






HIFI Spectroscopy of H₂O Submillimeter Lines in Nuclei of Actively Star-forming Galaxies

L. Liu^{1,2,3}, A. Weiß², J. P. Perez-Beaupuits^{2,4}, R. Güsten², D. Liu^{1,3}, Y. Gao¹, K. M. Menten² , P. van der Werf⁵ , F. P. Israel⁵ ,
A. Harris⁶, J. Martin-Pintado⁷, M. A. Requena-Torres^{2,6}, and J. Stutzki⁸

¹ Purple Mountain Observatory, Key Lab of Radio Astronomy, 2 West Beijing Road, 210008 Nanjing, PR China; ljliu@pmo.ac.cn

² Max-Planck-Institut für Radioastronomie, Auf dem Hügel 69, D-53121 Bonn, Germany; aweiss@mpifr-bonn.mpg.de

³ University of Chinese Academy of Sciences, 19A Yuquan Road, PO Box 3908, 100039 Beijing, PR China

⁴ European Southern Observatory, Santiago, Chile

⁵ Sterrewacht Leiden, Leiden University, PO Box 9513, 2300 RA, Leiden, The Netherlands

⁶ Department of Astronomy, University of Maryland, College Park, MD 20742, USA

⁷ Consejo Superior de Investigaciones Científicas, Spain

⁸ Physikalisches Institut der Universität zu Köln, Zùlpicher Straße 77, D-50937 Köln, Germany

Received 2017 January 20; revised 2017 June 11; accepted 2017 July 2; published 2017 August 24

Abstract

We present a systematic survey of multiple velocity-resolved H₂O spectra using *Herschel*/Heterodyne Instrument for the Far Infrared (HIFI) toward nine nearby actively star-forming galaxies. The ground-state and low-excitation lines ($E_{\text{up}} \leq 130$ K) show profiles with emission and absorption blended together, while absorption-free medium-excitation lines ($130 \text{ K} \leq E_{\text{up}} \leq 350$ K) typically display line shapes similar to CO. We analyze the HIFI observation together with archival SPIRE/PACS H₂O data using a state-of-the-art 3D radiative transfer code that includes the interaction between continuum and line emission. The water excitation models are combined with information on the dust and CO spectral line energy distribution to determine the physical structure of the interstellar medium (ISM). We identify two ISM components that are common to all galaxies: a warm ($T_{\text{dust}} \sim 40\text{--}70$ K), dense ($n(\text{H}) \sim 10^5\text{--}10^6 \text{ cm}^{-3}$) phase that dominates the emission of medium-excitation H₂O lines. This gas phase also dominates the far-IR emission and the CO intensities for $J_{\text{up}} > 8$. In addition, a cold ($T_{\text{dust}} \sim 20\text{--}30$ K), dense ($n(\text{H}) \sim 10^4\text{--}10^5 \text{ cm}^{-3}$), more extended phase is present. It outputs the emission in the low-excitation H₂O lines and typically also produces the prominent line absorption features. For the two ULIRGs in our sample (Arp 220 and Mrk 231) an even hotter and more compact ($R_s \leq 100$ pc) region is present, which is possibly linked to AGN activity. We find that collisions dominate the water excitation in the cold gas and for lines with $E_{\text{up}} \leq 300$ K and $E_{\text{up}} \leq 800$ K in the warm and hot component, respectively. Higher-energy levels are mainly excited by IR pumping.

Key words: galaxies: ISM – infrared: galaxies – ISM: molecules – line: formation – submillimeter: galaxies

1. Introduction

Galactic nuclei play a key role in our understanding of galactic evolution. An important method to determine their physical and chemical conditions is the analysis of molecular emission lines from the interstellar medium (ISM). Of particular interest is the water molecule, which has been demonstrated to have the uniquely powerful potential of deriving information on the ISM of external galaxies (e.g., González-Alfonso et al. 2010). The abundance of water in the gas phase ($[\text{H}_2\text{O}]/[\text{H}_2]$, $X(\text{H}_2\text{O})$) in quiescent molecular clouds is quite low, as suggested by studies in the Milky Way (e.g., $X(\text{H}_2\text{O}) < 1 \times 10^{-9}$; Caselli et al. 2010). But water becomes one of the most (third) abundant species in the shock-heated regions (e.g., Bergin et al. 2003; González-Alfonso et al. 2013) and in the dense warm regions in which radiation from newly formed stars raises the dust temperature above the ice evaporation temperature (e.g., Cernicharo et al. 2006a). Therefore, unlike other molecular gas tracers traditionally used to study the dense, star-forming (SF) ISM in extragalactic systems (such as CO and HCN), water probes the gas exclusively associated with SF regions or heated in the extreme environment of active galactic nuclei (AGNs). Because of its complex energy level structure and large level spacing, H₂O possesses a large number of rotation lines that lie mostly in the submillimeter and far-infrared (FIR) wavelength regime. These

lines can be very prominent in actively SF galaxies with intensities comparable to those of CO lines—much more prominent than other dense gas tracers such as HCN (e.g., van der Werf et al. 2011). The water lines not only probe the physical conditions of the gas-phase ISM (such as gas density and kinetic temperature) but also provide important clues on the dust IR radiation density as both collision with hydrogen molecules and IR pumping are important for their excitation (e.g., Weiß et al. 2010; González-Alfonso et al. 2012, 2014). The high-excitation water lines can even be used to reveal the presence of extended infrared-opaque regions in galactic nuclei and probe their physical conditions (van der Werf et al. 2011). This offers a potential diagnostic to distinguish AGN from starburst activity. Observations of water also shed light on the dominant chemistry in nuclear regions (e.g., Bergin et al. 1998, 2000; Melnick et al. 2000) as water could be a major reservoir of gas-phase interstellar oxygen (e.g., Cernicharo et al. 2006b). Overall, water provides a unique tool to probe the physical and chemical processes occurring in the galaxy nuclei and their surroundings (e.g., van der Werf et al. 2011; González-Alfonso et al. 2014).

However, previous observations of water in nearby extragalactic systems suffered great limitations. Ground-based observations of water in nearby galaxies have been limited to radio maser transitions (such as the famous 22 GHz water line)

or to a few systems with significant redshift (e.g., Combes & Wiklind 1997; Cernicharo et al. 2006a; Menten et al. 2008), due to the absorption by terrestrial atmospheric water vapor. Earlier satellite missions, such as *ODIN* and *SWAS*, did not have enough collecting area to detect the relatively faint ground transitions of water in external galaxies. *ISO* and, more recently, *Spitzer* have provided the first systematic studies of water in the FIR regime (e.g., Fischer et al. 1999; González-Alfonso et al. 2004). These missions, however, did not cover the frequencies of the molecule’s ground-state transitions and other low-excitation⁹ lines. These low-excitation water transitions provide crucial information on the widespread diffuse medium in galaxies (Weiß et al. 2010; van der Tak et al. 2016). Only with the launch of *Herschel*,¹⁰ with its large collecting area, have these transitions become accessible in the nearby universe (e.g., González-Alfonso et al. 2010; Weiß et al. 2010). Yet, SPIRE (and also PACS) on board *Herschel* does not provide the spectral resolution to obtain velocity-resolved spectra, and only the integrated line intensities (or barely resolved spectra) can be obtained from these observations.

High velocity resolution spectroscopy with *Herschel*’s Heterodyne Instrument for the Far Infrared (HIFI), however, allows us to derive detailed information on the shapes of H₂O lines, which is critical because emission and absorption are often mixed in water line profiles (Weiß et al. 2010). This implies that the modest spectral resolution of the *Herschel*/SPIRE spectroscopy results in severe limitations for the detections of low-excitation lines and limits the construction of excitation models, since emission and absorption from different ISM components along the line of sight are averaged. Recently, water has been detected in high-*z* sources with both high spectral and spatial resolution afforded by ALMA and NOEMA (e.g., Omont et al. 2011, 2013; Combes et al. 2012; Yang et al. 2016). The results confirm that H₂O lines are among the strongest molecular lines in high-*z* ultraluminous starburst galaxies, with intensities almost comparable to those of the high-*J* CO lines (e.g., Omont et al. 2013; Yang et al. 2016). In order to obtain a better understanding of observed water spectra in the early universe, a comprehensive analysis of water line shapes in the local universe is required. Only with HIFI are we able to investigate multiple water transitions resulting from levels with a wide range of energies in nearby galaxies in more detail than ever before.

The observed water line profiles provide crucial information on the geometry, dynamics, and physical structure of the ISM. However, retrieving this information is not straightforward, because most water lines have high optical depth (e.g., Poelman & van der Tak 2007; Poelman et al. 2007; Emprechtinger et al. 2012), so that column densities cannot be accurately derived from the observed line intensities alone. The excitation of water is also more complicated than other traditional gas tracers (e.g., CO, CS), as IR pumping has to be taken into account. The gas-phase H₂O could be a major coolant of the dense, SF ISM in case it is mainly collisionally excited. Yet, the relative importance of collision and IR pumping on the excitation of water in extragalactic sources has

not achieved a full understanding. Interstellar chemistry will benefit from an accurate knowledge of water abundances, the derivation of which requires detailed modeling of H₂O’s excitation of the rotational levels. Hence, to extract the underlying physical properties of the ISM (both gas and dust) and to investigate the relative contribution of the two excitation channels and derive chemical abundances, a detailed modeling of the water excitation is required.

In this paper we present velocity-resolved HIFI spectroscopy of multiple FIR H₂O lines (with upper energy $E_{\text{up}} \sim 50\text{--}450$ K) in a sample of nine local galaxies with different nuclear environments. We analyze the data using a 3D, non-LTE radiative transfer code. Our main goal is to deepen our understanding of the water excitation and to explore H₂O as a diagnostic tool to probe the physical and chemical conditions in the nuclei of active SF galaxies. We present our sample, observations, and data reduction in Section 2. A discussion of the line shapes is presented in Section 3. A description of our modeling method and a summary of our general model results are given in Section 4. In Section 5 we discuss the contributions from collisions and IR pumping on the excitation of water, as well as the resulting shape of the H₂O spectral line energy distributions (SLEDs), and establish an $L_{\text{H}_2\text{O}}\text{--}L_{\text{FIR}}$ luminosity relation. Our conclusions are summarized in Section 6.

2. Observation

Our sample is selected from the HEXGAL (*Herschel* ExtraGALactic) key project (PI: Güsten). HEXGAL is a project that aims to study the physical and chemical composition of the ISM in galactic nuclei, utilizing the very high spectral resolution of the HIFI instrument. Our sample consists of a total of nine galaxies and has been selected to cover a diversity of nuclear environments ranging from pure nuclear starburst galaxies (such as M82, NGC 253) to starburst nuclei that also host an AGN (such as NGC 4945) to AGN-dominated environments (such as Mrk 231) and to major mergers with even higher IR luminosity (such as Arp 220). The source names, systemic velocities, distances, FIR (40–120 μm ; Helou et al. 1985) luminosities, and galaxy types are given in Table 1. The FIR luminosities are computed by integrating our fitted SEDs over the wavelength range 40–120 μm (see Section 4.1.2 for more details on the dust SED fitting).

We have utilized HIFI to observe 5–10 carefully selected (both ortho- and para-) water transitions. Figure 1 shows the water energy diagram. Transitions observed with HIFI are indicated by blue arrows, whereas black arrows denote additional H₂O lines covered by *Herschel* SPIRE and PACS that are also included in our modeling (more details in Section 4.1.1). Our observed lines cover a wide energy range, from low-excitation transitions (with $E_{\text{up}} \leq 130$ K) to medium-excitation transitions (with $130 < E_{\text{up}} \leq 350$ K) to high-excitation transitions ($E_{\text{up}} \sim 350\text{--}450$ K). Table 2 reports our selected water transitions, the line frequencies, the energies of upper levels, the corresponding HIFI beam sizes, the galaxies toward which each line has been observed, whether emission or absorption is found, and the detection rate. The frequencies of our selected lines almost span the full HIFI frequency coverage of Bands 1–5 (480–1250 GHz) and Band 6 (1410–1910 GHz). The angular resolution changes from $\sim 40''$ for the o-H₂O 557 GHz line to $\sim 13''$ for the o-H₂O 1717 GHz line. We observed each galaxy toward a single position given in Table 1.

⁹ Throughout this paper, we use the term “low excitation” for H₂O lines with upper level energies $E_{\text{up}} \leq 130$ K, “medium excitation” for lines with $130 < E_{\text{up}} \leq 350$ K, and “high excitation” for lines with $E_{\text{up}} > 350$ K.

¹⁰ *Herschel* is an ESA space observatory with science instruments provided by European-led Principal Investigator consortia and with important participation from NASA.

Table 1
Sample Galaxies

Galaxy	v_{LSR} (km s^{-1})	Distance (Mpc)	L_{FIR} (FWHM = $40''$) ($\text{Log } L_{\odot}$)	R.A. h m s.s	Decl. deg' "	Type
M82	203	3.9	9.74	09 55 52.2	+69 40 46	SB
NGC 253	243	3.2	9.47	00 47 33.1	-25 17 17	SB
NGC 4945	563	3.9	10.70	13 05 27.4	-49 28 05	SB/AGN
NGC 1068	1137	12.6	10.32	02 42 40.7	-00 00 47	AGN/SB
Cen A	547	3.7	9.23	13 25 27.6	-43 01 08	AGN/SB
Mrk 231	12642	186	12.19	12 56 14.2	+56 52 25	AGN/SB
Antennae	1705	21.3	9.69	12 01 54.8	-18 52 55	SB, Major Merger
NGC 6240	7339	106	11.81	16 52 58.8	+02 24 03	AGN/SB, Major Merger
Arp 220	5434	78.7	11.98	15 34 57.2	+23 30 11	SB/AGN, Major Merger

Note. The FIR luminosities are computed by integrating our fitted SEDs over the wavelength range 40–120 μm . The last column indicates whether the IR luminosity of a galaxy is dominated by starbursts (SB), AGNs, or both, and whether the galaxy is a major merger.

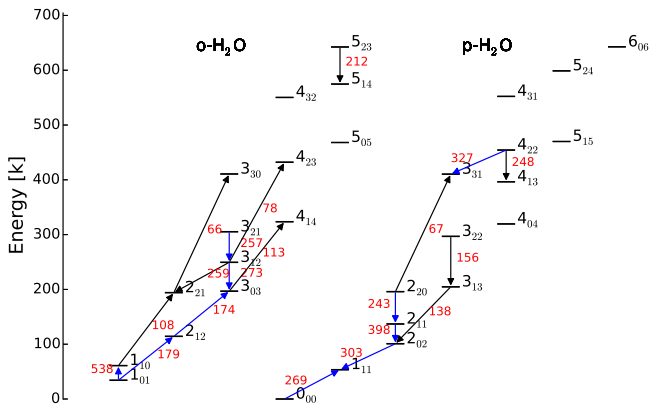


Figure 1. Energy level diagrams of H_2O (ortho and para). Blue arrows indicate lines observed with HIFI, and black arrows denote lines observed with SPIRE/PACS (data taken from literature). The downward-pointing arrows indicate the lines that are always detected in emission, while the upward-pointing arrows indicate the lines that are often observed in absorption. The red number denotes the wavelength (in μm) of each transition.

Thus, except for the most distant sources (Arp 220, Mrk 231, and NGC 6240), only the nuclear region is covered by our pointed observations.

The data were obtained between 2010 March and 2012 September, in a total of 124 hr of integration time. The dual beamswitch mode was used with a wobbler throw of $3'$ for all observations. The data were recorded using the wide-band acousto-optic spectrometer, consisting of four units with a bandwidth of 1 GHz each, covering the 4 GHz intermediate frequency band (IF) for each polarization with a spectral resolution of 1 MHz. Our spectra were calibrated using HIPE¹¹ and then exported to CLASS¹² format with the shortest possible pre-integration. For each scan we computed the underlying continuum using the line-free channels of a combined 4 GHz spectrum from the four sub-bands. Then, a first-order baselines was subtracted from each individual sub-band (in the cases where the signal spans over more than one sub-band, the nearby sub-bands were merged before subtracting the baselines). Next, the baseline-subtracted sub-bands in each scan were combined and the continuum level was added again. The noise-weighted spectra from two polarizations (H

and V) were thereafter averaged. Note that the continuum radiation enters the receiver through both sidebands while the line is only in one sideband. Therefore, the continuum used in our analysis (and for our figures) represents half of the value actually measured by HIFI. The o- H_2O ($3_{21} - 3_{12}$) 1163 GHz ($J = 10 - 9$) line; we therefore have estimated the CO ($J = 10 - 9$) line profile from the APEX CO ($J = 3 - 2$) line and subtracted it from the spectra.

3. Spectral Results and Analysis

We detected strong water emission and absorption in all galaxies except for the Antennae, which has no detection in any H_2O line. Our HIFI H_2O spectra are presented in Figures 11–18. The velocity scale on each panel is relative to the systemic velocity listed in Table 1. Except for a few sources (Mrk 231, NGC 1068, and NGC 6240), a wide variety of line shapes are observed for most galaxies in our sample (e.g., NGC 4945, NGC 253, M82). In the latter cases emission and absorption features are often blended. Unlike line profiles from multiple transitions of other molecules (such as CO), the line profiles of water cannot be assumed to be similar.

3.1. Line Shapes

3.1.1. Emission Lines

A few of the lines (indicated by blue downward-pointing solid arrows in Figure 1) are always detected in emission. They include a low-excitation line (p- H_2O ($2_{02} - 1_{11}$)), four medium-excitation lines (o- H_2O ($3_{12} - 3_{03}$), o- H_2O ($3_{21} - 3_{12}$), p- H_2O ($2_{11} - 2_{02}$), and p- H_2O ($2_{20} - 2_{11}$)), and a high-excitation line (p- H_2O ($4_{22} - 3_{31}$)). These emission lines display similar line shapes among each other and also show a good correspondence to the line profile of CO. Figure 2 presents the CO ($J = 3 - 2$) line obtained by APEX¹³ (FWHM $\sim 20''$) or JCMT (FWHM $\sim 14''$) overlaid on the HIFI-detected H_2O emission lines. All line profiles in Figure 2 have been scaled to the peak of the CO line for better visualization of the line shapes. One can see that, except for NGC 253, whose water line profile is slightly narrower than the

¹¹ Version 10.0.0. HIPE is a joint development by the *Herschel* Science Ground Segment Consortium, consisting of ESA and the NASA *Herschel*.

¹² <http://www.iram.fr/IRAMFR/GILDAS>

¹³ This publication is based in part on data acquired with the Atacama Pathfinder Experiment (APEX). APEX is a collaboration between the Max-Planck-Institut für Radioastronomie, the European Southern Observatory, and the Onsala Space Observatory.

Table 2
Selected Water Transitions

Line	Freq. (GHz)	E_{up} (K)	FWHM (arcsec)	Observed Galaxies	Emission or Absorption ^a	Detection Rate ^b
p-H ₂ O (1 ₁₁ –0 ₀₀)	1113	53.4	19	All	Absorption, emission	7/9
o-H ₂ O (1 ₁₀ –1 ₀₁)	557	61.0	40	All	Absorption, emission	8/9
p-H ₂ O (2 ₀₂ –1 ₁₁)	988	100.8	22	All	Emission	8/9
o-H ₂ O (2 ₁₂ –1 ₀₁)	1670	114.4	13	NGC 253, NGC 4945	Absorption	2/2
p-H ₂ O (2 ₁₁ –2 ₀₂)	752	136.9	28	All	Emission	6/9
p-H ₂ O (2 ₂₀ –2 ₁₁)	1229	195.9	17	NGC 253, Cen A	Emission	1/2
o-H ₂ O (3 ₀₃ –2 ₁₂)	1717	196.8	12	NGC 253, NGC 4945	Absorption, emission	2/2
o-H ₂ O (3 ₁₂ –3 ₀₃)	1097	249.4	19	All but NGC 1068	Emission	6/8
o-H ₂ O (3 ₂₁ –3 ₁₂)	1163	305.3	18	NGC 4945/253/6240, Cen A	Emission	2/4
p-H ₂ O (4 ₂₂ –3 ₃₁)	916	454.3	23	All	Emission	1/9

Notes.

^a Whether a line has been detected in emission, absorption, or both in our sample galaxies.

^b The number of detected galaxies divided by the number of observed galaxies.

CO (3–2) profile (see Appendix B for more discussions on this), water is often detected over the full velocity range of CO. This suggests that water is as widespread as CO and likely traces the bulk of the molecular gas in the central region of galaxies.

The closest resemblance is found between the CO and four medium-excitation H₂O lines that have $E_{\text{up}} \simeq 130$ –305 K above the ground state. The high-excitation emission line—p-H₂O (4₂₂ – 3₃₁) (with $E_{\text{up}} \simeq 450$ K)—which has been detected only in Arp 220, displays a narrower velocity dispersion (235 ± 18 km s^{–1}) compared with that of the CO and medium-excitation H₂O lines (412 ± 32 km s^{–1}; see Figure 2). The low-excitation emission line p-H₂O (2₀₂ – 1₁₁) (with $E_{\text{up}} \simeq 100$ K) often exhibits diminished emission compared to CO at the velocities where ground-state absorptions are detected, implying that the line is partly absorbed at the same velocities.

3.1.2. Absorption Lines

We have found four lines with absorption features in at least one galaxy of our sample. These are the p-H₂O ground-state (1₁₁ – 0₀₀) line, the o-H₂O ground-state (1₁₀ – 1₀₁) line, the o-H₂O (2₁₂ – 1₀₁) line, and the o-H₂O (3₀₃ – 2₁₂) line (see blue upward-pointing arrows in Figure 1). Except for the o-H₂O (3₀₃ – 2₁₂) line, which has $E_{\text{up}} \simeq 195$ K, all other absorption lines occur in low energy levels (50 K \leq $E_{\text{up}} \leq 115$ K). The two ground-state H₂O lines show absorptions toward all galaxies except for Mrk 231, NGC 1068, and NGC 6240. We further find that the absorption depth of the o-H₂O ground-state line is usually much weaker (10%–25%) than that of the p-H₂O ground-state line. The other two absorption lines (o-H₂O (2₁₂ – 1₀₁) and o-H₂O (3₀₃ – 2₁₂)) have only been observed toward NGC 253 and NGC 4945. Their line shapes are similar to the absorption feature of the p-H₂O ground-state line.

The observed absorption features can appear to be either broad and deep (e.g., Arp 220 and NGC 4945) or narrow and shallow (e.g., Cen A). In some galaxies (e.g., NGC 253 and NGC 4945), the low-excitation absorption feature covers a velocity range matching that of medium-excitation H₂O emission lines, while in some other galaxies (e.g., M82) the absorption feature occurs at a velocity that does not show emission in other lines.

Absorption and emission features are often found to be blended. Especially for the o-H₂O ground-state line, strong emission is detected in all of our sample galaxies, in particular toward the high- and low-velocity wings of the line profile. Conspicuous emission features also show up in the p-H₂O ground-state line in a few galaxies (e.g., NGC 253 and NGC 1068), although they appear to be much weaker. Finally, we find that the observed global line profiles with absorption and emission blended together are best explained by an emission profile similar to the medium-excitation H₂O lines modified by absorption components from foreground gas. It is therefore tempting to speculate that the lack of absorption at certain velocities has a geometrical origin, i.e., gas at these velocities is located outside of the sightline of the continuum (Weiß et al. 2010).

3.2. Gaussian Decomposition of Line Profiles

The complex water line shapes found in our sample galaxies suggest an ISM structure with several different physical components. In order to separate the individual contributions of multiple physical regions and to disentangle absorption from emission, we have performed a Gaussian decomposition of the observed H₂O line profiles. We first decompose the absorption-free medium-excitation H₂O emission lines and the CO($J = 3 - 2$) line, which typically requires two or three Gaussian components.

We next fit the remaining H₂O lines but constrain their line centroids and widths to narrow ranges centered on the thus-derived Gaussian fit parameters. The intensity of each component is then free to vary (from negative to positive). This procedure works well for the galaxies that show only emissions (Mrk 231, NGC 1068, and NGC 6240) and NGC 4945, where the width and velocity centroid of the absorption feature match one of the medium-excitation emission components.

For the remaining galaxies, however, one or two additional Gaussian components are required to fit the profile of the low-excitation and/or high-excitation lines. Specifically, we added a component for M82 and Cen A to match the narrow absorption feature seen at the galaxy systemic velocity and a component for NGC 253 to fit the redshifted broader emission seen only in the two ground-state lines. We added two additional components for Arp 220 to match the absorption

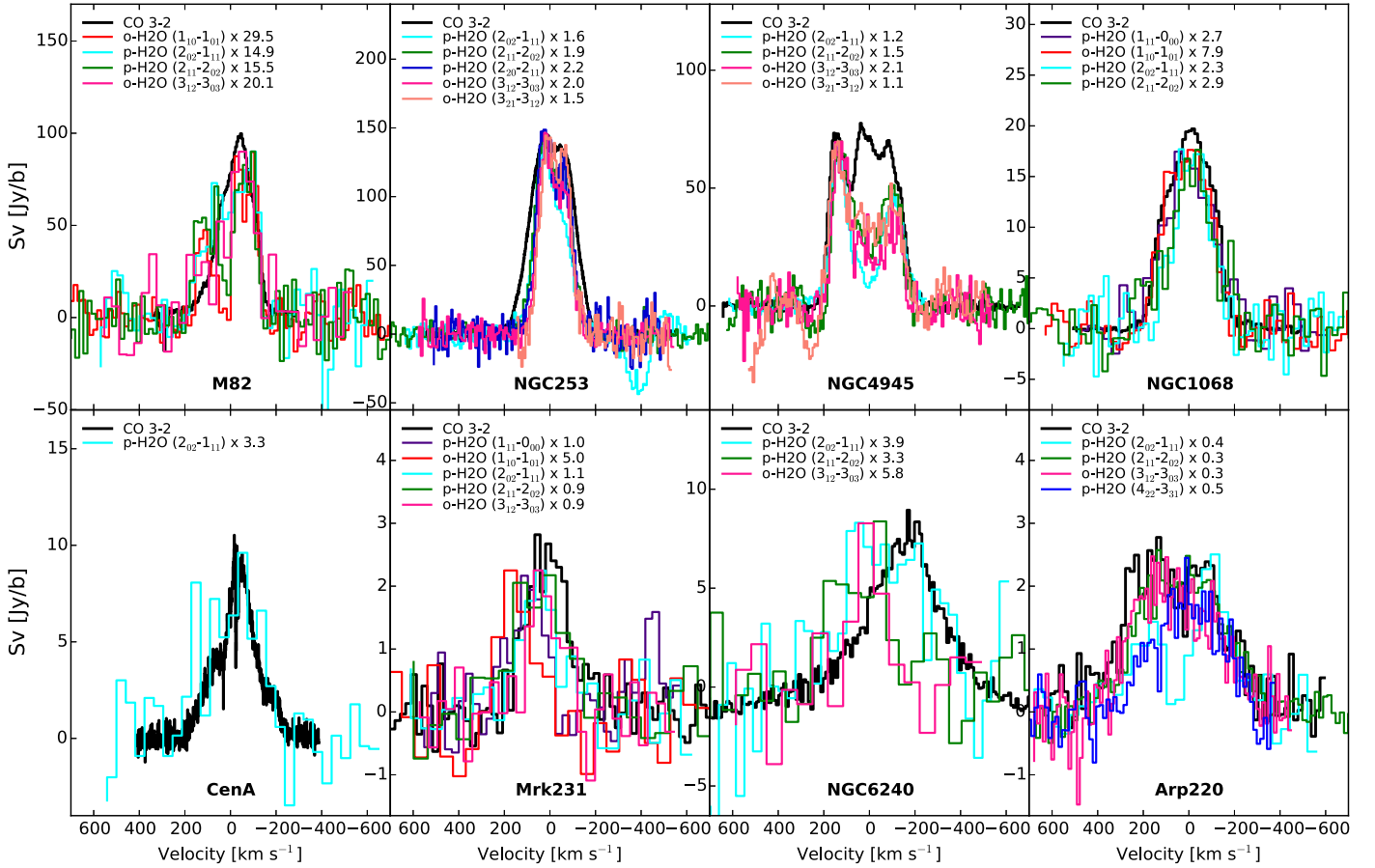


Figure 2. Water emission-line profiles are superposed on the CO($J=3-2$) line. The velocity scale is relative to the systemic velocity of each galaxy. The water line profiles are scaled to provide closest matches to the peak value of the CO profile.

feature in the low-excitation lines and the narrower emission feature evident in the higher-excitation p-H₂O ($4_{22} - 3_{31}$) line, respectively.

The IDL package MPFIT (Markwardt 2009) was used in the fitting analysis. In most cases, we allow the position of each Gaussian component to change by $\pm 2-3 \text{ km s}^{-1}$ and the line width by $\pm 5\%$. The line centroids and widths of Arp 220 are allowed to change by $\pm 5 \text{ km s}^{-1}$ and $\pm 8\%$, respectively. The resulting parameters from Gaussian decomposition are given in Table 3.

4. Line Modeling

4.1. Additional Observation Data

In order to better constrain the physical parameters of our model and also to check the reliability of our final model results, we have gathered IR and (sub)millimeter wavelength spectroscopy and continuum data from the literature. These supplementary data include SPIRE/PACS H₂O data, IR and (sub)millimeter wavelength continuum data ($\nu \sim 1 \times 10^2-10^5 \text{ GHz}$), and ground-based and SPIRE/HIFI CO $1 \leq J_{\text{up}} \leq 13$ fluxes. The dust continuum data are required to constrain the intrinsic IR radiation field and its effect on water excitation. The inclusion of the CO data allows us to investigate to which level the gas traced by water emission is related to the shape of CO SLEDs. For extended sources, all data have been scaled to a uniform beam size of $40''$ by applying the correction factors derived from IR images (see Section 4.1.2 for more details on the IR images).

4.1.1. SPIRE/PACS H₂O Data

In addition to our HIFI H₂O data, published H₂O data observed by *Herschel*/SPIRE and PACS from literature have also been incorporated into our line modeling, with the aim of studying the overall water excitation across a large number of energy levels. SPIRE combines a three-color photometer and a low- to medium-resolution Fourier Transform Spectrometer (FTS), with continuous spectral coverage from 190 to 670 μm ($\nu \approx 450-1550 \text{ GHz}$) and a spectral resolving power of ≈ 1400 . SPIRE H₂O data were used for transitions that were not observed/detected by HIFI. PACS detects H₂O lines with frequencies higher than those covered by SPIRE and HIFI ($\nu \sim 1500-5000 \text{ GHz}$), most of which have high excitation ($E_{\text{up}} \sim 300-650 \text{ K}$).

H₂O transitions, for which we only have SPIRE and PACS data, are labeled by black arrows in Figure 1. Again, downward-pointing arrows indicate emission lines, and upward-pointing arrows indicate the transitions that are often detected in absorption (some of them appear in emission occasionally). From Figure 1, we can see that the high-excitation lines with frequencies close to the peak of the dust continuum SED in SF/starburst galaxies ($\lambda \sim 60-150 \mu\text{m}$ or $\nu \sim 2000-4500 \text{ GHz}$) usually appear in absorption, while the lower-frequency ($\lambda \geq 150 \mu\text{m}$ or $\nu \leq 2000 \text{ GHz}$) high-excitation lines are often detected in emission. Note that for the SPIRE and PACS H₂O data, only integrated intensities are available. When information on their line shape is required, we use our HIFI H₂O line profiles as a proxy.

Table 3
Line Parameters Derived from Gaussian Decomposition

Source	Line	δv (km s ⁻¹)	FWHM (km s ⁻¹)	I (Jy beam ⁻¹ km s ⁻¹)	I_ν Cont. (Jy beam ⁻¹)
M82	o-H ₂ O (1 ₁₀ -1 ₀₁)	86 ± 2	122 ± 6	320 ± 0	13.6 ± 3.4 (538 μm)
		-73 ± 2	103 ± 5	333 ± 25	
		26 ± 2	65 ± 1	-137 ± 21	
	p-H ₂ O (1 ₁₁ -0 ₀₀)	86 ± 2	122 ± 6	≤153	85.0 ± 13.6 (269 μm)
		-73 ± 2	103 ± 5	≤140	
		26 ± 2	65 ± 1	-869 ± 34	
	p-H ₂ O (2 ₀₂ -1 ₁₁)	86 ± 2	122 ± 6	518 ± 76	59.7 ± 27.9 (303 μm)
		-73 ± 2	103 ± 5	701 ± 70	
		26 ± 2	65 ± 1	≤139	
	p-H ₂ O (2 ₁₁ -2 ₀₂)	86 ± 2	122 ± 6	458 ± 54	33.2 ± 5.0 (398 μm)
		-73 ± 2	103 ± 5	584 ± 41	
		26 ± 2	65 ± 1	≤83	
o-H ₂ O (3 ₁₂ -3 ₀₃)	86 ± 2	122 ± 6	209 ± 69	85.3 ± 9.6 (273 μm)	
	-73 ± 2	103 ± 5	545 ± 63		
	26 ± 2	65 ± 1	≤102		
p-H ₂ O (4 ₂₂ -3 ₃₁)	≤231	53.0 ± 8.5 (327 μm)	
NGC 253	o-H ₂ O (1 ₁₀ -1 ₀₁)	23 ± 3	91 ± 11	639 ± 92	19.7 ± 4.1 (538 μm)
		-60 ± 3	96 ± 11	-106 ± 40	
		80 ± 3	94 ± 9	1316 ± 75	
	p-H ₂ O (1 ₁₁ -0 ₀₀)	23 ± 3	91 ± 11	-2024 ± 234	181.5 ± 34.9 (269 μm)
		-60 ± 3	96 ± 11	-8548 ± 160	
		80 ± 3	94 ± 9	3629 ± 245	
	o-H ₂ O (2 ₁₂ -1 ₀₁)	23 ± 3	91 ± 11	-4179 ± 170	308.7 ± 70.8 (179 μm)
		-60 ± 3	96 ± 11	-18579 ± 214	
		80 ± 3	94 ± 9	≤905	
	p-H ₂ O (2 ₀₂ -1 ₁₁)	23 ± 3	91 ± 11	8001 ± 454	114.5 ± 26.4 (303 μm)
		-60 ± 3	96 ± 11	4640 ± 460	
		80 ± 3	94 ± 9	≤300	
	p-H ₂ O (2 ₁₁ -2 ₀₂)	23 ± 3	91 ± 11	6524 ± 155	55.0 ± 14.0 (398 μm)
		-60 ± 3	96 ± 11	5927 ± 161	
		80 ± 3	94 ± 9	≤268	
	p-H ₂ O (2 ₂₀ -2 ₁₁)	23 ± 3	91 ± 11	5496 ± 181	224.4 ± 30.3 (243 μm)
		-60 ± 3	96 ± 11	4997 ± 250	
		80 ± 3	94 ± 9	≤372	
	o-H ₂ O(3 ₀₃ -2 ₁₂)	23 ± 3	91 ± 11	4171 ± 215	378.6 ± 237.7 (174 μm)
		-60 ± 3	96 ± 11	≤990	
		80 ± 3	94 ± 9	≤944	
	o-H ₂ O (3 ₁₂ -3 ₀₃)	23 ± 3	91 ± 11	5450 ± 123	178.4 ± 36.5 (273 μm)
		-60 ± 3	96 ± 11	4692 ± 151	
		80 ± 3	94 ± 9	≤302	
o-H ₂ O (3 ₂₁ -3 ₁₂)	23 ± 3	91 ± 11	6316 ± 382	201.3 ± 32.0 (257 μm)	
	-60 ± 3	96 ± 11	8092 ± 404		
	80 ± 3	94 ± 9	≤592		
p-H ₂ O (4 ₂₂ -3 ₃₁)	≤1143	98.0 ± 24.3 (327 μm)	
NGC 4945	o-H ₂ O (1 ₁₀ -1 ₀₁)	-112 ± 3	98 ± 7	1122 ± 38	30.1 ± 5.1 (538 μm)
		48 ± 3	136 ± 10	-2348 ± 66	
		141 ± 3	63 ± 5	769 ± 46	
	p-H ₂ O (1 ₁₁ -0 ₀₀)	-112 ± 3	98 ± 7	≤295	237.4 ± 36.6 (269 μm)
		48 ± 3	136 ± 10	-25771 ± 286	
		141 ± 3	63 ± 5	1579 ± 138	
	o-H ₂ O (2 ₁₂ -1 ₀₁)	-112 ± 3	98 ± 7	≤909	458.7 ± 69.4 (179 μm)
		48 ± 3	136 ± 10	-68706 ± 291	
		141 ± 3	63 ± 5	≤729	
	p-H ₂ O (2 ₀₂ -1 ₁₁)	-112 ± 3	98 ± 7	4301 ± 87	173.9 ± 24.8 (303 μm)
		48 ± 3	136 ± 10	2032 ± 84	
		141 ± 3	63 ± 5	3890 ± 60	
	p-H ₂ O (2 ₁₁ -2 ₀₂)	-112 ± 3	98 ± 7	3430 ± 207	85.3 ± 15.4 (398 μm)
		48 ± 3	136 ± 10	3939 ± 336	
		141 ± 3	63 ± 5	2285 ± 198	
	o-H ₂ O (3 ₀₃ -2 ₁₂)	-112 ± 3	98 ± 7	≤891	475.5 ± 228.1 (174 μm)
		48 ± 3	136 ± 10	-12823 ± 231	
		141 ± 3	63 ± 5	≤714	

Table 3
(Continued)

Source	Line	δv (km s ⁻¹)	FWHM (km s ⁻¹)	I (Jy beam ⁻¹ km s ⁻¹)	I_ν Cont. (Jy beam ⁻¹)
	o-H ₂ O (3 ₁₂ -3 ₀₃)	-112 ± 3 48 ± 3	98 ± 7 136 ± 10	1548 ± 120 2362 ± 281	240.8 ± 39.2 (273 μm)
	o-H ₂ O (3 ₂₁ -3 ₁₂)	141 ± 3 -112 ± 3 48 ± 3 141 ± 3	63 ± 5 98 ± 7 136 ± 10 63 ± 5	1842 ± 169 4135 ± 304 5633 ± 342 3658 ± 255	277.9 ± 31.5 (257 μm)
	p-H ₂ O (4 ₂₂ -3 ₃₁)	≤593	146.1 ± 17.4 (327 μm)
NGC 1068	o-H ₂ O (1 ₁₀ -1 ₀₁)	-18 ± 2	211 ± 10	557 ± 18	4.3 ± 2.4 (538 μm)
	p-H ₂ O (1 ₁₁ -0 ₀₀)	-18 ± 2	211 ± 10	1552 ± 72	18.9 ± 10.9 (269 μm)
	p-H ₂ O (2 ₀₂ -1 ₁₁)	-18 ± 2	211 ± 10	1554 ± 94	17.1 ± 11.4 (303 μm)
	p-H ₂ O (2 ₁₁ -2 ₀₂)	-18 ± 2	211 ± 10	1264 ± 74	8.7 ± 3.4 (398 μm)
	p-H ₂ O (4 ₂₂ -3 ₃₁)	≤137	13.6 ± 6.0 (327 μm)
Cen A	o-H ₂ O (1 ₁₀ -1 ₀₁)	0 ± 2 16 ± 2	235 ± 11 70 ± 3	682 ± 58 -384 ± 32	10.1 ± 2.6 (538 μm)
	p-H ₂ O (1 ₁₁ -0 ₀₀)	0 ± 2 16 ± 2	235 ± 11 70 ± 3	384 ± 138 -358 ± 75	16.9 ± 7.0 (269 μm)
	p-H ₂ O (2 ₀₂ -1 ₁₁)	0 ± 2 16 ± 2	235 ± 11 70 ± 3	631 ± 65 ≤84	12.4 ± 8.3 (303 μm)
	p-H ₂ O (2 ₁₁ -2 ₀₂)	≤606	11.6 ± 5.8 (398 μm)
	p-H ₂ O (2 ₂₀ -2 ₁₁)	≤619	17.1 ± 11.4 (243 μm)
	o-H ₂ O (3 ₁₂ -3 ₀₃)	≤489	15.0 ± 6.6 (273 μm)
	o-H ₂ O (3 ₂₁ -3 ₁₂)	≤734	18.4 ± 12.2 (257 μm)
	p-H ₂ O (4 ₂₂ -3 ₃₁)	≤425	11.6 ± 7.7 (327 μm)
Mrk 231	o-H ₂ O (1 ₁₀ -1 ₀₁)	50 ± 2	211 ± 10	66 ± 77	0.4 ± 0.3 (538 μm)
	p-H ₂ O (1 ₁₁ -0 ₀₀)	50 ± 2	211 ± 10	362 ± 44	3.3 ± 2.2 (269 μm)
	p-H ₂ O (2 ₀₂ -1 ₁₁)	50 ± 2	211 ± 10	376 ± 54	2.6 ± 1.7 (303 μm)
	p-H ₂ O (2 ₁₁ -2 ₀₂)	50 ± 2	211 ± 10	588 ± 67	1.1 ± 0.7 (398 μm)
	o-H ₂ O (3 ₁₂ -3 ₀₃)	50 ± 2	211 ± 10	390 ± 63	3.5 ± 2.3 (273 μm)
	p-H ₂ O (4 ₂₂ -3 ₃₁)	≤191	2.1 ± 1.4 (327 μm)
Antennae	o-H ₂ O (1 ₁₀ -1 ₀₁)	≤68	0.90 ± 0.5 (538 μm)
	p-H ₂ O (1 ₁₁ -0 ₀₀)	≤126	4.65 ± 3.0 (269 μm)
	p-H ₂ O (2 ₀₂ -1 ₁₁)	≤233	1.96 ± 1.2 (303 μm)
	p-H ₂ O (2 ₁₁ -2 ₀₂)	≤125	1.71 ± 1.5 (398 μm)
	o-H ₂ O (3 ₁₂ -3 ₀₃)	≤171	3.00 ± 2.0 (273 μm)
	p-H ₂ O (4 ₂₂ -3 ₃₁)	≤148	2.25 ± 1.9 (327 μm)
NGC 6240	o-H ₂ O (1 ₁₀ -1 ₀₁)	-10 ± 2	282 ± 14	175 ± 33	0.5 ± 0.3 (538 μm)
	p-H ₂ O (1 ₁₁ -0 ₀₀)	≤334	4.5 ± 3.0 (269 μm)
	p-H ₂ O (2 ₀₂ -1 ₁₁)	-10 ± 2	282 ± 14	660 ± 116	4.6 ± 3.0 (303 μm)
	p-H ₂ O (2 ₁₁ -2 ₀₂)	-10 ± 2	282 ± 14	592 ± 81	1.3 ± 0.9 (398 μm)
	o-H ₂ O (3 ₁₂ -3 ₀₃)	-10 ± 2	282 ± 14	253 ± 53	3.1 ± 2.1 (273 μm)
	o-H ₂ O (3 ₂₁ -3 ₁₂)	≤546	4.8 ± 3.2 (257 μm)
	p-H ₂ O (4 ₂₂ -3 ₃₁)	≤375	2.3 ± 1.6 (327 μm)
Arp 220	o-H ₂ O (1 ₁₀ -1 ₀₁)	52 ± 5 20 ± 5 35 ± 5	412 ± 32 226 ± 18 235 ± 18	812 ± 133 -850 ± 98 ≤96	2.5 ± 1.6 (538 μm)
	p-H ₂ O (1 ₁₁ -0 ₀₀)	52 ± 5 20 ± 5 35 ± 5	412 ± 32 226 ± 18 235 ± 18	≤449 -3486 ± 141 ≤339	24.3 ± 14.3 (269 μm)
	p-H ₂ O (2 ₀₂ -1 ₁₁)	52 ± 5 20 ± 5 35 ± 5	412 ± 32 226 ± 18 235 ± 18	3162 ± 469 -1369 ± 477 ≤288	16.6 ± 11.1 (303 μm)
	p-H ₂ O (2 ₁₁ -2 ₀₂)	52 ± 5 20 ± 5 35 ± 5	412 ± 32 226 ± 18 235 ± 18	3481 ± 91 ≤132 ≤134	7.9 ± 4.2 (398 μm)
	o-H ₂ O (3 ₁₂ -3 ₀₃)	52 ± 5 20 ± 5 35 ± 5	412 ± 32 226 ± 18 235 ± 18	3021 ± 156 ≤232 ≤237	23.5 ± 11.3 (273 μm)
	p-H ₂ O (4 ₂₂ -3 ₃₁)	52 ± 5 20 ± 5	412 ± 32 226 ± 18	≤188 ≤139	13.3 ± 8.3 (327 μm)

Table 3
(Continued)

Source	Line	δv (km s ⁻¹)	FWHM (km s ⁻¹)	I (Jy beam ⁻¹ km s ⁻¹)	I_ν Cont. (Jy beam ⁻¹)
		35 ± 5	235 ± 18	811 ± 92	

Note. The errors of line center (δv) and line width (FWHM) are not the real fitted errors, but the ranges by which the parameters are allowed to vary. We allow the position of each Gaussian component to change by $\pm 2\text{--}3$ km s⁻¹ (± 5 km s⁻¹ in Arp 220) and the line width by $\sim \pm 5\%$ ($\sim \pm 8\%$ in Arp 220). The upper limits to water intensities in the Antennae are derived by adopting an FWHM = 200 km s⁻¹ from CO observation by Gao et al. (2001).

4.1.2. IR and Submillimeter Data

The submillimeter to IR imaging of our target galaxies is used in two ways. First, the observed distribution of the dust continuum has been used for our extended sources to compute aperture corrections to compensate for the different beam sizes of our HIFI observation, as well as for the other line data used in our analysis. To derive the aperture corrections, we have smoothed the highest spatial resolution map (typically PACS observations near the peak of the dust SED but in some cases also 350 μm maps from the Submillimetre Apex Bolometer Camera [SABOCA, FWHM = 7''.5]) to different spatial resolutions up to 40'', which corresponds to the largest HIFI beam size (in our data set, that of the H₂O ($1_{10}\text{--}1_{01}$) 557 GHz line). For each smoothed map we derive the aperture correction from the ratio of the peak flux relative to the flux at 40'' resolution, which allows us to scale all observations to a common aperture of 40''.

Second, the observed dust SEDs are used to constrain the dust continuum models for our target galaxies, which is a crucial ingredient for the modeling of water excitation. Apart from the IR fluxes measured by our HIFI observations at the H₂O line frequencies, we collect submillimeter to IR fluxes in the frequency range of $\sim 3 \times 10^2\text{--}10^5$ GHz ($\lambda \sim 3\text{--}1000$ μm) from the observations by *Spitzer*, *WISE*, *IRAS*, *Herschel* PACS/SPIRE, and *ISO*, as well as APEX 870 μm LABOCA and 350 μm SABOCA observations. The submillimeter data on the long-wavelength (Rayleigh–Jeans) tail enable us to better constrain the far-IR SED and the properties of cold dust in the galaxy (e.g., Weiß et al. 2008). The submillimeter and IR images are gathered for the extended sources.

We compute for each model the full dust SED and compared it to the observed dust flux densities (see Appendix A.1 for detailed description on our approach of dust SED modeling). Since we cannot be sure that all dust continuum emission is physically associated with water line emission, we consider a model more reliable if the predicted dust SED does not exceed the observed dust continuum intensities.

4.1.3. CO Data

In order to verify that our H₂O models are also consistent with other ISM tracers and to investigate to which level the H₂O-emitting volume contributes to the line intensity of other molecules, we also incorporate CO into our models. The CO molecule is a good tracer of overall gas content and excitation because it is mainly collisionally excited. In addition, it is the best-studied ISM tracer in extragalactic sources. The ground-state and low- J ($J_{\text{up}} \leq 3$) CO data have been collected from various sources in the literature (e.g., Papadopoulos et al. 2012; Greve et al. 2014, and references therein). The $J_{\text{up}} = 4\text{--}13$ CO line intensities (CO SLED) have been extracted from archival SPIRE/FTS observations (Panuzzo et al. 2010; van der Werf

et al. 2010; Rangwala et al. 2011; Spinoglio et al. 2012; Meijerink et al. 2013; Papadopoulos et al. 2014; Rosenberg et al. 2014). For some sources (e.g., M82, NGC 253, and Cen A) high- J ($J_{\text{up}} = 5$ to 13) CO lines observed with HIFI have also been collected (see, e.g., Loenen et al. 2010; Israel et al. 2014). The velocity-resolved HIFI CO observations allow us to model in detail the CO SLED for each Gaussian velocity component present in the HIFI H₂O profiles.

We have calculated the fluxes of CO transitions with $J_{\text{up}} = 1$ to 13 for each of our models and compared them to the observed values. As for the modeling of the dust continuum, we require that the model-predicted CO intensities from the H₂O-emitting volume shall not exceed the observed CO SLED.

4.2. Basic Model Description

4.2.1. The $\beta 3D$ Code

An updated version of the non-LTE 3D radiative transfer code “ $\beta 3D$ ” is used to calculate the excitation and radiative transfer of the molecular gas species (H₂O and CO in our work). $\beta 3D$ was first developed by Poelman & Spaans (2005, 2006). The main advantages of the code are its dimensionality and speed. It is not limited to spherical or axisymmetric problems but allows us to model arbitrary 3D structures where a unique gas and dust temperature, density, and abundance value can be attributed to every position (i.e., 3D grid cell). The code does not suffer from convergence problems at high optical depth, which reduces the computing time, as it adopts the escape probability method. The use of a multizone formalism, in contrast to a one-zone approach, allows us to calculate excitation gradients within opaque sources. We here use a modified version of $\beta 3D$, where the molecular and atomic line intensities and profiles are calculated within a line-tracing approach for an arbitrary viewing angle (Pérez-Beaupuits et al. 2011). Numerical results from $\beta 3D$ have extensively been tested against benchmark problems (see van Zadelhoff et al. 2002; van der Tak et al. 2005).

In the work presented here, we further extended the code by implementing the dust emission and absorption in the line radiative transfer by adopting the extended escape probability method developed by Takahashi et al. (1983). This allows us to take the interaction between dust and molecular gas into account. The dust grains are assumed to be mixed evenly with hydrogen gas (assuming a gas-to-dust mass ratio of 100:1), and the radiation field from the thermal dust emission is computed from each grid cell. More details on the extended escape probability method and our default parameter setting in $\beta 3D$ (e.g., dust grain property) are given in Appendix A.2. The resulting global line profile is computed using our newly developed ray-tracing approach, where the photons at various velocity channels are integrated through the dust and gas column along a line of sight within multiple ISM

components (for more details on our ray-tracing approach see Appendix A.3).

4.2.2. Applying β 3D to a Galaxy Using Multiple ISM Components

Modeling a galaxy as a whole still turns out to be impractical at present, because building up a galaxy with a detailed 3D geometry structure (e.g., arms, rings, disks) and kinematics (e.g., rotation, outflow, inflow) requires a huge cube, which will result in heavy memory usage and extremely slow computation speed. With the angular resolution of HIFI, our main goal is to investigate the observed different H₂O line shapes and the underlying properties of different physical regions, i.e., ISM components. Therefore, we model a galaxy by utilizing several different ISM components, assuming that each ISM component is an ensemble of molecular clumps with identical physical properties. The equilibrium temperature and level populations of the gas, however, are calculated within only a single clump based on our assumption that the excitation of the molecular gas at a given location should be connected mainly with gas and dust of the same clump and barely related to external clumps. This assumption is reasonable given that the contribution of an external clump to the local radiation intensity $\langle J_\nu \rangle$ at a test point depends on its spanned solid angle seen by the point (as suggested by Equations (5)–(7) in Appendix A.2), which is usually negligible considering the small volume filling factor of molecular clumps in galaxies. This assumption is similar to the approach in other radiative transfer calculations such as large velocity gradient (LVG) models, where the velocity gradient of a clump provides an intrinsic escape mechanism for photons by Doppler-shifting the frequencies out of the line. Thereby the radiative trapping is generally confined to the local region, i.e., the molecular clump (Takahashi et al. 1983).

A clump has been assumed to be a homogeneous, isothermal cube (grid size is $20 \times 20 \times 20$) whose main constituents are the hydrogen molecule gas (H₂), dust grains, and the molecular species of interest (H₂O and CO in our work). Hydrogen is assumed to be totally molecular in our model because the main part of the dissociating UV radiation is already absorbed in regions where H₂O is present (Poelman & Spaans 2005). The thermodynamic equilibrium statistical value of 3 is adopted to the water ortho-to-para ratio (OPR). In order to examine the water excitation under different physical conditions, we have generated a grid of clump models by varying five free parameters: hydrogen column density of clump $N_{\text{clump}}(\text{H})$, hydrogen density $n(\text{H})$, gas kinetic temperature T_K , dust temperature T_{dust} , and H₂O abundance $X(\text{H}_2\text{O})$. However, for simplicity, we fixed the CO abundance to the value of 1×10^{-4} , because it has been found to vary very little in different molecular clouds in nearby galaxies (e.g., Elmegreen et al. 1980; Tacconi & Young 1985; France et al. 2014; Bialy & Sternberg 2015). In fact, most of the CO lines are found to be optically thick in our sample galaxies, and thereby the modeled CO fluxes are not very sensitive to the adopted CO abundance.

With the level populations of H₂O and CO calculated for a clump, we next built an ISM component from an ensemble of clumps. The emergent line profile and dust continuum flux from an ISM component is calculated by our newly developed ray-tracing program (see Appendix A.3), which integrates both the line and dust continuum photons over all the overlapping clumps along a line of sight. This procedure is crucial, as the resulting global line profile is not just a simple superposition of

intrinsic line profiles of individual clumps, especially when the line is optically thick or dust continuum at line frequency becomes non-negligible. For example, the gas of foreground clumps will absorb the emission from clumps in the background, and thereby their contributions to the final line profile will significantly deviate from the sum of their intrinsic line profiles. The problem of a simple superposition of line profiles from overlapping clumps in an optically thick region has been pointed out by several authors (e.g., Downes et al. 1993; Aalto et al. 2015). As a result, the total column density of the ISM component has significant influence on not only integrated line intensity but also the line shape (including whether a modeled line appears in emission or absorption) and has therefore been introduced as the sixth free parameter ($N(\text{H})$). Since we do not want to involve the detailed galaxy dynamics in our model, a random normal distribution of velocities was attributed to the clumps of each ISM component as a statistical approximation. The velocity distributions follow the properties derived from our Gaussian decomposition of HIFI H₂O spectra (see Section 3.2).

We model each Gaussian-decomposed velocity component of H₂O spectra separately. However, even for a single velocity component, we fail to fit all observed H₂O line intensities by using only one ISM component. This implies that different H₂O lines (at a certain velocity) arise from different physical regions. Therefore, we model each velocity component of H₂O spectra with multiple ISM components (i.e., the combination of different clump properties). The final model of a galaxy is then built by adding up the sets of ISM components at various velocities. If different ISM components do not spatially overlap, the emergent global line profile is derived by simply adding individual line profiles of each ISM component together. Otherwise, the emergent line and continuum intensities are integrated along all the overlapped ISM components using the ray-tracing approach mentioned above (see Appendix A.3), where the foreground ISM component will absorb both line and dust photons generated by the background ISM component.

4.3. General Modeling Results

For each velocity component, we derived the first ISM component by fitting only the medium-excitation H₂O emission lines, because they are most likely to arise from the same physical region given by their similarities in both energies and line shapes (which also show a good correspondence with the CO line). Then a second ISM component is added to fit the ground-state and low-excitation emission-line features that are not accounted for in the first ISM component. In the presence of ground-state and low-excitation absorption features, we utilize the ISM component dominating FIR luminosity (normally the first component derived by fitting medium-excitation lines) as the background continuum source and add an absorbing ISM component whose physical size is allowed to vary from zero to maximum coverage. For the galaxies that have been detected in the high-excitation lines (Mrk 231 and Arp 220), we require an additional ISM component to match the high-excitation line features. Our best-fit models are obtained based on fitting to the HIFI-detected H₂O line profiles and the SPIRE/PACS H₂O data, with additional constraints from fitting the observed dust SED and CO SLED. The detailed fitting procedures are given in Appendix A.4.

We have derived a multicomponent ISM model for each of the eight galaxies with H₂O line detections. The best-fit values for each galaxy are presented in Table 4, which lists the individual results for each ISM component at different velocities (δv). The column density of clumps $N_{\text{clump}}(\text{H})$ (which is allowed to vary in the range of 1×10^{22} – $1 \times 10^{24} \text{ cm}^{-2}$ during the fitting) is usually found to be of the order $1 \times 10^{23} \text{ cm}^{-2}$. Details on the model of each galaxy are given in Appendix B.

4.3.1. Common ISM Phases among Galaxies

Although the derived models differ in some details between galaxies, we found a few general results that apply to most systems. First of all, our results reveal two typical ISM components that are shared by all galaxies—a warm component and a cold extended region (ER). The warm component has typical parameters with density of the order of $\sim 1 \times 10^5$ – 10^6 cm^{-3} , gas and dust temperature between 40 and 70 K, and column density around a few times 10^{24} cm^{-2} , while the cold component has density of the order of $\sim 1 \times 10^4 \text{ cm}^{-3}$, gas and dust temperature of 20–30 K, and column density of a few times 10^{23} cm^{-2} . The cold component is found to be much more widespread than the warm component (see Table 4).

With these two components, we are able to explain almost all of the water emission detected by HIFI. Figures 11–18 present in gray color the HIFI-detected H₂O spectra and the SPIRE/PACS H₂O data, with line widths assumed to be identical to the medium-excitation HIFI line shapes. In the figures we also show our line modeling results (red solid curve) together with individual contributions from the warm component (orange dashed curve) and cold ER (green dashed curve). From the figures it is obvious that the warm component and cold ER contribute differently to the H₂O line intensities. The cold ER produces observable line emission only in the ground-state transitions and in some cases in the o-H₂O (2_{12} – 1_{01}) line. The warm gas, on the other hand, emits almost all power in the medium-excitation lines, but contributes little to the intensity of the ground transitions.

This finding is further illustrated in Figure 3, where we show the most prominent H₂O lines predicted by our models for each ISM component. The black downward-pointing and red upward-pointing arrows denote emission and absorption, respectively. The relative line strength is coded in the line style, with solid arrows indicating the strongest ($>70\%$ of the maximum intensity, I_{max}), dashed arrows medium (70% – 10% of I_{max}), and dotted arrows weak lines with less than 10% of the maximum line intensity. Figure 3 implies that the excitation of water is very sensitive to the underlying physical conditions. In Figure 4 we present the partition functions (the fractional population of each level as a function of its energy) for each ISM component. The figure shows that only the first two or three levels (with energies below ~ 150 K) are populated in the cold ER, while water can efficiently be populated to levels with energies up to ~ 500 K in the warm gas component. Another useful feature to distinguish between the two ISM components is that the two ground-state lines seen in cold ER become invisible in the warm component. The different patterns shown in Figure 3 suggest that H₂O is powerful diagnostic tool to distinguish multiple ISM components with different physical conditions in galaxies.

4.3.2. Relation to the Dust Continuum and CO Emission

The two gas components also account for the major part of observed dust SED and CO SLED, although their generated dust SED and CO SLED are found to be very distinct. Figure 19 presents the observed dust SED and CO SLED (in black points), as well as the results predicted from our best-fit models (red lines). Overall, most of IR luminosity is generated by the warm component (its dust SED peaks at FIR wavelength), while the dust continuum emission on the long-wavelength Rayleigh–Jeans side arises mainly from the cold ER. The CO SLED of the warm component typically peaks at $8 \leq J_{\text{up}} \leq 10$ transitions and dominates the emission of middle/high- J CO lines ($7 \leq J_{\text{up}} \leq 12$). The CO gas of the warm component almost approaches LTE in levels $J_{\text{up}} \leq 6$. On the other hand, the cold ER generates most of the CO line emissions in the low- J CO transitions and its SLED peaks at $4 \leq J_{\text{up}} \leq 6$. Our models on average recover around 70% of the observed dust continuum and CO line intensities. It is worth mentioning that we find a good match between the physical sizes of the warm component (derived from model) and the starburst regions measured from high-resolution molecular gas or IR observations. This fact, in combination with its relatively high excitation of H₂O and CO, suggests that the warm component is associated with the nuclear starburst region in our sample galaxies. The cold ER, however, is likely associated with the more widespread quiescent ISM and may partly trace gas in the outer disks and spiral arms in some of our targets (e.g., in NGC 253 and NGC 4945).

4.3.3. H₂O Absorption

Another typical ISM component in our models is the bulk of the absorbing gas, which normally is located in front of the warm component that dominates the FIR luminosity. Unlike the other two ISM components that exist in all galaxies, we have only detected absorption in ground-state and other low-excitation lines within five sources. The existence of the absorbing gas seems to depend on both the galaxy orientation and geometry structure. We find that the absorbing gas is more likely to be detected in the edge-on galaxies, as in the case of NGC 4945, NGC 253, and M82 in our sample. This is not surprising given that most of the cold material in the disk of a galaxy will not be located in front of the warm dust continuum if the galaxy is seen face-on (e.g., such as in NGC 1068). The absorbing gas is very likely partly associated with the cold ER given the similar physical parameters we find for the cold ER and the absorbing material in, e.g., NGC 4945 and NGC 253. Furthermore, the partition function of the cold gas (with a significant population of the first few energy levels of water only; see Figure 4, left panel) naturally explains why absorption is usually only detected in the ground-state and the low-excitation H₂O lines. The medium-excitation H₂O lines from the background warm component can thereby pass through the cold ER almost without being absorbed. The profile of a resulting absorption line depends on how the cold ER is distributed relative to the warm component. If a large part of the warm component is covered by the cold ER, as suggested by our models for NGC 4945 and NGC 253, the absorption will appear to be very broad and deep. If only a small part of the warm component is covered, the absorption will be narrow and shallow, as is the case for M82.

Table 4
Physical Parameters Derived from Best-fit Models

Source	Component	δv (km s ⁻¹)	R_s (pc)	$n(\text{H})$ (cm ⁻³)	T_k (K)	T_{dust} (K)	$N(\text{H})$ (10 ²³ cm ⁻²)	$X_{\text{H}_2\text{O}}$	$M(\text{H})$ (10 ⁶ M_\odot)
M82	Warm	-73	17-25	1×10^4 - 10^5	80-160	50-70	10-20	$\sim 1 \times 10^{-8}$	7-30
	Warm	17-25	$\sim 1 \times 10^5$	80-160	~ 50	10-20	$\sim 1 \times 10^{-8}$	7-30	
	ER	-73, 86	60-90	$\sim 1 \times 10^5$	20-30	20-30	6-10	$\sim 1 \times 10^{-8}$	55-200
	Absorbing gas	26	10-15	$\sim 1 \times 10^4$	40-160	20-30	3-10	1×10^{-9} - 10^{-8}	0.7-6
NGC 253	Warm	23, -60	30-45	1×10^5 - 10^6	50-70	40-50	10-20	$\sim 1 \times 10^{-7}$	22-100
	ER	80, -60	160-200	$\sim 1 \times 10^5$	~ 20	~ 20	3-6	$\sim 1 \times 10^{-7}$	190-600
	Absorbing gas	-60	50-60	$\sim 1 \times 10^4$	~ 20	~ 20	6-10	$\sim 1 \times 10^{-7}$	35-90
NGC 4945	Warm	-112, 48, 141	30-40	$\sim 1 \times 10^6$	50-70	50-60	20-40	$\sim 1 \times 10^{-7}$	45-160
	ER	-112, 141	120-180	1×10^4 - 10^5	~ 20	~ 20	6-10	$\sim 1 \times 10^{-8}$	200-800
	Absorbing gas	48	50-70	1×10^4 - 10^5	~ 20	~ 20	6-10	$\sim 1 \times 10^{-8}$	40-130
NGC 1068	Warm	-18	70-100	$\sim 1 \times 10^6$	50-60	40-50	40-60	$\sim 1 \times 10^{-7}$	500-1500
	ER	-18	400-450	1×10^3 - 10^4	20-30	20-30	~ 1	$\sim 1 \times 10^{-7}$	400-500
	Outflow	-18	150-200	$\sim 1 \times 10^4$	120-180	30-40	~ 1	$\sim 1 \times 10^{-7}$	55-100
Cen A	Warm	0	7-15	1×10^5 - 10^6	50-80	40-60	10-60	1×10^{-7} - 10^{-6}	1-35
	ER	0	70-100	$\sim 1 \times 10^4$	~ 20	~ 20	6-10	$\sim 1 \times 10^{-8}$	70-250
	Absorbing gas (case I)	16	≤ 1 pc	$\sim 1 \times 10^3$	120-180	20-180	1-3	$\sim 1 \times 10^{-7}$	≤ 0.007
	Absorbing gas (case II)	16	≤ 1 pc	1×10^4 - 10^5	20-30	20-30	1-3	$\sim 1 \times 10^{-7}$	≤ 0.007
Mrk 231	Warm	50	300-550	$\sim 1 \times 10^5$	50-70	50-60	10-20	$\sim 1 \times 10^{-7}$	$(2-15) \times 10^3$
	ER	50	1000-1500	$\sim 1 \times 10^4$	30-50	~ 30	1-3	$\sim 1 \times 10^{-7}$	$(3-17) \times 10^3$
	Hot	50	60-80	$\sim 1 \times 10^6$	180-200	160-180	40-60	$\sim 1 \times 10^{-6}$	$(4-10) \times 10^2$
NGC 6240	Warm	-10	250-350	$\sim 1 \times 10^6$	60-70	60-70	10-20	$\sim 1 \times 10^{-7}$	$(15-60) \times 10^2$
	ER	-10	800-1000	1×10^3 - 10^4	120-400	20-30	1-3	$\sim 1 \times 10^{-7}$	$(16-75) \times 10^2$
Arp 220	Warm	52	120-150	1×10^4 - 10^5	50-60	30-40	40-60	1×10^{-7} - 10^{-6}	$(14-34) \times 10^2$
	ER	52	1000-1200	$\sim 1 \times 10^4$	~ 20	~ 20	10-20	$\sim 1 \times 10^{-7}$	$(25-75) \times 10^3$
	Absorbing gas	20	70-100	1×10^4 - 10^5	100-200	60-80	300-600	1×10^{-8} - 10^{-7}	$(35-150) \times 10^2$
	Hot	35	70-100	1×10^5 - 10^6	100-180	100-180	~ 100	1×10^{-6} - 10^{-5}	$(12-25) \times 10^2$

Note. The physical parameters are given for a ISM component at a single velocity, and thereby the total size and gas mass of a ISM component are sum of the values of the component at different velocities δv . The continuum covering factor of the absorbing gas can be estimated as the total size of the absorbing gas compared to the total size of the warm background gas.

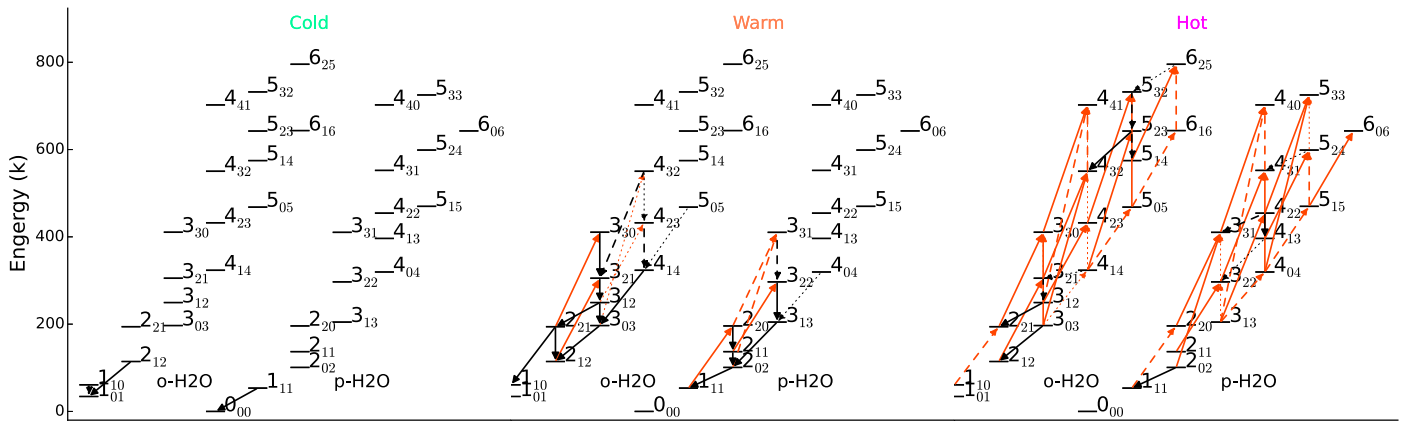


Figure 3. Prominent H₂O line features from multiple ISM components predicted by our model. The black downward-pointing and red upward-pointing arrows denote the emissions and absorptions, respectively. The solid arrows in the figure indicate the strongest lines (with intensities larger than 70% of the highest value), while the dashed arrows show the weaker lines and the dotted arrows show the weakest lines of all (with intensities less than 70% and 10% of the highest value, respectively).

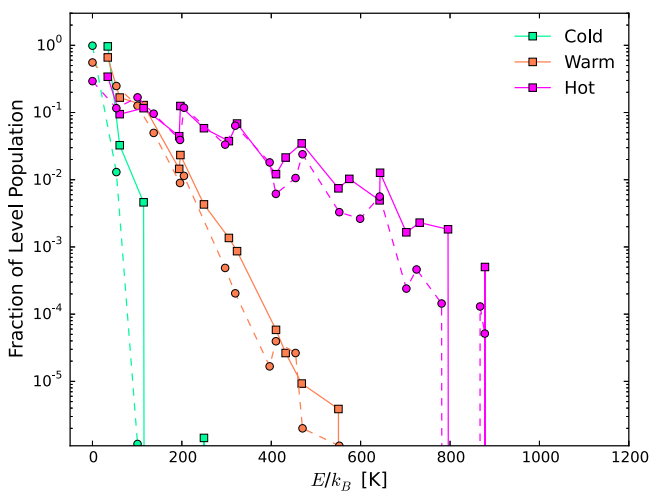


Figure 4. Distributions of water level populations of multiple ISM components. The x -axis indicates the energy of the level, and the y -axis indicates the fraction of water gas residing at each level. The squares denote level populations for o-H₂O, and the circles denote those for p-H₂O.

Note that the absorbing gas does not always have to be associated with the cold ER. For example, the ground-state/low-excitation H₂O absorption detected in Arp 220 is found to arise from warm gas (possibly associated with molecular outflows driven by the nuclear activity) against the even warmer background radiation from the hot component.

4.3.4. Hot Water in Mrk 231 and Arp 220

For the two most IR-luminous sources in our sample, Mrk 231 and Arp 220, our models require another physical component contributing significantly to H₂O line intensities. This component is required to explain the high-excitation transitions exclusively detected toward both sources (e.g., the p-H₂O (4₂₂ – 4₁₃) line). The component contains a substantial amount of hot (T_k and $T_{\text{dust}} \sim 100$ –200 K) and dense ($n(\text{H}) \geq 1 \times 10^6$) gas with high column density ($N_{\text{H}} \geq 5 \times 10^{24} \text{ cm}^{-2}$). The physical size of this hot component is found to be very compact (60–100 pc; e.g., Downes & Eckart 2007; Weiß et al. 2007). As we can see from Figure 3 (right panel), the high-excitation transitions from the hot gas are seen in both emission and absorption, most of which are not excited by the warm component. In the hot component, water

can be populated to extremely high excited levels with energies up to 800–1000 K (see Figure 4). This is due to efficient collisional excitation in this gas phase and, more importantly, due to a combination of the strong IR emission associated with the hot gas and the large number of mid-IR water transitions, which allow for efficient pumping of H₂O rotational levels to high energy states. A significant fraction of the continuum emission from the hot component, however, may be attenuated by foreground material at short wavelengths ($\lambda < 200 \mu\text{m}$), as the hot component is usually deeply buried in the galaxy nuclei (Downes & Eckart 2007). Due to its small size, the hot gas component has only a small contribution to the low- J CO transitions, but it becomes increasingly important for higher- J transitions and may dominate the CO SLED for CO lines with $J_{\text{up}} \geq 10$ (see Figure 19).

Finally, we find that the gas-phase abundance of water varies from 10^{-9} – 10^{-8} in the cold ER to 10^{-8} – 10^{-7} in the warm component and jumps to 10^{-6} – 10^{-5} in the hot gas, due to the efficient release of H₂O from dust grains into the gas phase at these high temperatures.

5. Discussion

5.1. Water Excitation in a Multiphase ISM

In order to explore the relative importance of collisions and IR pumping on the water excitation under typical conditions derived for our galaxy sample, we compute the water excitation in the warm gas component ($n(\text{H}) = 10^5 \text{ cm}^{-3}$, $T_{\text{K}} = 50 \text{ K}$, $X(\text{H}_2\text{O}) = 10^{-7}$) with the dust temperature varying from 0 to 50 K. The resulting emission and absorption lines from this calculation are shown in Figure 5, while the underlying level populations are shown in the form of Boltzmann diagrams in Figure 6. From the first panel of Figure 5, which ignores the effect of IR pumping ($T_{\text{dust}} = 0 \text{ K}$), one can see that water can be excited by collision to levels with energies up to 250–350 K (250 K for p-H₂O and 350 K for o-H₂O). This picture does not change significantly as long as the dust temperature stays below $\sim 30 \text{ K}$. Only when the dust temperatures reach 40–50 K does IR pumping start to play a dominant role by populating H₂O levels with 250 – $350 \text{ K} \leq E/k_{\text{B}} \leq 500$ – 700 K . The magenta numbers in Figure 5 indicate the peak brightness temperature of each transition in the warm gas component (averaged over the surface of a single clump). From these numbers one can see that the line strength of transitions

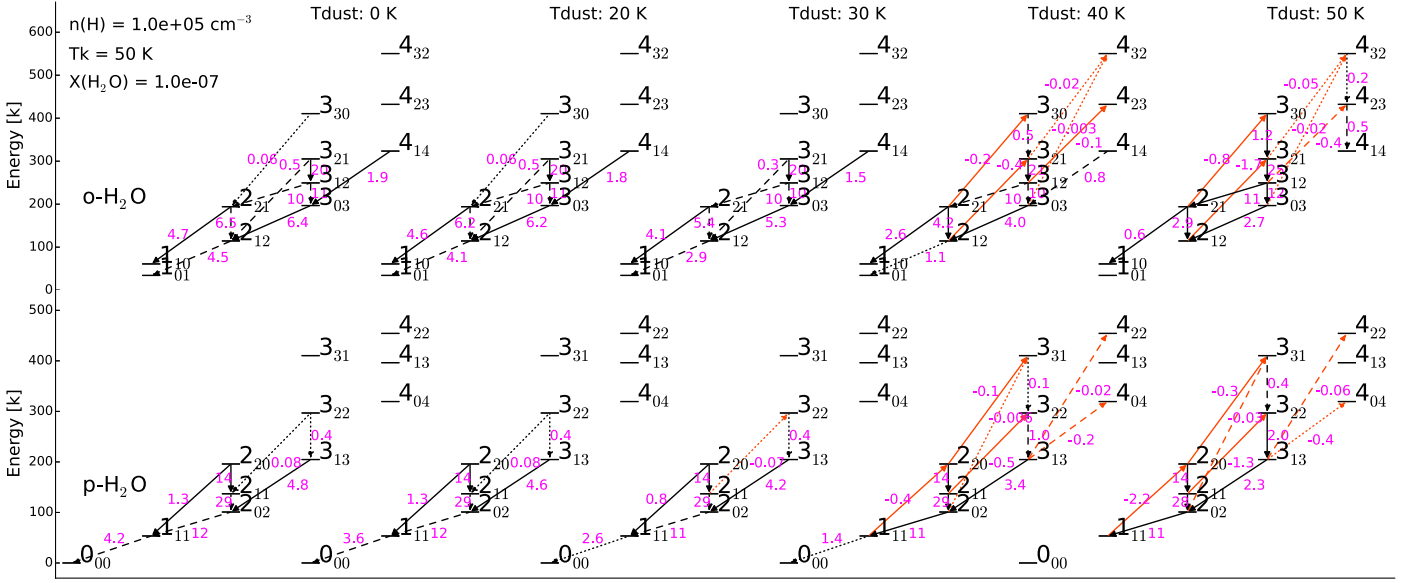


Figure 5. Water excitation of a set of clumps that have characteristic parameters of a typical warm component with fixed $n(\text{H})$, T_{K} , and $X(\text{H}_2\text{O})$, but with T_{dust} varying from 0 to 50 K. The clump with $T_{\text{dust}} = 0$ K shows the result without considering the IR pumping, and the clumps that have $T_{\text{dust}} \sim 40\text{--}50$ K display results under typical physical conditions of the warm component. The black downward-pointing arrows indicate emissions, while the red upward-pointing arrows denote absorptions that can be regarded as where IR pumping occurs. The different line styles represent different strengths of line intensities (same as Figure 3). The magenta number indicates the peak brightness temperature of each transition.

between levels $E_{\text{up}} > 250\text{--}350$ K increases rapidly with dust temperature (e.g., o-H₂O (3₃₀ – 3₂₁) and p-H₂O (3₃₁ – 3₂₂)). In contrast, line intensities for transitions with $E_{\text{up}} < 250\text{--}350$ K depend little on the dust temperature (e.g., o-H₂O (3₂₁ – 3₁₂)), and some of them (e.g., the lines with $E_{\text{up}} < 200$ K) even decrease for an increasing dust temperature, due to the increased continuum levels (e.g., o-H₂O (2₂₁ – 2₁₂)).

This behavior is more quantitatively shown in the Boltzmann diagrams in Figure 6. The collisional excitation drives the o-H₂O (p-H₂O) populations with $E/k_{\text{B}} \leq 200$ (100) K toward a Boltzmann distribution at the kinetic temperature (i.e., these levels are thermalized) and dominates the equilibrium population of the levels with $E/k_{\text{B}} \leq 350$ (250) K for o-H₂O (p-H₂O) independent of the dust temperature. Note that this happens already at densities much below the critical density of the water lines ($\sim 10^8\text{--}10^9$ cm⁻³), due to the high optical depth of these lines (see Equation (9) in Appendix A). The population of levels with energies above 250–350 K, however, is almost exclusively determined by radiative pumping. Figure 6 shows that the dust radiation field tends to drive the population of these levels (which are poorly populated by collisions) toward a Boltzmann distribution close to the dust temperature. When the dust temperature is about equal to the kinetic temperature (red points), the overall level population (from ground-state to most highly excited levels) can be fit well with a single rotational temperature (red solid line). However, we also notice that the rotational temperature can only rise to 50%–70% of the dust temperature even at the highest dust temperature ($T_{\text{dust}} = T_{\text{K}}$). We attribute this effect to the dust optical depth, i.e., it is due to the modified blackbody shape, rather than a blackbody shape, of our dust radiation field.

The dust radiation energy is absorbed by the short-wavelength, far-IR transitions (see red upward-pointing arrows in Figure 5) and then emitted by the long-wavelength, far-IR/submillimeter high-excitation lines. Under the typical conditions in the warm gas derived for our galaxy sample,

the most efficient pumping occurs at the strong 2₁₂ → 3₂₁/2₂₁ → 3₃₀/3₂₁ → 4₃₂/3₀₃ → 4₃₂/3₁₂ → 4₂₃ lines (2₁₁ → 3₂₂/2₂₀ → 3₃₁/2₀₂ → 3₃₁ lines for p-H₂O) through absorptions of far-IR photons at 75/66/58/40/79 μm (90/67/46 μm for p-H₂O), which greatly enhance the intensities of high-excitation 3₂₁ → 3₁₂/3₃₀ → 3₂₁/3₃₀ → 3₂₁/4₃₂ → 4₂₃/4₂₃ → 4₁₄ (3₂₂ → 3₁₃/3₃₁ → 3₂₂ for p-H₂O) emission lines.

We have limited the discussion here to the typical warm environment derived for our galaxy sample. Whether a transition is excited mainly by IR pumping or collision in the general case is, however, very sensitive to the ambient ISM conditions. We show the Boltzmann diagrams for other cases in Figure 21 in Appendix C. In summary, our models suggest that our observed low-excitation lines ($E_{\text{up}} < 130$ K) are collisionally excited, and most of the observed medium-excitation lines (130 K < $E_{\text{up}} < 250\text{--}350$ K) are also predominantly excited by collision. IR pumping starts to populate the medium-excitation transitions with 250–350 K < E_{up} for the typical dust fields derived in our sample and becomes increasingly important for higher transitions. For the high-excitation transitions with $E_{\text{up}} \geq 600\text{--}800$ K, IR pumping is the dominant excitation channel even for the extreme ISM conditions derived for our hot gas in Arp 220 and Mrk 231.

5.2. H₂O SLED

To investigate the SLED of H₂O within various ISM components and discuss the implications for the observed various line ratios, we present normalized H₂O SLEDs for our sample galaxies in Figure 7. The filled squares in Figure 7 indicate the observed values (for each velocity component as derived from the Gaussian decomposition), the open circles indicate the model-predicted values for the lines without observations, and the black star indicates the H₂O transition that has been used for the normalization. The kinetic temperature and the column density for each component are

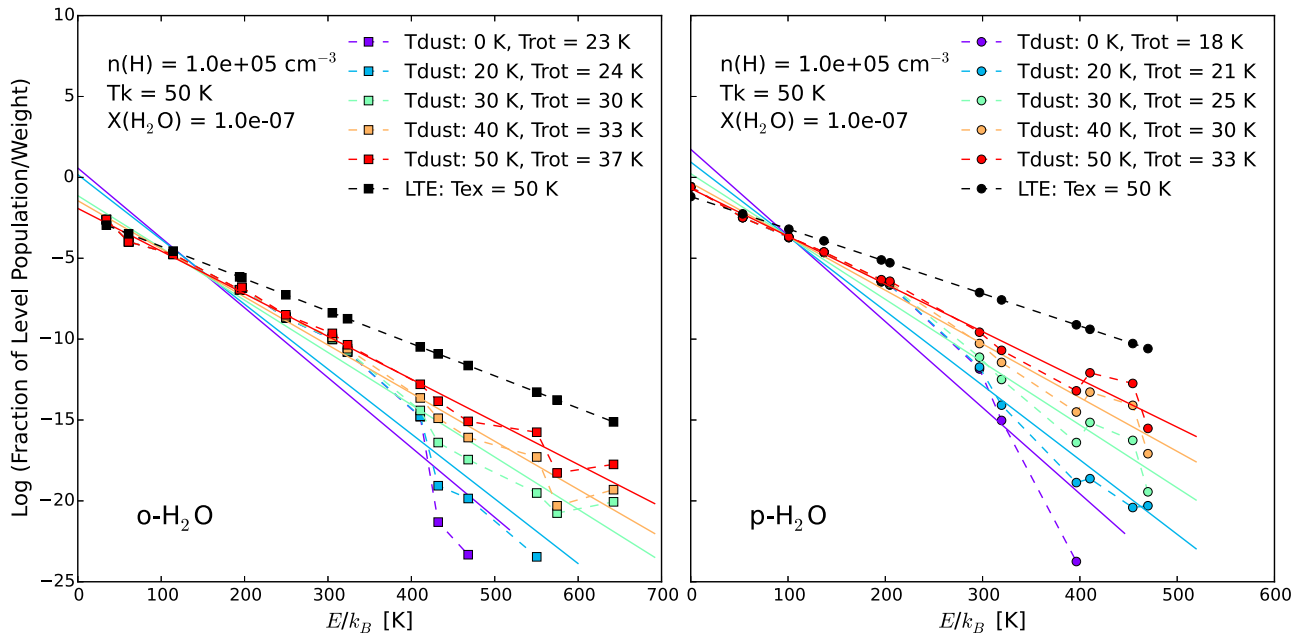


Figure 6. Level populations of water for the clumps shown in Figure 5, whose dust temperatures are labeled by different colors. The x -axis indicates the energy of each level, and the y -axis indicates the ratio of the fraction of water gas to statistical weight of level. The solid straight line presents the best fit to the data points, whose slope equals $-1/T_{\text{rot}}$. The black points show the level populations of water in LTE whose rotational temperature is assumed to be the same as T_k .

given in the plot legend, while the values for other parameters are presented in Table 4.

5.2.1. Elevated $2_{12} - 1_{01}/1_{10} - 1_{01}$ Ratios in the ER

The most remarkable feature in the first panel of Figure 7, which shows the $1_{10} - 1_{01}$ normalized H_2O SLED for the ER (note that ER for NGC 1068 also includes the component of outflow listed in Table 4), is that the $2_{12} - 1_{01}/1_{10} - 1_{01}$ line ratios are strongly boosted in galaxies with high kinetic temperatures. The $2_{12} - 1_{01}/1_{10} - 1_{01}$ line ratio varies from 0.5–2.0 in galaxies with kinetic temperature around 20–30 K (e.g., Cen A, NGC 4945, and NGC 253), to the extreme large values (~ 10 –40) in galaxies with $T_k \geq 80$ –100 K, which are well known to harbor “shocked gas” (e.g., NGC 6240 and NGC 1068; Müller Sánchez et al. 2009; Wang et al. 2012, 2014; Meijerink et al. 2013; Papadopoulos et al. 2014). As such, we suggest that the $2_{12} - 1_{01}/1_{10} - 1_{01}$ line ratio can be utilized as a good indicator of “shock condition” where gas is heated to high kinetic temperatures. The strong collisional excitation in shocks allows water to be populated above the ground states efficiently, and thereby strongly enhances the line intensity of $2_{12} - 1_{01}$.

5.2.2. Line Ratios in the Warm Gas

The second panel in Figure 7 presents the $2_{02} - 1_{11}$ normalized H_2O SLED for warm components of our galaxies. The $2_{02} - 1_{11}$ line is one of the visible lines from the warm component that can be most easily excited by collisions (therefore least affected by radiative pumping), thereby the line ratios of other transitions to it can directly reflect the effect of radiative pumping. The first notable feature inferred from the plot is that the H_2O SLED seen in medium-excitation lines (from $2_{11} - 2_{02}$ to $3_{22} - 3_{13}$) appears to be nearly flat, with their emitted line intensities comparable within a factor of ~ 2 in our sample. This implies that the upper levels of these medium-excitation lines tend to approach statistical

equilibrium, in agreement with our findings in Section 5.1 and with the analysis by González-Alfonso et al. (2014).

However, all H_2O SLEDs show a peak at the $3_{21} - 3_{12}$ line, demonstrating that the $3_{21} - 3_{12}$ line has relatively stronger intensities since these medium-excitation lines have similar line frequencies ($\nu \sim 1000$ –1200 GHz). The underlying reason is that the upper level 3_{21} not only is approximately thermalized by collisions (as the other lower levels) but also is one of the levels that can be most easily excited by IR pumping (see Figures 5 and 6). So the $3_{21} - 3_{12}$ line usually exhibits higher-excitation temperature. The $3_{21} - 3_{12}$ line is found to be optically thinner ($\tau_{\text{line}} \simeq 1$) than the lower-excited medium-excitation lines ($\tau_{\text{line}} > 1$), due to its required higher-excitation energy. Therefore, the $3_{21} - 3_{12}/2_{02} - 1_{11}$ line ratios are mostly sensitive to the total H_2O column density ($N(\text{H}_2\text{O})$) and are enhanced in galaxies with higher $N(\text{H}_2\text{O})$. The $3_{21} - 3_{12}/2_{02} - 1_{11}$ ratio exhibits the largest value (~ 5) in Arp 220, which has the highest $N(\text{H}_2\text{O})$ ($\sim 6 \times 18 \text{ cm}^{-2}$), moderate values (~ 2) in galaxies with $N(\text{H}_2\text{O}) \sim 1 \times 17 \text{ cm}^{-2}$ (e.g., NGC 4945, NGC 253, NGC 6240), and the smallest value (~ 1.2) in M82, which has the lowest $N(\text{H}_2\text{O})$ ($\sim 1 \times 16 \text{ cm}^{-2}$). Yet, not all galaxies (e.g., Cen A and NGC 1068) follow this trend, indicating that other parameters, such as the dust temperature as suggested by González-Alfonso et al. (2014), may also influence this ratio. A comparable trend is also seen in the $2_{20} - 2_{11}$ line, which is located in a position of the para- H_2O energy diagram similar to that of the $3_{21} - 3_{12}$ line in the ortho- H_2O energy diagram. The $2_{20} - 2_{11}$ line also exhibits smaller line optical depth ($\tau_{\text{line}} \simeq 1$) and slightly higher excitation temperature than other para- H_2O medium-excitation lines. We have not found a strong variance of H_2O SLEDs over dust temperatures, possibly due to the small range of dust temperatures in our warm components or physically suggesting that radiative pumping does not play a dominant role in exciting these medium-excitation lines. Finally, we find that the lines that are most sensitive to

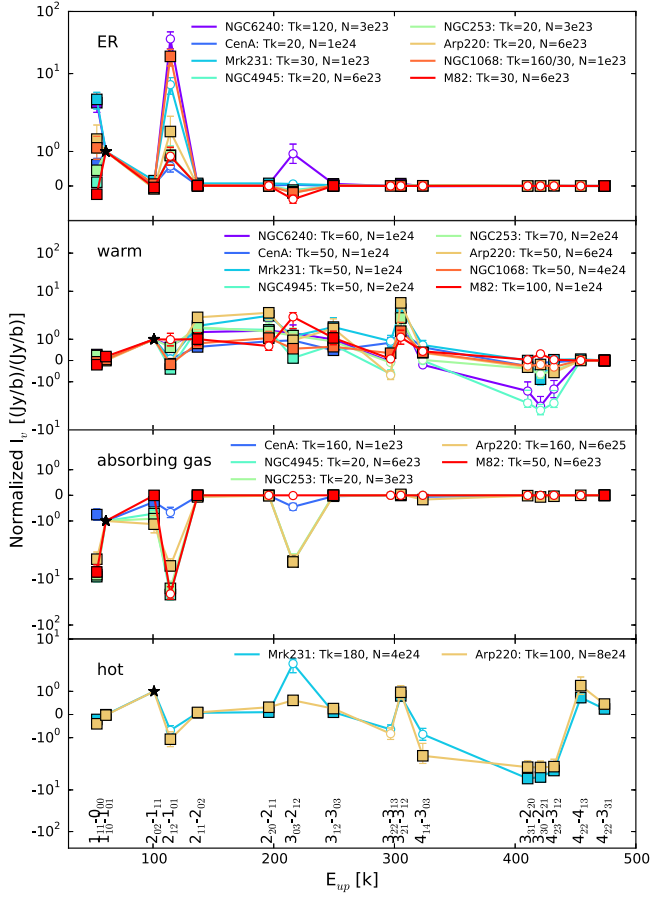


Figure 7. Normalized H₂O SLED for multiple ISM components. The black star indicates the H₂O transition, which is used to normalize all the other H₂O lines. The filled squares indicate the observed values for each ISM component that are derived from Gaussian decomposition. The open circles denote the transitions without observations whose intensities are predicted by our models. The best-fit values for gas kinetic temperature T_k (in units of K) and hydrogen column density N (in units of cm^{-2}) for each ISM component are given in the legends. Note that the upper levels of $3_{03} - 2_{12}$, $3_{30} - 2_{21}$, and $4_{22} - 3_{31}$ are shifted to the right by 20, 10, and 20 K, respectively, for clarity.

collision ($3_{03} - 2_{12}$ and $2_{12} - 1_{01}$) have larger intensities in galaxies with higher kinetic temperatures (e.g., M82).

5.2.3. The Line Ratios in the Absorbing Gas

The third panel in Figure 7 shows the H₂O SLEDs for the absorbing gas of five galaxies in our sample, which are normalized to the absolute line intensity of the $1_{10} - 1_{01}$ line. The first conclusion inferred from this plot is that the absorption is often observed only up to the $2_{12} - 1_{01}$ line. This is because higher levels are usually not populated for this component. We further find that the H₂O SLED of absorbing gas is closely related to the dust SEDs (T_{dust} and τ_{dust}) of both the background continuum source and the absorbing gas. If the dust continuum from the absorbing gas is negligible, then the ratios of absorption lines depend mainly on the flux ratios of background continuum sources at the line frequencies, as the low-excitation absorptions ($1_{11} - 0_{00}$, $1_{10} - 1_{01}$, $2_{12} - 1_{01}$) are often found to be optically thick. We find that the galaxies whose absorbing gas contributes little to the dust continuum (e.g., $T_{\text{dust}}^{\text{abs}} \simeq 20\text{--}30$ K, $\tau_{100\mu\text{m}}^{\text{abs}} \simeq 0.2$ in NGC 4945, M82, and NGC 253) have the $1_{11} - 0_{00}/1_{10} - 1_{01}$ ratios around 8–10 and the $2_{12} - 1_{01}/1_{10} - 1_{01}$ ratios around

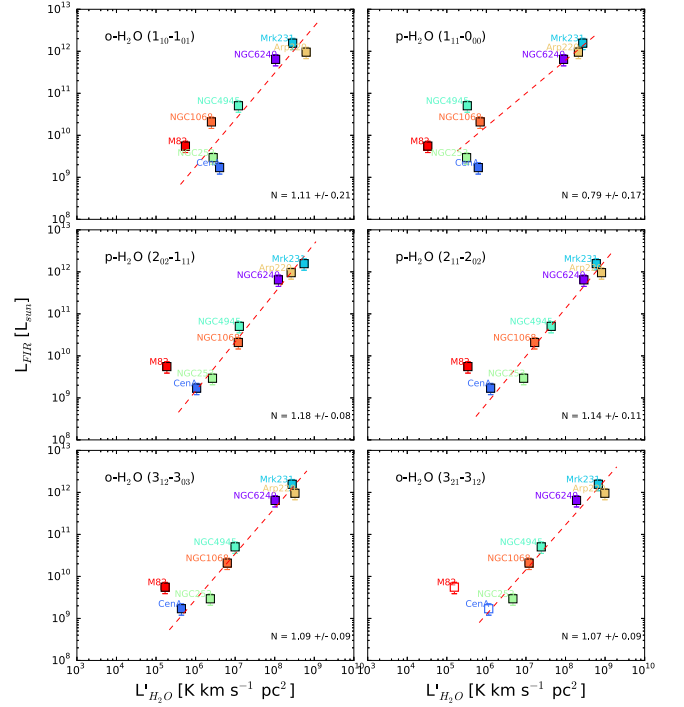


Figure 8. Correlations between $L'_{\text{H}_2\text{O}}$ and L_{FIR} for our sample galaxies. The line luminosities of o-H₂O ($1_{10} - 1_{01}$) and p-H₂O ($1_{11} - 0_{00}$) are calculated without considering the absorptions. The open squares in the last panel indicate the galaxies whose $L'_{\text{H}_2\text{O}}(3_{21} - 3_{12})$ are estimated from our model, as no observations have been obtained. The red dashed line denotes the best-fitting correlation whose slope is given by N .

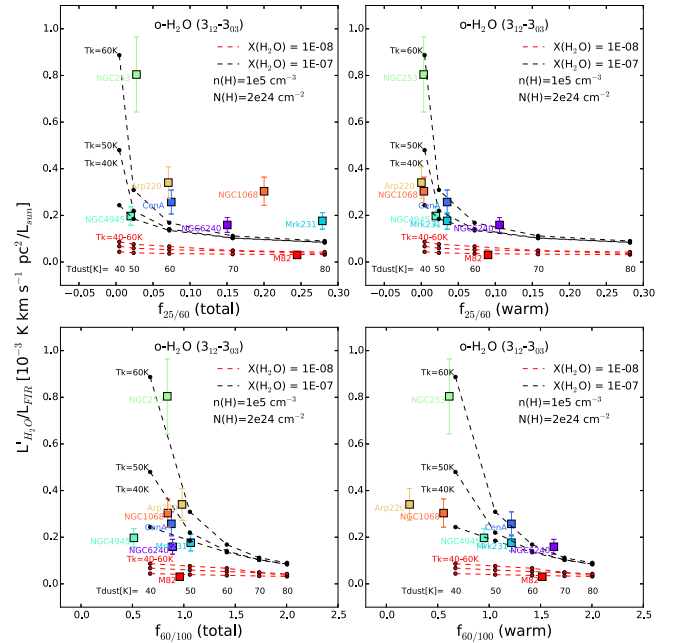


Figure 9. $L'_{\text{H}_2\text{O}}(3_{12} - 3_{03})/L_{\text{FIR}}$ vs. f_{25}/f_{60} (top) and f_{60}/f_{100} (bottom), respectively. The left column panels show the observed $L'_{\text{H}_2\text{O}}/L_{\text{FIR}}$ ratios vs. the observed total IR colors, while the right column panels present the observed $L'_{\text{H}_2\text{O}}/L_{\text{FIR}}$ vs. the IR colors derived from the warm component only. The dashed curve presents our modeled $L'_{\text{H}_2\text{O}}/L_{\text{FIR}}$ –IR color correlation for a set of warm components with fixed T_k and $X(\text{H}_2\text{O})$, where different filled circles indicate various dust temperatures whose values are labeled at the bottom of the plot. The values of T_k are labeled in the text, while various $X(\text{H}_2\text{O})$ are given by different colors. The gas density and column density of all models are fixed to the values labeled in the plots.

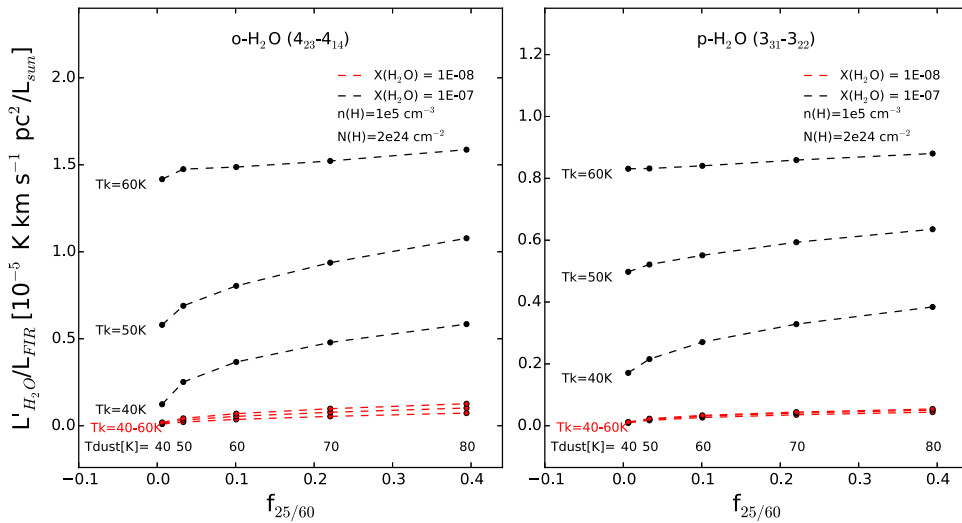


Figure 10. Modeled $L'_{\text{H}_2\text{O}}/L_{\text{FIR}}-f_{25}/f_{60}$ for two H_2O lines that are supposed to be excited dominantly by IR pumping. We have no observations for these two lines in all our sample galaxies. For explanation of the symbols used in the plots, see Figure 9.

20–30, which are very close to the dust continuum 1113/557 GHz ($S_{1113\text{GHz}}/S_{557\text{GHz}} \simeq 8.5$) and 1670/557 GHz ($S_{1670\text{GHz}}/S_{557\text{GHz}} \simeq 23$) flux ratios of the background source (i.e., the warm component). However, once the dust continuum from the absorbing gas becomes significant (e.g., $T_{\text{dust}}^{\text{abs}} \simeq 60$ –80 K, $\tau_{100\mu\text{m}}^{\text{abs}} \geq 1.5$ in Arp 220), the $l_{11} - 0_{00}/l_{10} - l_{01}$ and $2_{12} - 1_{01}/l_{10} - l_{01}$ line ratios will decrease with increasing column density of the absorbing gas (as the dust continuum $S_{1113\text{GHz}}/S_{557\text{GHz}}$ and $S_{1670\text{GHz}}/S_{557\text{GHz}}$ flux ratios are smaller at lower dust temperature and higher column density). In the cases where the absorption lines are optically thin (in this case, $N(\text{H}_2\text{O}) \leq 1 \times 15 \text{ cm}^{-2}$), however, our modeling suggests that the $l_{11} - 0_{00}/l_{10} - l_{01}$ and $2_{12} - 1_{01}/l_{10} - l_{01}$ ratios can be significantly larger than the values estimated from the background dust continuum. We do not find optically thin absorption lines in our work. The $l_{11} - 0_{00}/l_{10} - l_{01}$ and $2_{12} - 1_{01}/l_{10} - l_{01}$ ratios should be always larger than 1, if the background continuum is a modified blackbody spectrum. Otherwise, it suggests that the background continuum may be a radio source with a power-law spectrum just as in the case of Cen A (see Appendix B for more details on Cen A). Thus, the ratios of H_2O absorption lines are able to provide valuable hints on the properties of background continuum sources even without spatially resolving the nuclear regions.

5.2.4. The H_2O SLED of the Hot Gas

The last panel in Figure 7 presents the $2_{02} - l_{11}$ normalized H_2O SLED of the hot component, which has only been found in the ULIRGs in our sample (Arp 220 and Mrk 231). The H_2O SLED of the hot component displays similar features to the warm component in medium-excitation lines but displays a quite distinct behavior in high-excitation lines, which show strong detections in both emission and absorption. Considering its high dust temperature and other extreme physical conditions, the hot component is possibly associated with a dusty toroid heated by an AGN (e.g., Downes & Eckart 2007; Weiß et al. 2007).

5.3. Dependence of the Water Line Intensities on the FIR Continuum Properties

5.3.1. The $L'_{\text{H}_2\text{O}}-L_{\text{FIR}}$ Correlation

We present the correlations between L_{FIR} (40–120 μm) and $L'_{\text{H}_2\text{O}}$ for the two ground transitions and four medium-excitation lines in Figure 8. Note that we adopted only the emission luminosity, rather than total line luminosity, for the two ground-state lines to avoid biases due to foreground absorption. Figure 8 shows that M82 deviates significantly from the overall correlations in particular for the medium-excitation lines. We attribute this finding to its lower water abundance (for more details on M82 see Appendix B) and excluded M82 from our correlation analysis between $L'_{\text{H}_2\text{O}}$ and L_{FIR} .

We find that all medium-excitation transitions show a tight nearly linear $L'_{\text{H}_2\text{O}}-L_{\text{FIR}}$ correlation, which agrees well with the linear correlation found in the larger galaxy sample observed with the SPIRE/FTS (Yang et al. 2013). As our model suggests that collision plays a significant role in exciting most of the medium-excitation transitions (see Figures 5 and 6), this linear correlation is not simply a consequence of IR pumping as suggested by Yang et al. (2013). Our models show that the medium-excitation transitions probe the same physical regions of galaxies where most of FIR emission is generated (i.e., the warm component; see Section 4.3), suggesting that the observed correlations between FIR and the medium-excitation line are mostly driven by the sizes of the FIR- and water-emitting regions in these lines.

This view is also supported by the $L'_{\text{H}_2\text{O}}-L_{\text{FIR}}$ correlations of the two ground-state lines, which we present here for the first time. While the $L'_{\text{H}_2\text{O}}-L_{\text{FIR}}$ correlation for the o- H_2O ($l_{10} - l_{01}$) line has an approximately linear slope ($N = 1.11 \pm 0.21$), the p- H_2O ($l_{11} - 0_{00}$) line shows a slope slightly below unity ($N = 0.79 \pm 0.17$). In addition, the correlations for ground-state lines have smaller Spearman rank correlation coefficients (~ 0.82) compared with those for medium-excitation lines (~ 0.97), suggesting that the former are less correlated with L_{FIR} compared with the latter. This is not surprising given that the ground-state lines are found to

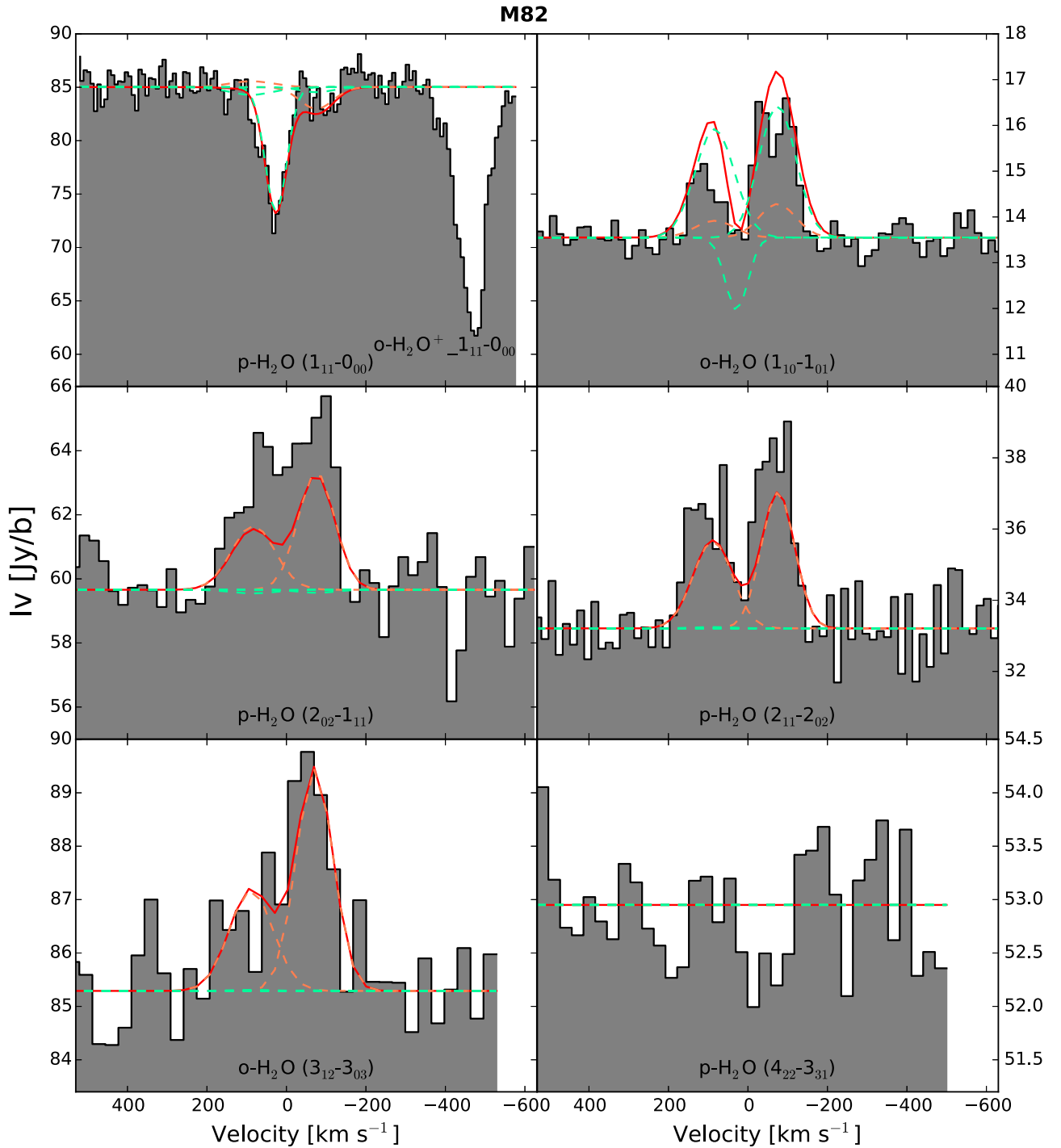


Figure 11. Observed H₂O spectra (gray histogram) and the modeling results (red solid curve) of M82. The individual contributions from the warm component and cold ER are displayed by orange and green colors, respectively. The horizontal lines indicate the observed continuum flux level. The panels are ordered according to the upper level energies of the lines. On each panel, we shift the systemic velocity of the galaxy to $v_{\text{LSR}} = 0 \text{ km s}^{-1}$.

arise mostly from the cold ERs of galaxies, which contribute less to FIR luminosity.

5.3.2. Dependence on $L'_{\text{H}_2\text{O}}/L_{\text{FIR}}$ on the Dust Color

In order to investigate the variations of luminosity ratios ($L'_{\text{H}_2\text{O}}/L_{\text{FIR}}$) with T_{dust} , we have analyzed the correlation between $L'_{\text{H}_2\text{O}}/L_{\text{FIR}}$ and the IR colors (f_{25}/f_{60} and f_{60}/f_{100}) for the medium-excitation lines. All medium-excitation lines

display a similar trend, and we show as an example the relation for the o-H₂O (3₁₂ – 3₀₃) line in Figure 9. The left column of Figure 9 shows the observed $L'_{\text{H}_2\text{O}}/L_{\text{FIR}}$ ratios versus the observed total IR colors for our sample galaxies (with f_{25}/f_{60} in the top row and f_{60}/f_{100} in the bottom row), while the right column presents the observed $L'_{\text{H}_2\text{O}}/L_{\text{FIR}}$ versus the IR colors derived from the warm component only.

The first conclusion inferred from Figure 9 is that we do not find a clear trend where the observed $L'_{\text{H}_2\text{O}}/L_{\text{FIR}}$ ratios vary

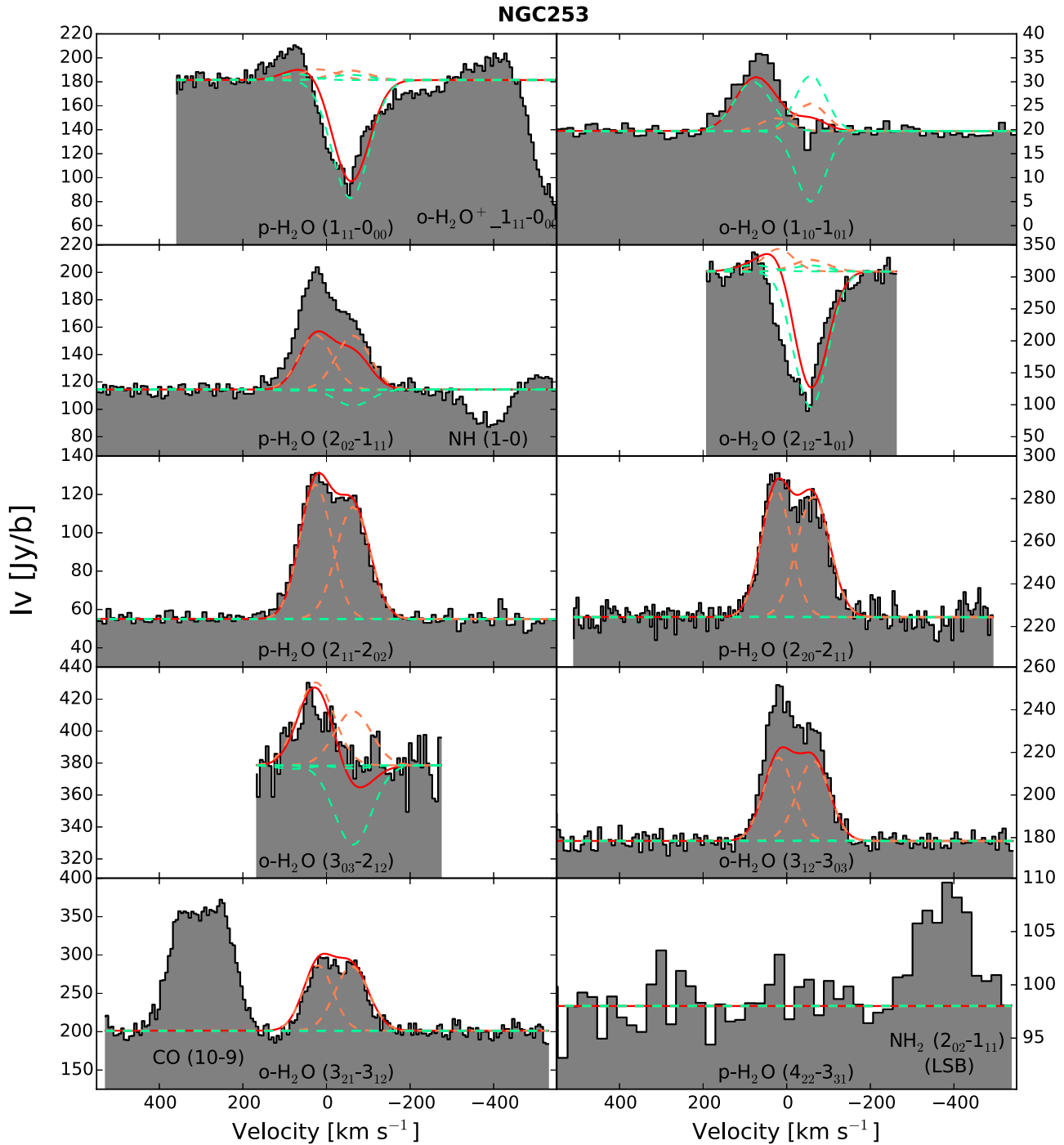


Figure 12. Observed H_2O spectra (gray histograms) and the modeling results (red solid curve) of NGC 253. For explanation of the symbols used in the plots, see Figure 11.

with the observed total IR colors (for both f_{25}/f_{60} and f_{60}/f_{100}); however, we find that the observed $L'_{\text{H}_2\text{O}}/L_{\text{FIR}}$ ratios decrease with the increasing values of IR colors estimated from the warm component only. The first fact could be due to the different physical origins of the observed $L'_{\text{H}_2\text{O}}/L_{\text{FIR}}$ ratios and IR colors. The former arises mainly from the warm component, while the observed f_{25}/f_{60} and f_{60}/f_{100} will be contaminated by other ISM components. The f_{25}/f_{60} will be greatly enhanced if a strong AGN is present (e.g., Mrk 231, NGC 1068, and Arp 220), while the f_{60}/f_{100} will be decreased largely if the cold ER

contributes significantly to the total IR luminosity. We can see from the right column of Figure 9 that once the contamination in IR colors from other components is removed, $L'_{\text{H}_2\text{O}}/L_{\text{FIR}}$ ratios start to show a correlation with IR colors. Within a larger sample of galaxies that are detected by the SPIRE/FTS, however, a slight trend that the $L'_{\text{H}_2\text{O}}/L_{\text{IR}}$ ratio decreases with increasing f_{25}/f_{60} has been observed (Yang et al. 2013).

To further understand how the $L'_{\text{H}_2\text{O}}/L_{\text{FIR}}$ ratios vary with IR colors, we have modeled the relations between $L'_{\text{H}_2\text{O}}/L_{\text{FIR}}$ and IR colors for a set of warm components with variable dust

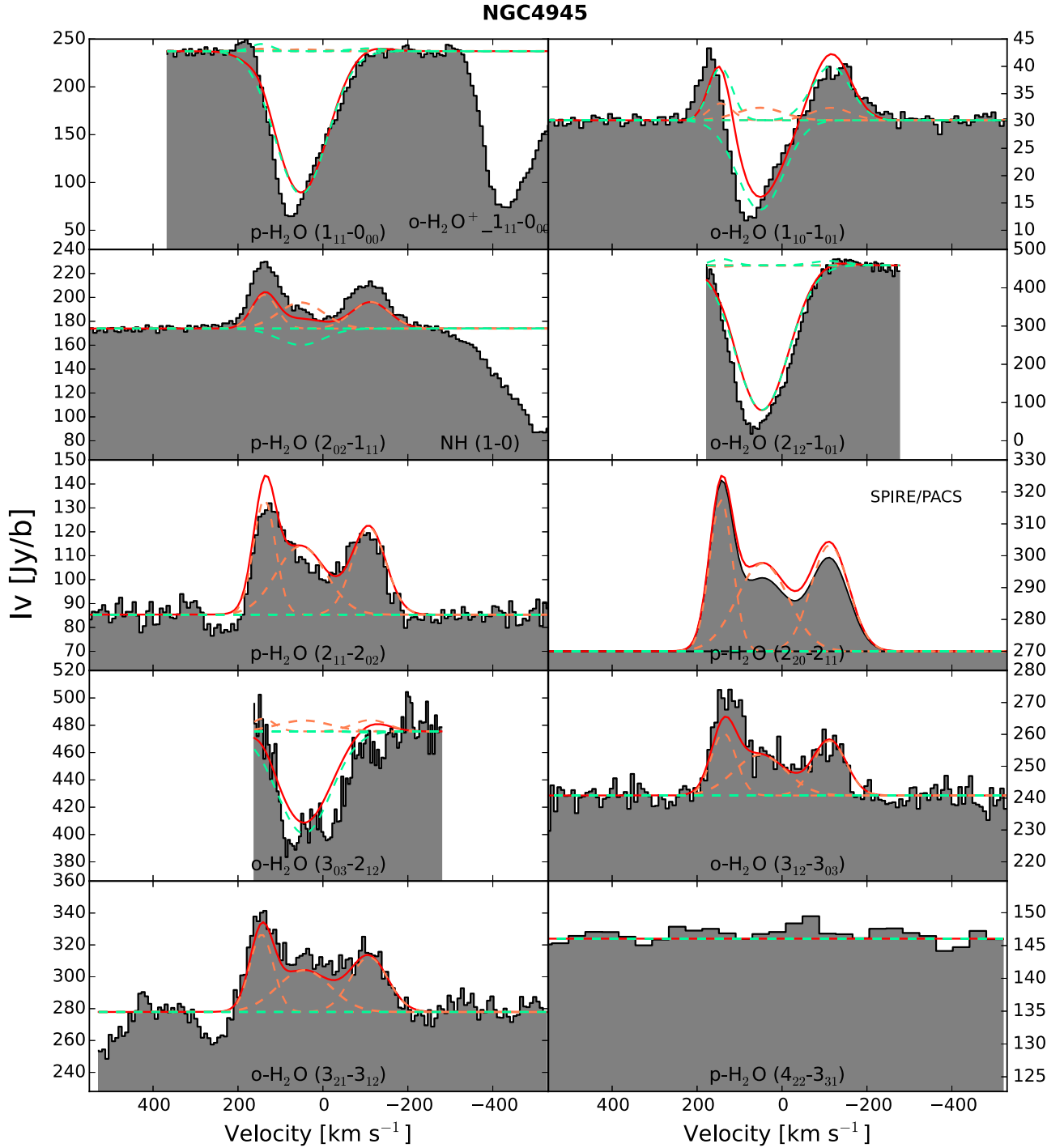


Figure 13. Observed H_2O spectra (gray histograms) and the modeling results (red solid curve) of NGC 4945. The black solid line in the subpanel of $\text{p-H}_2\text{O}$ ($2_{20} - 2_{11}$) with text “SPIRE/PACS” presents the estimated line profile from HIFI-detected medium-excitation lines, whose integrated intensity is derived by SPIRE/PACS. For explanation of the other symbols used in the plots, see Figure 11.

temperatures, kinetic temperatures, and water abundances but with a fixed gas density ($n(\text{H}) = 1 \times 10^5 \text{ cm}^{-3}$) and column density ($N(\text{H}) = 2 \times 10^{24} \text{ cm}^{-2}$). The dashed curves in Figure 9 present the model results for the warm components. One can see that our model predicts a strong decrease of $L'_{\text{H}_2\text{O}}/L_{\text{FIR}}$ with increasing f_{25}/f_{60} and f_{60}/f_{100} (i.e., T_{dust}), which is in very good correspondence with the trend seen in the warm component only.

We further find that the constant T_{k} lines drop much faster at the low- T_{dust} end, where most of our sample galaxies reside,

while they decrease very little at the high- T_{dust} end. This is because the $\text{o-H}_2\text{O}$ ($3_{12} - 3_{03}$) line (along with the other medium-excitation lines in our work) is excited largely by collisions at low T_{dust} ($T_{\text{dust}} \leq T_{\text{k}}$), and therefore its line intensity does not increase significantly with T_{dust} , but is greatly enhanced for increasing kinetic temperature. That is why NGC 253 stands out significantly in the plot, because it has a relatively high T_{k} compared to its T_{dust} . At the high- T_{dust} end ($T_{\text{dust}} > T_{\text{k}}$), where IR pumping becomes more important, the line intensity $L'_{\text{H}_2\text{O}}$ increases rapidly with T_{dust} , and

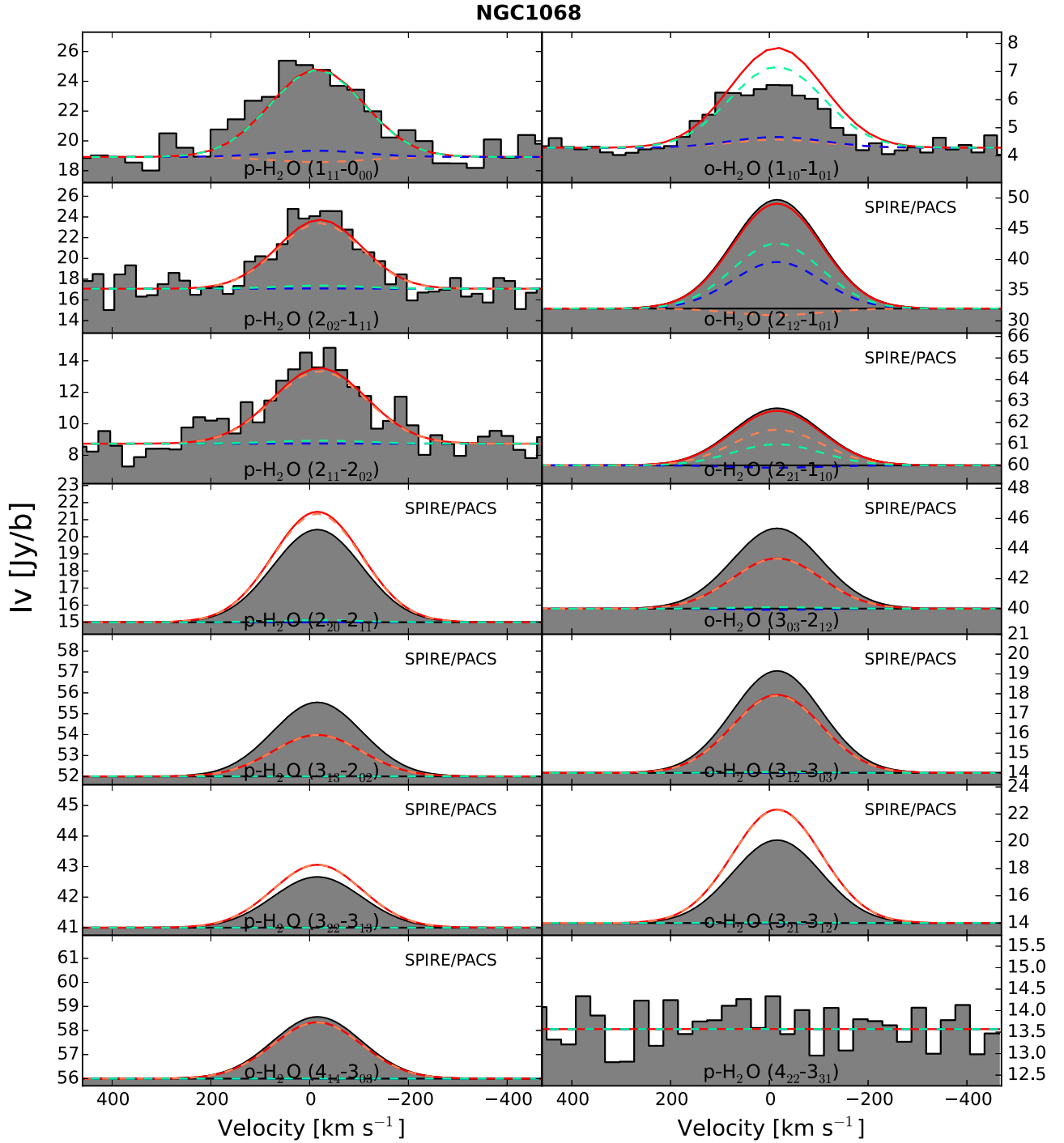


Figure 14. Observed H₂O spectra (gray histograms) and the modeling results (red solid curve) of NGC 1068. The black solid lines in the subpanels with text “SPIRE/PACS” present the estimated line profiles for SPIRE/PACS-detected lines, whose line shapes are assumed to be the same as the HIFI-detected medium-excitation lines. The blue dashed lines denote the modeling results of the shocked outflow gas in NGC 1068. For explanation of the other symbols used in the plots, see Figure 11.

therefore its ratio to L_{FIR} remains almost constant for increasing T_{dust} (i.e., IR colors), and it will show no dependence on T_{k} . The $L'_{\text{H}_2\text{O}}/L_{\text{FIR}}$ ratio of o-H₂O ($3_{12} - 3_{03}$) is found to be always larger than 1×10^{-4} if $X(\text{H}_2\text{O}) \geq 1 \times 10^{-7}$ and decreases rapidly with decreasing water abundance.

For the lines that are excited dominantly by IR pumping (such as the p-H₂O ($3_{31} - 3_{22}$) and the o-H₂O ($4_{23} - 4_{14}$) lines, which have both not been observed in our work), our

model predicts that the $L'_{\text{H}_2\text{O}}/L_{\text{FIR}}$ ratios have a different dependence on the IR color than the lines mainly excited by collisions. As shown in Figure 10, these lines do not show a decreasing but an increasing $L'_{\text{H}_2\text{O}}/L_{\text{FIR}}$ ratio for an increasing dust temperature. A similar trend is found by González-Alfonso et al. (2014), which suggests that the $L'_{\text{H}_2\text{O}}/L_{\text{FIR}}$ ratio is expected to decrease with increasing T_{dust} for all lines with $E_{\text{up}} < 300$ K but increases with T_{dust} for the high-excitation

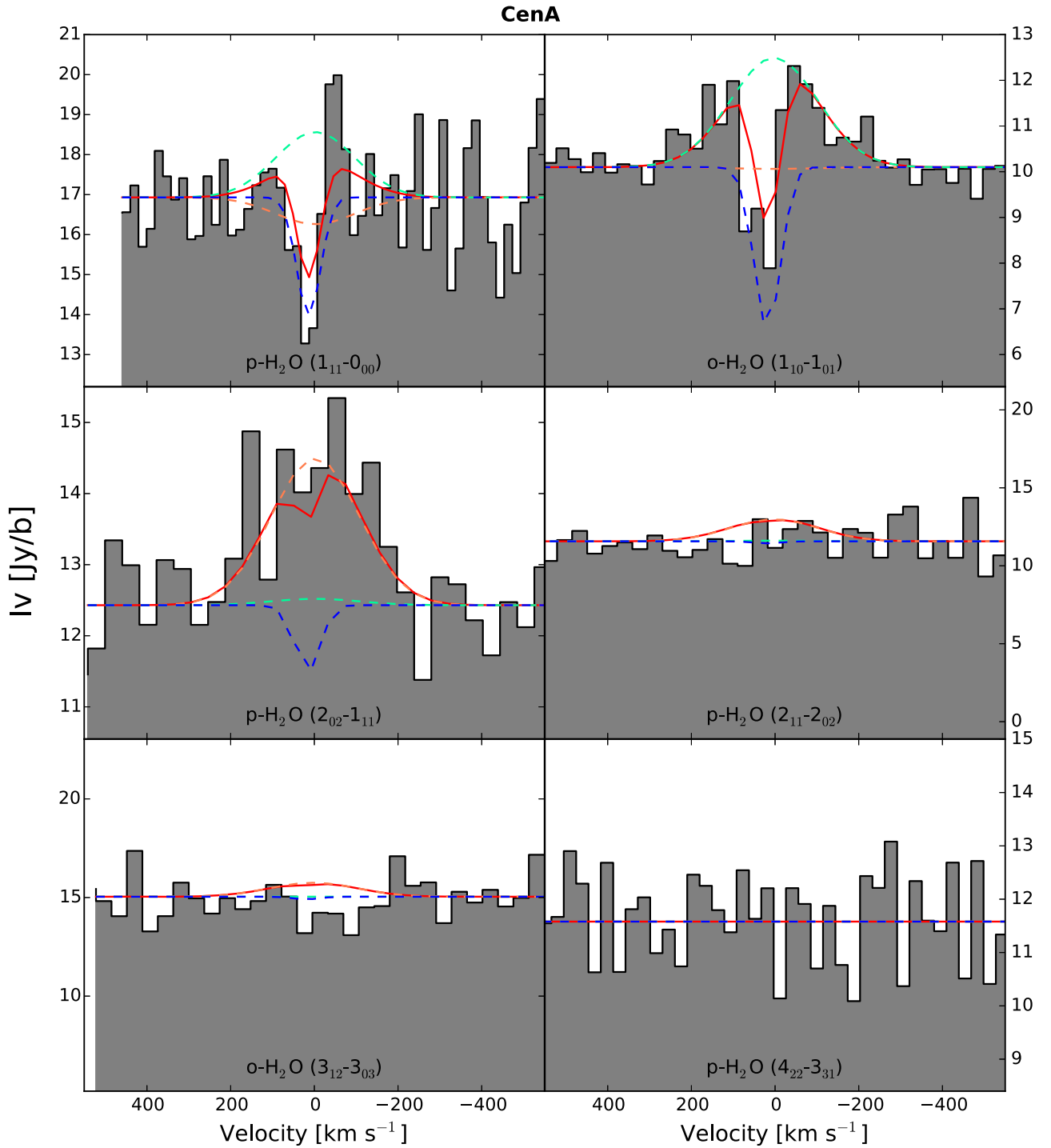


Figure 15. Observed H₂O spectra (gray histograms) and the modeling results (red solid curve) of Cen A. The blue dashed curves denote the absorption of shocked gas toward the power-law continuum of the radio core. For explanation of other symbols used in the plots, see Figure 11.

H₂O lines with $E_{\text{up}} > 400$ K. The modeling results shown in Figures 9 and 10 imply that the observed correlation between $L'_{\text{H}_2\text{O}}/L_{\text{FIR}}$ and IR colors can be utilized as a diagnostic tool to distinguish between different excitation channels (i.e., collisional excitation and IR pumping) of H₂O lines. That is, if the $L'_{\text{H}_2\text{O}}/L_{\text{FIR}}$ ratio is found to decrease with increasing IR color, then the line is possibly excited mainly by collision within the sample; otherwise, the line may be excited dominantly by IR pumping.

5.4. The Implication of Line Profiles

Unlike the line profiles of other molecules (such as CO or HCN), the H₂O line shapes strongly depend on the involved energy levels. The absorption-free medium-excitation H₂O transitions show line profiles in agreement with or slightly narrower than CO. Our model suggests that the medium-excitation H₂O lines stem from the same volume that gives rise to the FIR emission. This leads to a tight linear correlation between the luminosities of medium-excitation lines and FIR.

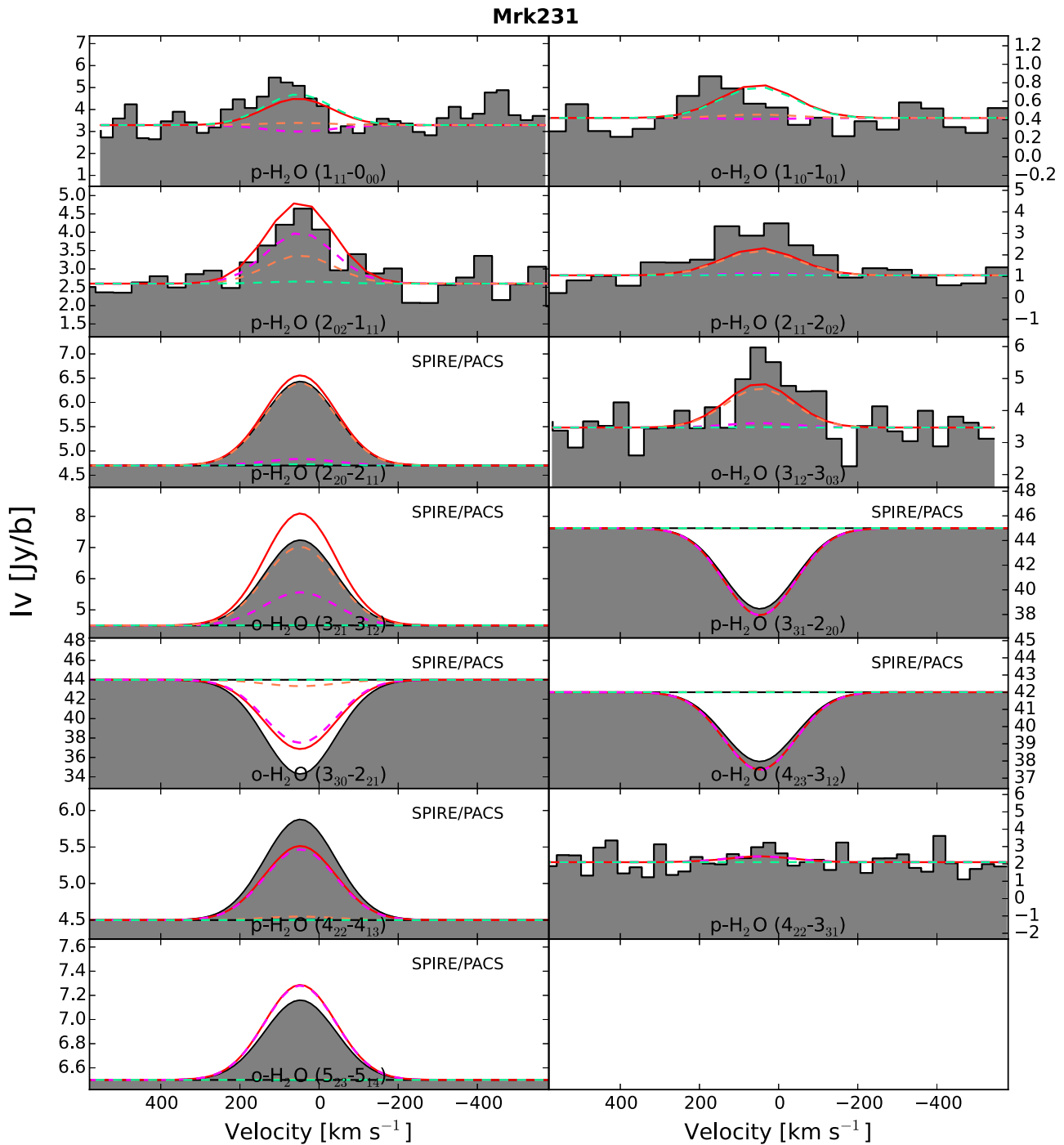


Figure 16. Observed H_2O spectra (gray histograms) and the modeling results (red solid curve) of Mrk 231. The individual contributions from the cold ER, warm component, and hot component are displayed by green, orange, and magenta colors, respectively. The black solid lines in the subpanels with text “SPIRE/PACS” present the estimated line profiles for SPIRE/PACS-detected lines, whose line shapes are assumed to be the same as the HIFI-detected medium-excitation lines. For explanation of the other symbols used in the plots, see Figure 11.

We therefore conclude that the medium-excitation H_2O lines are good probes to study the kinematics of the starburst/SF gas, e.g., they can serve as kinematic probes of the FIR emission region.

The line profiles of ground-state and low-excitation lines are found to differ from galaxy to galaxy. Some of these lines show pure absorption, while the others show pure emission or a mix of both. The emission of the ground-state lines often spans a larger velocity range than the medium-excitation transitions (e.g., NGC 4945, NGC 253, and NGC 1068), implying that the

ground-state emission arises from a more extended physical region. This is most prominently seen in NGC 253, where the $\text{o-H}_2\text{O}$ ground-state line is $\sim 60 \text{ km s}^{-1}$ wider than the medium-excitation lines. The absorption-line shapes and centroids depend on the dynamics of the foreground gas and its location related to the background continuum source. Although detailed kinematics of galaxies are not considered in our work, some important information can still be obtained by comparing the line profiles of H_2O with those of other species (e.g., CO, HF) and the high spatial resolution CO observations.

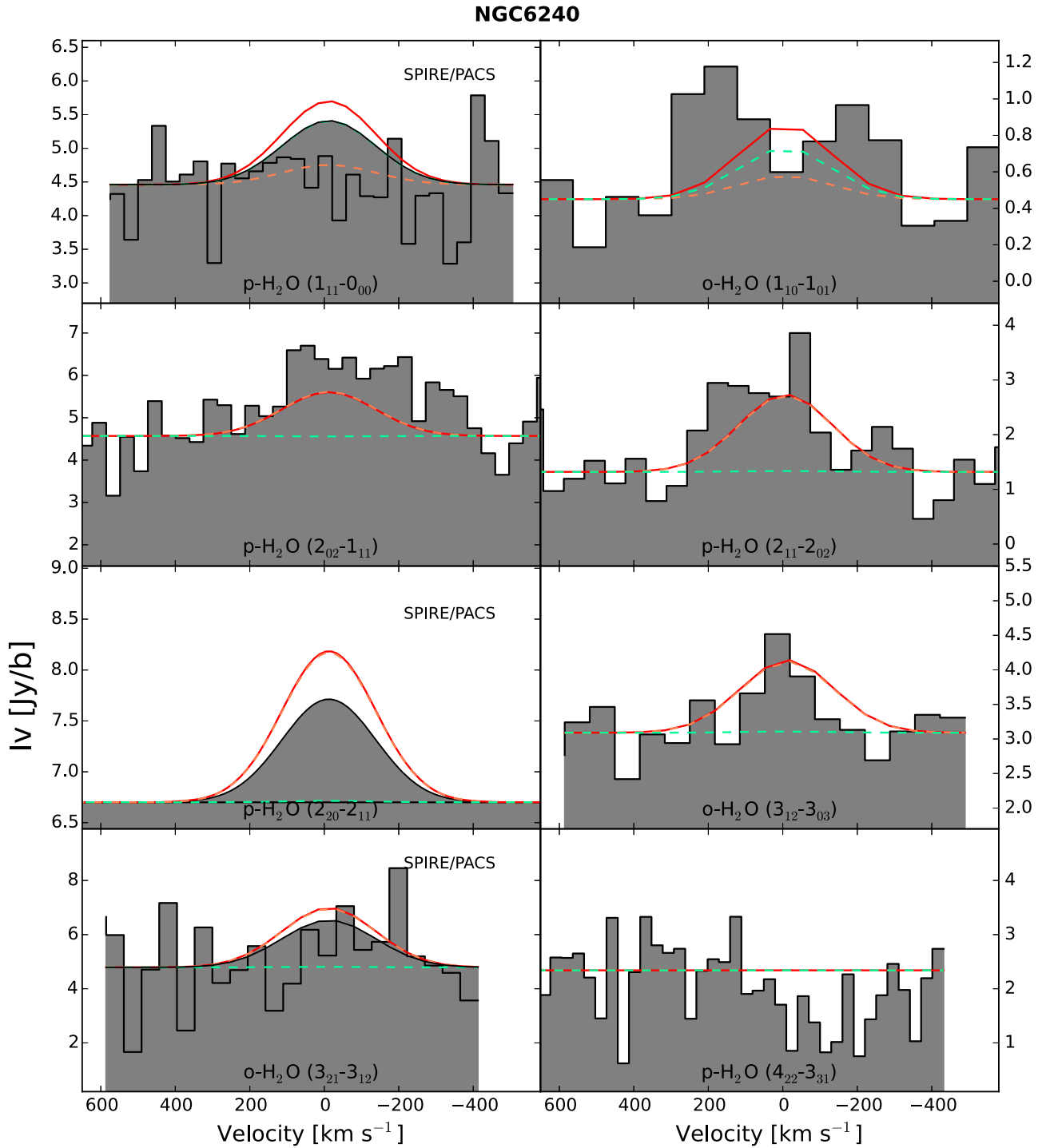


Figure 17. Observed H₂O spectra (gray histograms) and the modeling results (red solid curve) of NGC 6240. For explanation of the symbols used in the plots, see Figure 11. The p-H₂O ($1_{11} - 0_{00}$) and o-H₂O ($3_{21} - 3_{12}$) lines have not been detected by HIFI, so their integrated fluxes from *Herschel*/SPIRE were used in the modeling.

We noticed that most H₂O absorption profiles have line shapes that deviate from pure Gaussian profiles and often show P Cygni or inverse P Cygni profiles indicative of noncircular motions driven by gas outflow or infall. For example, the absorption of NGC 4945 is better fitted by a broad Gaussian component centered close to the systemic velocity plus a redshifted (by ~ 80 km s⁻¹) narrower Gaussian component. The latter is possibly related to an infall of gas in the molecular ring

or noncircular motion (for instance, in a barred potential; van der Tak et al. 2016). The absorption of NGC 253 shows a P Cygni profile that has also been observed in other gas species (e.g., HI and HF; Koribalski et al. 1995; Monje et al. 2014), and is likely connected to the molecular outflow observed in CO (Bolatto et al. 2013). By comparing the absorptions of M82 with high-resolution CO maps, Weiß et al. (2010) found that the absorption of M82 only displays a good agreement with the

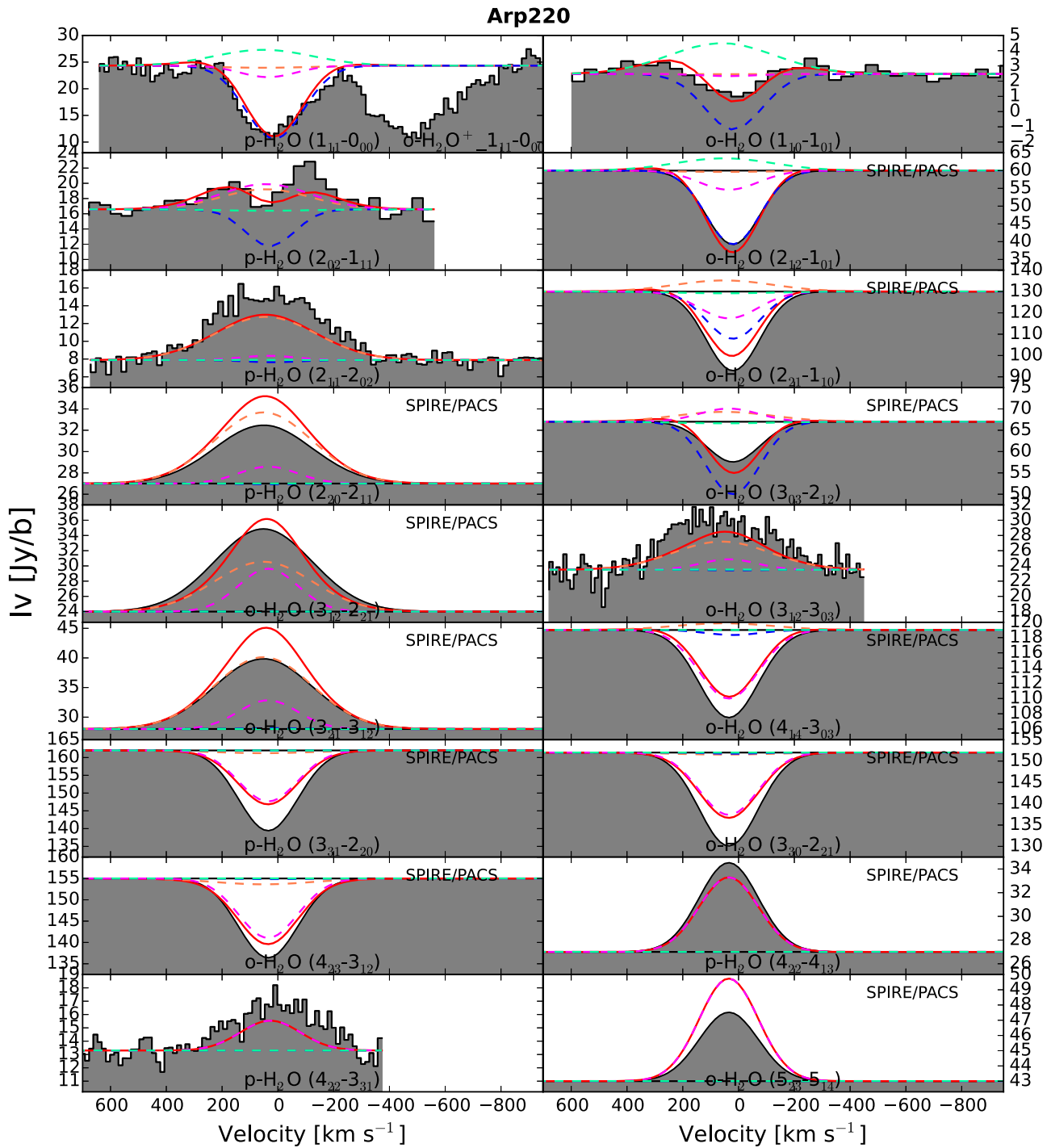


Figure 18. Observed H₂O spectra (gray histograms) and the modeling results (red solid curve) of Arp 220. The blue dashed curves denote the absorption of outflow gas toward the dust continuum of galaxy nuclei. The black solid lines in the subpanels with text “SPIRE/PACS” present the estimated line profiles for SPIRE/PACS-detected lines, whose line shapes are assumed to be the same as the HIFI-detected ground-state absorptions and high-excitation p-H₂O (4₂₂ – 3₃₁) line. For explanation of the other symbols used in the plots, see Figure 11.

CO profiles from a small region toward the galaxies’ center, implying that the absorption may arise from a small strip orthogonal to the molecular disk.

In the case of Arp 220 the ground-state (and low-excitation) absorption feature displays a velocity dispersion that is much narrower than those of the medium-excitation emission lines (FWHM ~ 226 km s⁻¹ compared to FWHM ~ 412 km s⁻¹), but in good agreement with the width of the high-excitation

lines (FWHM ~ 235 km s⁻¹). High spatial resolution ALMA imaging by König et al. (2017) finds that most of the high-excitation H₂O line emission stems from the western nucleus, which is also suspected to harbor a buried AGN (Downes & Eckart 2007). The velocity centroid of the H₂O absorption is consistent with that arising from the western source. It is therefore likely that the low-excitation absorption of Arp 220 arises within the compact western nucleus in a region that could

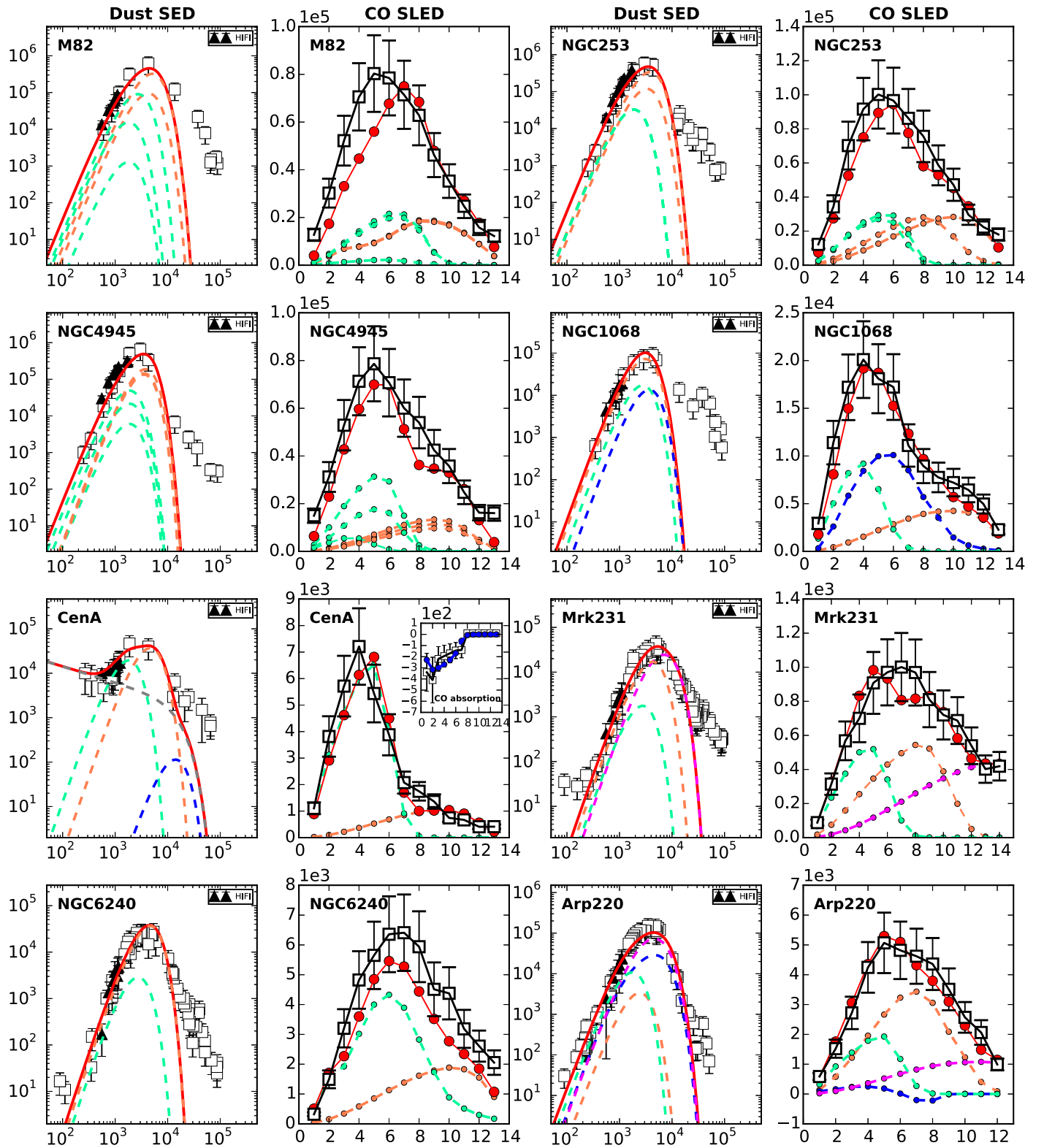


Figure 19. Observed and modeled dust SED (in units of mJy/b) and CO SLED (in units of Jy km s^{-1}) for our sample galaxies. The black squares denote the observed dust continuum or CO emission fluxes, and the black solid triangles denote our HIFI measured dust continuum fluxes. The green, orange, and magenta dashed lines indicate the best-fit model results for cold ERs, warm components, and hot components, respectively, whose velocities are given in Table 4. The red solid lines denote the total modeling results of various components. The blue dashed lines in subplots of NGC 1068, Cen A, and Arp 220 denote the modeling results of outflow gas, absorbing gas (case I), and outflow absorbing gas, respectively. The gray dashed line in the dust SED plot of Cen A indicates the power-law continuum emission of the radio core. The small figure in the CO SLED subplot of Cen A presents the observed (black open squares) and the modeled (blue solid circles) low- J CO absorptions toward the radio core.

be about the same size as the region where high-excitation lines are generated from.

The o-H₂O ground transition profile of Cen A is similar to those of low- J CO lines observed by Israel et al. (2014) showing a broad emission profile arising from the circumnuclear disk (CND) with a narrow absorption close to the systemic velocity against the compact nuclear source. In Cen A, the p-H₂O ground-state line shows an inverse P Cygni profile, which could be a sign of infall (e.g., van der Tak et al. 2016).

Another interesting finding comes from a comparison between the line profiles of o-H₂O and p-H₂O. We find that parts of the o-H₂O and p-H₂O energy ladders are very similar, where the o-H₂O $1_{01}/2_{12}/3_{03}/3_{12}/3_{21}$ levels correspond to the p-H₂O $0_{00}/1_{11}/2_{02}/2_{11}/2_{20}$ levels, respectively (see Figure 1). Therefore, the p-H₂O ground-state ($1_{11}-0_{00}$) transition shows a good correspondence in the line shape to the o-H₂O ($2_{12}-1_{01}$) line rather than the o-H₂O ($1_{10}-1_{01}$) ground-state transition. This is also why the o-H₂O ($3_{21}-3_{12}$) and ($3_{12}-3_{03}$) lines have very similar shapes compared to the p-H₂O ($2_{20}-2_{11}$) and ($2_{11}-2_{02}$) lines, respectively, even though the upper levels of the former are around 100 K higher than those of the latter.

6. Summary and Conclusion

Using HIFI on board *Herschel*, we have obtained for the first time velocity-resolved H₂O spectra for a sample of nearby actively SF galaxies. Our observations include the ground-state transitions of ortho and para H₂O and cover transitions with $E_{\text{up}} \leq 450$ K. The main observational results from our spectroscopic survey are as follows:

1. The H₂O spectra show a diversity of line shapes. The medium-excitation H₂O lines ($130 < E_{\text{up}} \leq 350$ K) are always detected in emission. Their line profiles typically resemble those of CO, indicating that water is widespread in the warm nuclear regions of active galaxies.
2. The line profiles of ground-state and low-excitation H₂O transitions ($E_{\text{up}} \leq 130$ K) often show a mix of emission and absorption. The emission features of these low-excitation lines usually display a wider velocity range than the medium-excitation lines, while the absorption features are often found to show more complex line profiles that differ from galaxy to galaxy.

We analyze the water excitation using the state-of art, 3D non-LTE radiative transfer code “ β 3D.” The main conclusions from the analysis are as follows:

1. Multiple ISM components with different physical conditions are required to explain the observed H₂O line shapes and line intensities. We identify two ISM components that are present in all galaxies—an extended cold ($T_{\text{dust}} \sim 20\text{--}30$ K) region (ER) and a warm ($T_{\text{dust}} \sim 50\text{--}70$ K) component. The cold ER is only excited by collisions and has significant emission-line intensities only in the ground-state and a few low-excitation lines. This gas component is also often responsible for the detected low-excitation absorption features seen in our targets. The warm component contributes almost all the emission of medium-excitation lines. For the two ultraluminous IR galaxies in our sample (Mrk 231 and Arp 220), our models suggest the presence of an even warmer gas component (hot gas) to explain the emission and absorption in the high-excitation H₂O lines ($E_{\text{up}} > 350$ K).

2. The multiple ISM model also allows us to explain the observed dust SED and CO SLED in our target galaxies. The cold ER contributes mainly to millimeter and submillimeter dust continuum. The warm component dominates the total IR luminosity with its dust SED peaking at FIR regimes, suggesting that its generated medium-excitation H₂O lines are excellent probes to study the kinematic of the FIR emitting regions. The middle/high- J ($7 \leq J_{\text{up}} \leq 12$) CO emission lines mainly arise from the warm component, while the low- J CO transitions mainly come from the cold ER. The CO SLEDs of these two components peak at $4 \leq J_{\text{up}} \leq 6$ and $8 \leq J_{\text{up}} \leq 10$, respectively. The hot component, if present, contributes large amounts of IR emission in mid-IR (MIR) regimes (which, however, is usually attenuated by foreground dust) and has a significant effect on the CO SLED at levels with $J_{\text{up}} \geq 10$.
3. IR pumping dominates the excitation of high-excitation energy levels of water (with $250\text{--}350$ K $\leq E/k_{\text{B}} \leq 500\text{--}700$ K in the warm component and $600\text{--}800$ K $\leq E/k_{\text{B}} \leq 1300\text{--}1600$ K in the hot component) and drives their level population toward a Boltzmann distribution close to the dust temperature, while collision dominates the excitation of low-excitation energy levels (with $E/k_{\text{B}} \leq 100\text{--}150$ K, $E/k_{\text{B}} \leq 250\text{--}350$ K, and $E/k_{\text{B}} \leq 600\text{--}800$ K in cold, warm, and hot components, respectively) and drives some low-excitation level population ($E/k_{\text{B}} \leq 150\text{--}200$ K and $E/k_{\text{B}} \leq 400\text{--}600$ K in warm and hot components, respectively) toward a Boltzmann distribution at the kinetic gas temperature. Our observed low-excitation lines (with $E_{\text{up}} < 130$ K) and most of the observed medium-excitation lines (with $130 < E_{\text{up}} < 250\text{--}350$ K) are excited dominantly by collision. IR pumping becomes more and more important in exciting our observed medium-excitation lines with $E_{\text{up}} \geq 200\text{--}300$ K.
4. The gas-phase abundance of H₂O varies from 10^{-9} to 10^{-8} in the cold ER to $10^{-8}\text{--}10^{-7}$ in the warm component to $10^{-6}\text{--}10^{-5}$ in the hot component. Therefore, our results suggest that the water abundance is typically larger in the higher-density and warmer regions.

We thank the anonymous referee for a careful reading of our manuscript and for constructive comments and suggestions, which improved the paper. HIFI has been designed and built by a consortium of institutes and university departments from across Europe, Canada, and the United States under the leadership of SRON Netherlands Institute for Space Research, Groningen, The Netherlands, and with major contributions from Germany, France, and the US. Consortium members are: Canada: CSA, UWaterloo; France: CESR, LAB, LERMA, IRAM; Germany: KOSMA, MPIfR, MPS; Ireland: NUI Maynooth; Italy: ASI, IFSI-INAF, Osservatorio Astrofisico di Arcetri/INAF; Netherlands: SRON, TUD; Poland: CAMK, CBK; Spain: Observatorio Astronómico Nacional (IGN), Centro de Astrobiología (CSIC-INTA); Sweden: Chalmers University of Technology MC2, RSS & GARD, Onsala Space Observatory, Swedish National Space Board, Stockholm University Stockholm Observatory; Switzerland: ETH Zurich, FHNW; USA: Caltech, JPL, NHSC. L.J. and Y.G. acknowledge support by NSF grant nos. 11311130491 and 11420101002 and CAS

Key Research Program of Frontier Sciences B program no. XDB09000000.

Appendix A The Methods of Line Modeling

A.1. Dust SED Model

The dust and gas are assumed to be coexistent in our model, and their mass ratio is set to be the Galactic value of 1:100 (e.g., Draine et al. 2007). Therefore, the frequency-dependent dust emission arising from a single ISM component with uniform physical properties can be calculated with a modified blackbody spectrum:

$$S_\nu = B_\nu(T_d)(1 - e^{-\tau(\nu)})\Omega_s, \quad (1)$$

where B_ν is the Planck function, $\tau(\nu)$ is the total dust optical depth, and Ω_s is the solid angle of the ISM component determined by $\Omega_s = \pi R_s^2/d^2$ (d is the distance of galaxy). The dust optical depth $\tau(\nu)$ was computed by

$$\tau(\nu) = \kappa_d(\nu)N_H\mu_H/100, \quad (2)$$

where N_H is the total proton column density in cm^{-2} , μ_H is the mass of a hydrogen nucleus in g, and $\kappa_d(\nu)$ is the frequency dependence of the dust absorption coefficient in the form of $\kappa_d(\nu) = 0.4(\nu/250 \text{ GHz})^\beta$ in units of $\text{cm}^2 \text{g}^{-1}$ (Priddey & McMahon 2001). The dust emissivity index β is set to 1.5.

The combination of dust SEDs from multiple ISM components depends on their physical distribution relative to each other. If they do not spatially overlap, the total dust SED is simply the sum of the individual dust SEDs from all ISM components. Otherwise, the absorption of dust continuum emission of the background component by the foreground dust needs to be taken into account:

$$S_\nu = B_\nu(T_d)(1 - e^{-\tau(\nu)})\Omega'_s e^{-\tau'(\nu)}, \quad (3)$$

where Ω'_s is the solid angle of the overlapping region and $\tau'(\nu)$ is the dust opacity of the foreground ISM component.

A.2. The β 3D: The Extended Escape Probability Method

The level populations of molecular gas are determined by collisions and radiation through the equations of statistical equilibrium:

$$\begin{aligned} n_u \sum_l (A_{ul} + B_{ul}\langle J_\nu \rangle_{ul} + C_{ul}) \\ = \sum_l n_l (A_{lu} + B_{lu}\langle J_\nu \rangle_{lu} + C_{lu}), \end{aligned} \quad (4)$$

where $l = 45$, which is the total number of levels included, A_{ul} and B_{ul} are Einstein coefficients, and C_{ul} are collisional excitation ($u < l$) and de-excitation ($u > l$) rates. The collision rates of para- and ortho- H_2O with para- and ortho- H_2O (whose OPR in thermal equilibrium is estimated by Equation (1) in Mumma et al. (1987)) have been taken from the LAMDA database (Schoeier et al. 2005), which are originally calculated by Daniel et al. (2011).

The profile-averaged mean radiation intensity, $\langle J_\nu \rangle_{ul}$, is given by

$$\langle J_\nu \rangle_{ul} = (1 - \epsilon_{ul})S_L + (\epsilon_{ul} - \eta_{ul})B(T_d) + \eta_{ul}B(T = 2.7 \text{ K}), \quad (5)$$

where S_L is the source function, $B(T_d)$ is the Planck function at the dust temperature T_d , and $B(T = 2.7 \text{ K})$ is the 2.7 K cosmic microwave background. The method has introduced two profile-averaged photon escape probabilities ϵ_{ul} and η_{ul} . The ϵ_{ul} is the probability that a photon escapes line absorption, and η_{ul} is the probability that a photon escapes dust absorption as well as line absorption and therefore contributes to the observed line emission by a distant observer. The first term on the right-hand side of Equation (5) can be explained as the contribution of line photons, while the second term can be explained as the contribution of dust photons, and the third term as the amount of external radiation reaching the test point.

Under the LVG assumption and our assumption that the excitation of the molecular gas at a given point is only connected with the gas and dust of the same clump, the two escape probabilities ϵ_{ul} and η_{ul} can be simplified into the following forms:

$$\epsilon_{ul} = \frac{\kappa_d}{\kappa_L + \kappa_d} + \frac{\kappa_L}{\kappa_L + \kappa_d} \int \frac{d\Omega}{4\pi} \left[\frac{1 - e^{-(\tau_L + \tau_d)}}{\tau_L + \tau_d} \right], \quad (6)$$

$$\eta_{ul} = \int \frac{d\Omega}{4\pi} \left[\frac{1 - e^{-\tau_L}}{\tau_L} \right] e^{-\tau_d}, \quad (7)$$

where κ_L is the line absorption coefficient, κ_d is the dust absorption coefficient with the form of $\kappa_d(\nu) = 0.4(\nu/250 \text{ GHz})^\beta$ in units of $\text{cm}^2 \text{g}^{-1}$ (Priddey & McMahon 2001), and τ_L and τ_d are the line and dust optical depths, respectively, from the test point to the edge of the clump along a line of sight. The κ_L is calculated by the form of $\kappa_L = [(n_l B_{lu} - n_u B_{ul})h\nu_{ul}/4\pi]\varphi(\nu)$, where $\varphi(\nu)$ is the normalized absorption-line profile contributed by turbulence and thermal speed of gas:

$$\varphi(\nu) = \frac{1}{(\Delta v_D \frac{v_0}{c})\sqrt{\pi}} e^{-(\nu - \nu_0)^2 / (\Delta v_D \frac{v_0}{c})^2}, \quad (8)$$

where ν_0 is the line rest frequency, Δv_D is the Doppler velocity width in the form of $\Delta v_D = \left(v_{\text{turb}}^2 + \frac{2k_B T_k}{\mu} \right)^{1/2}$ (v_{turb} is the turbulence velocity, k_B is the Boltzmann constant, μ is the molecular weight, and T_k is the gas kinetic temperature). The turbulence velocity v_{turb} used to calculate the Doppler velocity width is estimated from molecular cloud line width-size scaling relations where a $3\times$ larger normalization value is adopted (i.e., $\sigma/R^{0.38} = 3.3$), since starburst galaxies are often reported to deviate the local classical molecular cloud scaling relations (Larson's relations; e.g., Swinbank et al. 2011; Kruijssen & Longmore 2013). The grid sizes of clumps ($ngx \times ngy \times ngz$) are fixed to $20 \times 20 \times 20$, but the corresponding physical sizes of grid cell and clump (R) are determined by the column density $N_{\text{clump}}(\text{H})$ of a clump and gas density $n(\text{H})$. In the absence of dust emission and absorption, we obtain the usual expression for the escape probability (e.g., Castor 1970; Hollenbach & McKee 1979). Finally, the critical density is calculated by

$$n_{\text{cr}} = \frac{\sum_{u>l} \epsilon_{ul} A_{ul}}{\sum_{u>l} C_{ul}}. \quad (9)$$

Due to the large Einstein A -coefficients, the critical densities of water lines are usually on the order of 10^8 – 10^9 cm^{-3} under the optically thin case ($\epsilon_{\text{ul}} \simeq 1$) (Poelman et al. 2007).

Note that the angle dependence in the above equations is replaced by the summation over a fixed number of directions in our model, i.e., $\int \frac{d\Omega}{4\pi} = \sum_{\kappa=1}^N$. The number of directions is arbitrary, but a six-ray approximation is implemented, i.e., $N = 6$, to represent the six different orthogonal directions in a 3D Cartesian grid. The line and dust optical depths (τ_L and τ_d) are calculated from the test point up to the edge of the clump cube in each of six directions. Hence, the probability for a photon to escape is connected through all the grid points along six directions. Equations (4)–(7) constitute the core of our method to calculate level populations including dust radiation.

A.3. The Ray-tracing Approach

The ISM component, which is an ensemble of uniform clumps in a rectangular box, forms the basic unit in our ray tracing. We perform the ray tracing in a 3D Cartesian grid, with the z -axis along the line of sight. For each pixel (x, y) in the projected surface (i.e., xy -plane at $z = 0$), we calculate the line and dust continuum fluxes emerging from this pixel at different frequency channels by

$$I(x, y) = \sum_{z'=1}^Z \Lambda(x, y, z') \times \exp \left[- \sum_{i=1}^{z'-1} (\tau_L(x, y, i) + \tau_d(x, y, i)) \right], \quad (10)$$

$$\Lambda(x, y, z') = \left[\frac{\kappa_L}{\kappa_L + \kappa_d} S_L(x, y, z') + \frac{\kappa_d}{\kappa_L + \kappa_d} \times B(T_d(x, y, z')) \right] (1 - e^{-(\tau_L(x, y, z') + \tau_d(x, y, z'))}), \quad (11)$$

where z' labels all the grid cells in backward order along the ray, and i indicates grid cells located in front of the z' th grid cell in backward order. The $\tau_L(x, y, z')$ and $\tau_d(x, y, z')$ indicate integrated line and dust optical depth of a single grid cell at (x, y, z') , respectively. And Z is the total number of grid cells along the z -direction, which is determined by the clump size ($ngz = 20$) and number of clumps along the line of sight (i.e., $Z = N(H)/N_{\text{clump}}(H) \times ngz$). A simple physical interpretation of Equations (10)–(11) is that $\Lambda(x, y, z')$ equals the amount of photons generated by molecule gas and dust at the grid cell (x, y, z') , and $\exp[-\sum_{i=1}^{z'-1} (\tau_L(x, y, i) + \tau_d(x, y, i))]$ is the probability that a photon at the grid cell (x, y, z') escapes both dust and line absorption along the z -direction.

We attribute the clumps inside an ISM component to a random normal distributed global velocity field following the parameters derived by Gaussian decomposition of H_2O spectra. The final output of our ray-tracing approach is a 3D line data cube, with the first two dimensions along the spatial xy -plane and the third dimension along the frequency (or velocity). We then integrate the line cube along the xy -plane to derive a single global spectrum. In our ray-tracing approach, the surface size (i.e., the area along the xy -plane) of an ISM component is not important, since the modeled line intensity per unit area and the global line shape will not change with surface size as long as the given global velocity field can be fully sampled. We

determine the physical size (R_s) of an ISM component by scaling the modeled line intensity per unit area to the observed value.

The spectra from multiple ISM components are simply the sum of individual ISM components if they do not spatially overlap. Otherwise, we need to integrate emissions through all the gas and dust of different ISM components (i.e., $Z = \sum_{j=1}^n Z_j$ in Equation (10), n is the total number of overlapped ISM components), to consider the line and dust absorption of the front ISM component against the background ISM component.

A.4. Select Best Models

In summary, our galaxy (nucleus) model is a combination of multiple ISM components. An ISM component is constrained by six parameters: $N_{\text{clump}}(H)$, $n(H)$, T_k , T_d , $X_{\text{H}_2\text{O}}$, and $N(H)$. The first five parameters constrain the excitation condition of the molecule (H_2O and CO). The last parameter $N(H)$, together with the parameters (line centers and line widths) derived from Gaussian decomposition of our H_2O spectra, further determines the integrated line intensity and global line shape.

We model each velocity component of the H_2O spectra separately. For each velocity component, we derive the first and second ISM components by fitting the medium-excitation and ground-state/low-excitation emission lines, respectively. Additional ISM components are then added to fit the ground-state/low-excitation absorption lines and/or high-excitation lines where necessary. We first remove the underlying continuum and fit only the H_2O line intensities (negative integrated areas are fitted in the cases of absorption lines). The best-fit parameters for an ISM component are searched by minimizing the sum of chi-squared residuals. We then do a second pass to discriminate the models that significantly overestimate ($\geq 120\%$) the observed total continuum fluxes and CO ($J_{\text{up}} = 1$ – 13) fluxes.

We utilize the ISM component dominating FIR luminosity (normally the warm component derived by fitting medium-excitation lines) as the background continuum source of the ground-state/low-excitation absorptions. For each derived possible model of the background warm component (or the background hot component in the case of Arp 220), we search for the best-fit models of the absorption component by allowing its physical size to vary from zero to the maximum coverage. It is worth mentioning that some models of the warm component (or hot component in the case of Arp 220) fail to produce satisfactory absorptions that match the observations, and thereby we have discriminated these models.

Since our models of individual ISM components are derived by fitting only certain H_2O transitions, they may significantly overestimate or underestimate line intensities of the other transitions. Therefore, we add up the modeled H_2O spectra from all the sets of ISM components at different velocities and do a third pass by discriminating the combined models whose predicted global H_2O spectra show large discrepancies with the observations. The combined models with predicted global dust continuum or CO line intensities exceeding 120% of the observed values were also excluded. The derived final parameters of our models are given in Table 4.

Appendix B Detailed Models for Individual Galaxies

B.1. M82

M82 is a nearby, almost edge-on galaxy ($i \simeq 77^\circ$), notable for its spectacular bipolar outflow (e.g., Kamenetzky et al. 2012). High-resolution CO maps of the central ~ 1 kpc disk indicate that the molecular gas is largely concentrated in three areas: a northeast lobe, a southwest lobe, and, to a lesser extent, a central region (Weiß et al. 2001, 2010; Walter et al. 2002). Overall, M82 shows weaker H₂O line emission relative to CO. For example, the CO($J = 3 - 2$)/H₂O($2_{11} - 2_{02}$) ratio in M82 is much larger ($\simeq 40$) compared to that of NGC 4945 ($\simeq 5.5$) and NGC 253 ($\simeq 5.6$). Our models suggest that the faintness of H₂O in M82 is mainly due to the lower H₂O abundance (see Table 4). The blueshifted and redshifted H₂O emissions are associated with the southwestern ($\delta v = -73$ km s⁻¹) and northeastern ($\delta v = 86$ km s⁻¹) molecular lobes, respectively. Our model for M82 requires a warm and a more extended cold component to match the observed H₂O line intensities, where the warm gas dominates the medium-excitation H₂O lines, dust FIR continuum, and high- J ($J \geq 8$) CO lines, while the cold gas mainly contributes to the low-excitation H₂O, the long-wavelength submillimeter dust continuum, and low/middle- J ($J \leq 8$) CO emission lines. The blueshifted emission from the southwestern lobe is stronger than the redshifted emission from the northeastern lobe (see Figure 11). In our model these differences arise from the slightly elevated dust temperature in the southwestern lobe compared to the northeastern lobe ($T_{\text{dust}} \simeq 50\text{--}70$ K vs. $\simeq 40\text{--}50$ K). The absorption seen in ground-state lines occurs close to the systemic velocity ($\delta v = 26$ km s⁻¹) and does not have any correspondence to the emission features seen in medium-excitation H₂O lines. This implies that the absorptions arise from a different region than the warm component, possibly from the front cold gas. As the absorption in M82 is observed to be much narrower and shallower than those in NGC 4945 and NGC 253, our model suggests that the cold gas in M82 covers only a small fraction of the continuum ($F_{\text{cc}} \leq 0.25$). In a more detailed study of the H₂O absorption in M82, Weiß et al. (2010) compared the absorption profile with high spatial resolution ($3''.5$) CO observations. They find that the CO line profile is in very good agreement with the water absorption profile within only a small region at the galaxy center, which is associated with a strip orthogonal to the molecular disk of M82.

B.2. NGC 253

NGC 253 is a nearby barred spiral galaxy with a compact nuclear starburst and a weak AGN in its center (Müller-Sánchez et al. 2010; Aalto et al. 2011). The nuclear starburst drives a ~ 100 pc scale molecular gas outflow/wind detected in CO (Mitsuishi et al. 2013; Bolatto et al. 2013). As in the case of M82, our model reveals that the medium-excitation H₂O emission lines and most of the dust continuum arise from a warm ($T_{\text{dust}} \simeq 50$ K), dense ($n(\text{H}) \sim 10^5\text{--}10^6$ cm⁻³), and compact ($R_s \simeq 50\text{--}60$ pc) region that is very likely associated with the inner nuclear starburst disk. The line profile of this warm gas component displays a double Gaussian and follows qualitatively the shape of the CO(3–2) line profile (see Figure 2). It is, however, significantly narrower than the CO(3–2) emission profile and lacks emission at the terminal velocity of the CO spectrum. In contrast, both ground

transitions of o-H₂O and p-H₂O show emission significantly redward ($\delta v \approx 60$ km s⁻¹) of the medium-excitation lines, in good agreement with the shape of the red wing of the CO line profile. This demonstrates convincingly that the ground-state lines originate from a different physical volume than the medium-excitation lines, and it is tempting to speculate that the H₂O ground transitions are at least partly associated with the outflowing molecular material in NGC 253. This interpretation is also supported by the blueshifted ($\delta v = -60$ km s⁻¹) absorption seen in the p-H₂O ground transition, which forms, together with the redshifted emission, a P Cygni profile. We have modeled the blue and red line wings of the outflow using similar physical parameters resembling those found for the cold gas in NGC 4945. The two outflows generate almost equal emissions in ground-state o-H₂O ($1_{10} - 1_{01}$) lines (green dashed curves in Figure 12). The reason for asymmetrical line shapes found in low-excitation lines of NGC 253 is simply due to their different spatial geometry with respect to the nuclear disk. That is, the redshifted outflow is located behind the nuclear disk, while the blueshifted outflow resides in front of, and almost completely covers ($F_{\text{cc}} \simeq 1$), the nuclear disk (see Figure 20), in agreement with the high spatial resolution CO maps from Bolatto et al. (2013). Therefore, the part of the blueshifted outflow located right in front of the nuclear disk produces ground-state and low-excitation absorption lines, while the rest produces ground-state line emission. The absorption in o-H₂O ($1_{10} - 1_{01}$) and o-H₂O ($3_{03} - 2_{12}$) lines happens to compensate for the blueshifted line emission, making these two lines partly invisible.

B.3. NGC 4945

NGC 4945 is a nearby, almost edge-on, disk galaxy. The central region of this galaxy contains an inclined nuclear starburst disk (Moorwood et al. 1996; Marconi et al. 2000; Chou et al. 2007) and a heavily enshrouded AGN (Iwasawa et al. 1993; Guainazzi et al. 2000; Pérez-Beaupuits et al. 2011). The central region is obscured by a strongly absorbing rotating circumnuclear SF ring seen nearly edge-on (Marconi et al. 2000; Spoon et al. 2003; Chou et al. 2007). Our modeling of NGC 4945 suggests that the strong emission seen in medium-excitation lines comes from a dense ($n(\text{H}) \sim 10^6$ cm⁻³), warm ($T_{\text{dust}} \sim 50\text{--}60$ K) region with a size of $R_s \sim 50\text{--}70$ pc (this total size is the sum of the sizes of three warm components at different velocities given by Table 4). The warm component is most likely associated with the nuclear starburst disk, whose size has been determined to be ~ 100 pc from high-resolution HST-NICMOS observations of the Pa α line (Marconi et al. 2000) and CO interferometric maps (Chou et al. 2007). Since the warm nuclear disk material does not produce enough line emission in the low-excitation transitions, we added another ISM component to match these low-excitation emissions. We find that the corresponding emission component is relatively cold ($T_{\text{dust}} \sim 20$ K), less dense ($n(\text{H}) \sim 10^5$ cm⁻³), and much more extended ($R_s \sim 200\text{--}300$ pc). By fitting the absorption features seen in ground-state/low-excitation lines, we obtain an absorption component with similar physical properties to the cold emission component, except for its much smaller size ($R_s \sim 50\text{--}70$ pc). Thus, we speculate that the cold emission and absorption components arise from the same physical region, which is very likely to be the surrounding molecular ring. In this picture, the ground-state emission seen at $\delta v = 141$ km s⁻¹ and $\delta v = -112$ km s⁻¹ arises from the edges

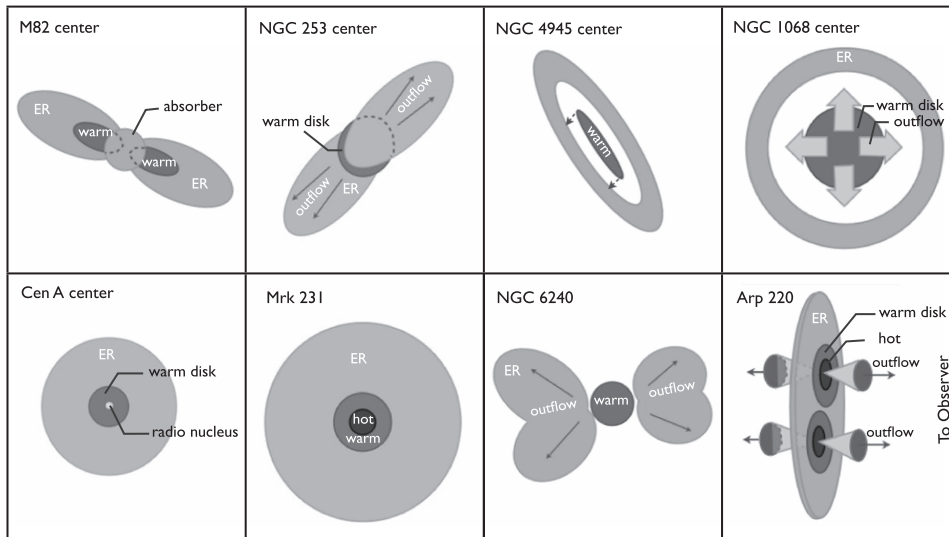


Figure 20. Schematic representation of our modeled sources, showing possible geometries for our sample galaxies. The detailed descriptions of each modeled source are given in the text.

of the molecular ring, whose sightlines do not intercept with the warm nuclear gas and are therefore free of absorption. The absorption feature at $\delta v = 48 \text{ km s}^{-1}$ arises from the cold gas of the molecular ring, which is located right in front of the warm nuclear disk. The warm nuclear disk is almost entirely covered by the cold gas of the molecular ring (i.e., $F_{cc} \simeq 1$), given by the deep-to-bottom absorption seen at the velocity center. The terminal velocities in the low-excitation and medium-excitation spectra are almost identical (see Figure 13), implying that the nucleus disk spans approximately the same range of velocities as the surrounding molecular ring. This interpretation is consistent with high spatial resolution CO maps, which show that the rotation curve flattens beyond the radius of the nucleus disk ($R \sim 100 \text{ pc}$; Chou et al. 2007). Note that the source size of the cold molecular ring (ER) given in Table 4 denotes the projected area at the two sides of the molecular ring rather than the real radius of the ring structure. The gas kinetic temperatures are found to be close to the dust temperatures within both the nucleus disk and the molecular ring.

B.4. NGC 1068

NGC 1068 is a nearby and bright Seyfert galaxy seen at an inclination angle of $i \leq 40^\circ$. Molecular gas (CO and HCN) observations toward its center have shown a central CND with a radius around 100–150 pc (e.g., Krips et al. 2011; Spinoglio et al. 2012) and an SF ring/spiral at a radius of 1.0–1.5 kpc (Tacconi et al. 1994; Schinnerer et al. 2000). As the brightest prototype Seyfert-2 AGN, NGC 1068 exhibits pronounced radio jets extending out to several kiloparsecs from the center (Gallimore et al. 2004; Krips et al. 2006). Following the above modeling approach, we utilized a warm component plus a cold component to match the medium-excitation and low-excitation H_2O emission lines, respectively. According to the derived physical parameters, the warm component is very likely associated with the CND, while the cold component should be at least partly related to the SF ring/spiral. In contrast to higher-inclination galaxies in our sample, the low-excitation H_2O lines in NGC 1068 do not show absorption, indicating that no cold gas is located in front of the warm CND. The models of the above two components are able to fit most of H_2O lines

very well, but fail to explain a large part of the $\text{o-H}_2\text{O}$ ($2_{12} - 1_{01}$) and middle- J CO ($4 \leq J_{\text{up}} \leq 8$) line intensities, which are very luminous in NGC 1068. Therefore, we added another component to match the remaining intensities of these lines. We find that this additional component contains a substantial amount of relatively low density ($\sim 10^4 \text{ cm}^{-3}$), low opacity ($N_{\text{H}} \sim 1 \times 10^{23} \text{ cm}^{-2}$), but very hot gas ($T_{\text{k}} \sim 120\text{--}180 \text{ K}$) within a radius of $\sim 150\text{--}200 \text{ pc}$. Therefore, we speculate that this gas is probably associated with the part of molecular gas in the CND that is shock heated to high kinetic temperatures as a consequence of an interaction between the radio jet and the CND (Krips et al. 2011). The strong interaction between the radio jet and the CND has been indicated by many recent observations: the CO and HCN line observations display a complex kinematic behavior of the gas (e.g., Krips et al. 2011), MIR observations reveal hot and ionized gas following the orientation of the radio jet (e.g., Poncelet et al. 2008; Müller Sánchez et al. 2009), and X-ray observations show that clouds in many locations are strongly affected by shock heating (e.g., Wang et al. 2012). The strong collisional excitation of the shocked gas leads to enhanced emission of the $\text{o-H}_2\text{O}$ ($2_{12} - 1_{01}$) line and line ratios of CO middle- J to $1 - 0$ (e.g., CO ($3 - 2$)/($1 - 0$); Wang et al. 2014) in NGC 1068. With this supplemented component of hot shocked gas, we are able to fit all the observed H_2O lines, dust SED, and CO SLED very well.

B.5. Centaurus A, NGC 5128

Cen A is the closest giant elliptical and a powerful radio galaxy (for a review, see Israel 1998). Cen A exhibits a powerful and variable radio nucleus (Meisenheimer et al. 2007; Israel et al. 2008). Observations of molecular gas toward its central region ($\leq 3 \text{ kpc}$) have revealed several different prominent components: a nuclear disk ($\sim 30 \text{ pc}$) containing ionized and molecular gas, a compact CND (within the inner 400 pc), and an even larger extended thin molecular disk (Espada et al. 2009; Espada 2013; Israel et al. 2014; Salomé et al. 2016). According to our model, the ground-state emissions arise from a cold ($T \sim 20 \text{ K}$), extended ($R_s \sim 70\text{--}100 \text{ pc}$) region, which is likely related to dense gas in the CND or the outer molecular disk. Although we

have only detected one line above ground states, we are still able to roughly constrain physical parameters of the warm component in Cen A by utilizing the upper limits of those undetected H₂O lines, together with additional information from the dust SED and CO SLED. The warm component in Cen A is found to be very compact ($R_s \sim 7\text{--}15$ pc), implying that only a small fraction of the gas is excited to high levels.

In order to model the absorption features seen in ground-state lines, we first adopted the dust continuum of the warm component as the background. With this assumption we derived a cold ($T_{\text{dust}} \simeq 20$ K) absorbing gas component with extremely high optical depth ($N_{\text{H}} \geq 6 \times 10^{25} \text{ cm}^{-2}$), which we consider as unrealistic, as it would result in a dust SED inconsistent with the observation. We noticed that the o-H₂O ($1_{10} - 1_{01}$) line in Cen A has an almost comparable (or even a slightly higher) absorption depth compared with the p-H₂O ($1_{11} - 0_{00}$) line, which is very unusual as the ratios of their absorption intensities are much smaller (10%–25%) in all other cases. Considering these matters, the background source should be more likely the radio core rather than warm dust. Recent works found that at the lowest frequencies (≤ 500 GHz) observed with SPIRE and HIFI, the continuum flux of Cen A is still completely dominated by the radio core (Israel et al. 2014, and Figure 19). We adopted an index of -0.36 ($F_\nu \propto \nu^{-0.36}$; Meisenheimer et al. 2007) and a normalization value of $F_{461 \text{ GHz}} = 8.2$ Jy (Israel et al. 2014) to model the radio power-law spectrum. As the radio core is unresolved even at very high spatial resolution ($\sim 0''.1$ or ~ 1.8 pc; Israel 1998; Espada et al. 2009), we adopt different values from 0.01 to 10 pc for its physical size (R_{core}). Our models suggest that the absorptions arise from either less dense ($\sim 10^3 \text{ cm}^{-3}$) but high kinetic temperature ($T_k \sim 120\text{--}180$ K) gas or relatively denser ($\sim 10^4 \text{ cm}^{-3}$) but cold ($T \sim 20\text{--}30$ K) gas. The former may be associated with shocked gas around the base of the radio jet (Ott et al. 2013), while the latter could be related to cold dense gas in the CND or the outer molecular gas disk. Our model can also explain the absorptions detected in low- J CO lines (see the top subplot in the panel of Cen A of Figure 19, where the observed CO data points are from Israel et al. 2014). We obtain the same model results for $R_{\text{core}} \leq 1$ pc; however, no satisfactory solutions can be found anymore if the radio core becomes larger than a few parsecs.

B.6. Mrk 231

Mrk 231 is the most luminous infrared galaxy in the local universe, with $L_{\text{TIR}} \simeq 3.2 \times 10^{12} L_\odot$ (Sanders et al. 2003). Multiwavelength observations reveal a QSO-like nucleus (e.g., Soifer et al. 2000; Gallagher et al. 2002) and a compact starburst disk (e.g., Carilli et al. 1998; Tacconi et al. 2002), embedded in a more extended (~ 1 kpc scale) diffuse disk (Taylor et al. 1999). Our favored model for Mrk 231 consists of a cold ($T_{\text{dust}} \sim 30$ K), extended ($R_s \simeq 1000\text{--}1500$ pc) diffuse halo, a warm ($T_{\text{dust}} \sim 50\text{--}60$ K) starburst disk of radius $\sim 300\text{--}550$ pc, and a highly obscured, compact ($R_s \sim 60\text{--}70$ pc), hot ($T_{\text{dust}} \sim 160\text{--}180$ K), dense ($n(\text{H}) \simeq 10^6 \text{ cm}^{-3}$) component. Our derived sizes are in good agreement with interferometric imaging of CO(1–0) and (2–1) lines, which shows a starburst disk with $R_s \simeq 500$ pc (Downes & Solomon 1998) embedding in a \sim kiloparsec extended diffuse disk (Taylor et al. 1999). Unlike normal LIRGs of our sample, Mrk 231 shows intense high-excitation H₂O features (with $E_{\text{up}} \sim 600\text{--}700$ K) in both emission and absorption, which cannot be explained by the warm component. Our model reveals that these high-excitation lines emerge from a very compact component with extremely

high dust temperature and gas density, which is most likely related to the AGN-dominated region. The contributions of the hot component to H₂O line intensities are denoted by magenta dashed curves in Figure 16.

The observed and modeled dust SED and CO SLED of Mrk 231 are presented in Figure 19. As one can see from the figure, the bulk of far-IR continuum arises from the warm disk (with $\tau_{100\mu\text{m}} \sim 0.5\text{--}1.0$), while large amounts of mid-IR continuum fluxes arise from the hot component (with $\tau_{100\mu\text{m}} \sim 1.0\text{--}1.5$ and $\tau_{25\mu\text{m}} \sim 8\text{--}10$). The hot component of Mrk 231 accounts for $\sim 25\%$ of the total infrared luminosity, but contains only 0.04% of the total dust mass. Note that the hot component should be deeply buried in the warm starburst disk and halo. Otherwise, it will severely overshine dust SED in the mid-IR wavelength regime. In our model, the mid-IR infrared emission from the hot component is attenuated by foreground dust with $\tau_{25\mu\text{m}} \simeq 1.2\text{--}2.5$. The CO SLED of Mrk 231 displays an approximately flat distribution over rotational ladders above $J_{\text{up}} = 10$, due to the strong high- J CO emissions from the hot component. Finally, our model for Mrk 231 is broadly consistent with the model derived by González-Alfonso et al. (2010).

B.7. The Antennae Galaxies—NGC 4038/NGC 4039

The Antennae is an early-stage merger between two gas-rich spiral galaxies, NGC 4038 and NGC 4039 (Schirm et al. 2014). Its majority of molecular gas and star formation is occurring within two nuclei and the overlap region (e.g., Gao et al. 2001; Schirm et al. 2014, 2016). Our HIFI single-pointing observations were positioned at the overlap region, which is the strongest continuum source of the Antennae. We do not have any detections within this region, which we suspect is due to its low mass of dense gas. If assuming that the overlap region has a warm component that is similar to those found in other galaxies, we estimate its physical size to be around $R_s = 40\text{--}50$ pc and dense gas mass around a few times $10^8 M_\odot$. The dust SED fitting predicts that its dust temperature is around $\sim 40\text{--}50$ K and dust mass around $\sim 2 \times 10^6 M_\odot$. Our derived low mass of warm dense gas is consistent with recent studies based on SPIRE/FTS CO observations using a non-LTE analysis (Schirm et al. 2014) and high angular resolution observations of dense molecular gas (HCN and HNC) with ALMA (Schirm et al. 2016), which showed that the fraction of molecular gas in the dense and warm phase in the Antennae is only around 0.2%–0.3%.

B.8. NGC 6240

NGC 6240 is an early-stage merger hosting two nuclei that are separated by $\sim 1''.5$ (Beswick et al. 2001). CO observations reveal that most of the molecular gas in NGC 6240 is located in the overlap region of the two nuclei (e.g., Iono et al. 2007; Engel et al. 2010; Feruglio et al. 2013a, 2013b). We utilized a warm component to model medium-excitation H₂O emissions (which are likely associated with the gas concentration between the two nuclei) and an extended low-excitation component (i.e., ER) to account for ground-state H₂O emissions. The latter are likely associated with the large-scale (\sim kiloparsec) gas distribution detected in CO (Downes & Solomon 1998). While the warm gas component in NGC 6240 shows similar physical properties to those derived for other galaxies, the low-excitation gas is inconsistent with the parameters found in other systems but exhibits a much higher kinetic temperature ($T_k \simeq 120\text{--}400$ K; see Table 4). This high kinetic temperature is required to match the

exceptionally high line-to-continuum ratios ($L'_{\text{line}}/L_{\text{IR}}$) found in ground-state H_2O and low- J CO ($J \leq 7$) lines. The line-to-continuum ratio ($L'_{\text{H}_2\text{O}}/L_{\text{IR}}$) of ground-state H_2O transitions for NGC 6240 is around 3×10^{-4} , which is significantly higher than the value found, e.g., for Mrk 231 ($L'_{\text{H}_2\text{O}}/L_{\text{IR}} \simeq 7 \times 10^{-5}$). The high line-to-continuum ratios of CO lines have been investigated in several recent publications and have been attributed to galaxy-wide shocks owing to the advance merger state of NGC 6240 (e.g., Meijerink et al. 2013; Papadopoulos et al. 2014). This picture also explains the strong $\text{H}_2(1-0)$ S(1) emission at $2.12 \mu\text{m}$ (Goldader et al. 1995), the spectacular butterfly-shaped emission-line nebula seen in *HST* $\text{H}\alpha$ images (Gerssen et al. 2004) and *Chandra* X-ray images (Feruglio et al. 2013b), and the massive molecular outflow detected by the high-resolution interferometry CO maps (Feruglio et al. 2013a) and HCN/CS maps (Scoville et al. 2015). Our model with high kinetic temperatures but normal dust temperatures gives further support to this picture.

Note that we use the integrated fluxes from *Herschel*/SPIRE for p- H_2O ($1_{11} - 0_{00}$) and o- H_2O ($3_{21} - 3_{12}$) lines since they are not detected by our HIFI observations. *Herschel*/PACS observations show that high-excitation H_2O lines of NGC 6240 are much weaker than those of Mrk 231 or Arp 220. This suggests that a significant hot component, similar to the one in Mrk 231 or Arp 220, may not exist in NGC 6240. This is in agreement with our dust SED fitting, which suggests that the size of such a hot component, if it exists, cannot be larger than ~ 20 pc.

B.9. Arp 220

Arp 220 is the nearest ultraluminous infrared galaxy. It is a late-stage merger with two counterrotating disks separated by roughly $\simeq 1''$ (or $\simeq 400$ pc), orbiting within an extended kiloparsec-scale molecular gas disk (e.g., Scoville et al. 1997; Downes & Solomon 1998). A highly dust-obscured AGN in the western nucleus of Arp 220 is suggested by mounting evidence (e.g., Downes & Eckart 2007). A large reservoir of molecular gas has been observed to be concentrated in both nuclear disks (FWHM $\simeq 200$ – 250 pc from CO(6–5) map; Scoville et al. 1997; Rangwala et al. 2015; Tunnard et al. 2015). High-resolution ALMA imaging of dense gas (CO (6–5), HCN, CS) has shown that the two nuclei have almost the same line centroids and velocity dispersions (with velocity offset only being $\Delta V \sim 20$ – 100 km s^{-1} ; Scoville et al. 2015; Rangwala et al. 2015). Thus, we cannot kinematically separate the two nuclei in our H_2O spectra, and thereby we model the two nuclei together as a single region. The predicted size and line intensities of each nucleus, therefore, are half of our modeled values, if they are assumed to be equal. We note that recent high spatial resolution observations of H_2O with ALMA, however, showed that 2/3 of the high-excitation water emission is emitted by the western nucleus (König et al. 2017). It is worth noting that strong self-absorption has been detected at the centers of both nuclei, where CO $J = 6 - 5$, HCN, and CS lines show double-peaked velocity profiles in both nuclei (Rangwala et al. 2015; Scoville et al. 2015; Wang et al. 2016). So it is possible that the double-peaked line shapes seen in our H_2O spectra are also due to self-absorption. We thereby utilized a broad Gaussian emission plus a narrow absorption to fit the double-peaked H_2O lines.

We first model the medium-excitation and high-excitation H_2O lines of Arp 220. We found that the medium-excitation lines come

from a warm ($T_{\text{dust}} \sim 40$ K) region ($N_{\text{H}} \sim 5 \times 10^{24} \text{ cm}^{-2}$, $R_s \sim 120$ – 150 pc), which is very likely to be associated with the outer starburst regions of two nuclear disks. The high-excitation lines arise from a very compact ($R_s \sim 70$ – 100 pc), hot ($T_{\text{dust}} \sim 100$ – 180 K) region whose column density is extremely high ($N_{\text{H}} \sim 1 \times 10^{25} \text{ cm}^{-2}$). The hot component is very likely associated with the compact AGN- or starburst-dominated region at the nuclear center. To match the absorptions seen in ground-state and low-excitation lines, we add a third component in front of the hot component. The gas absorber is located in front of the hot component rather than the warm component because it is the hot component that dominates dust continuum emission and displays a velocity dispersion ($235 \pm 18 \text{ km s}^{-1}$) comparable to the line width of the absorptions ($226 \pm 18 \text{ km s}^{-1}$). Our model reveals that the ground-state/low-excitation absorptions arise from an ISM component with warm dust temperature ($T_{\text{dust}} \sim 60$ – 80 K), high gas temperature ($T_{\text{k}} \sim 100$ – 200 K), and large column density ($N_{\text{H}} \sim 5 \times 10^{25} \text{ cm}^{-2}$), whose line intensities are denoted by blue dashed curves in Figure 18. The absorption component is not likely to arise from the part of the warm disk, given by its very distinct physical properties. Considering its high gas temperature, the absorption component is very likely to associate with massive outflows driving from the nuclei. The molecular outflows have been suggested by many molecular gas (like OH^+ , H_2O^+ , and HCO^+) observations, which show P Cygni absorption line profiles in both nuclei (Sakamoto et al. 2009; Tunnard et al. 2015). The last component required to account for the broad ground-state H_2O emissions of Arp 220 is a kiloparsec-size ($R_s \sim 1000$ – 1200 pc) molecular disk with large amounts of cold ($T_{\text{dust}} \sim 20$ K), less dense ($\sim 10^4 \text{ cm}^{-3}$) gas.

Our model for Arp 220 is also capable of explaining the observed dust SED and CO SLED (see Figure 19). The massive kiloparsec-size molecular disk, in which the two nuclei are embedded, contributes most of the submillimeter continuum flux and low- J ($J \leq 3$) CO emissions (green lines). The warm component (i.e., the outer starburst regions of two nuclei) barely contributes to the total dust continuum, but it produces the major part of dense gas emissions such as medium-excitation H_2O and CO $5 \leq J_{\text{up}} \leq 9$ lines (orange lines). The hot component and its massive molecular outflow dominate dust SED in the FIR/MIR regime, whose size ($D \sim 140$ – 200 pc) matches the observed dust continuum size (FWHM $\simeq 140$ – 220 pc) well. We therefore predict that dust continuum comes from a more compact region than dense gas emission, which has been confirmed by several observations (e.g., Rangwala et al. 2015). Our model also suggests strong self-absorptions in CO $5 \leq J_{\text{up}} \leq 8$ lines by the molecular outflow (blue points in Figure 19). As the absorption intensities (blue points) are comparable to (or even larger than) CO emissions from the hot component (magenta points), CO $5 \leq J_{\text{up}} \leq 8$ lines should be close to (or even go below) the zero continuum level, at the center region in which the hot component and its molecular outflow reside. This picture corresponds well with high-resolution ALMA CO (6–5) observation, which displays a double-peaked line profile at the centers of both nuclei but shows blue/red line peaks farther outside (Rangwala et al. 2015). The high- J ($J_{\text{up}} \geq 11$) CO lines, however, arise mainly from the hot component, and they shine through molecular outflows without absorptions. A schematic representation of our model for Arp 220 is given in Figure 20. Finally, we compare our model of Arp 220 with that in

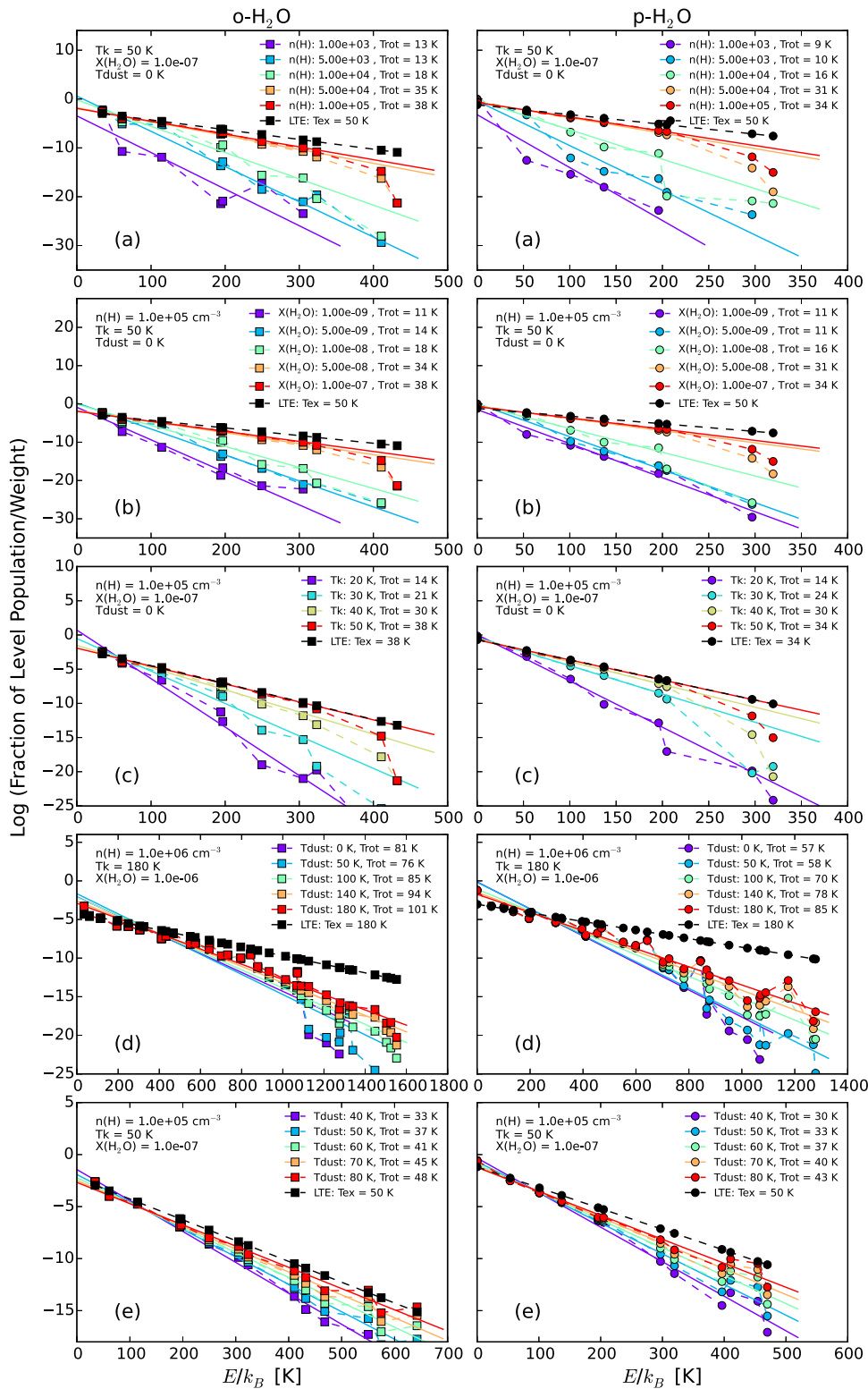


Figure 21. Level populations of water under different physical conditions. The values for gas density ($n(\text{H})$), gas temperature (T_K), water abundance ($X(\text{H}_2\text{O})$), and dust temperature (T_{dust}) are given in the plots. For explanation of the symbols used in the figure, see Figure 6.

González-Alfonso et al. (2004, 2012). Overall, our model predicts a roughly similar hot component, but results in a denser, more compact and opaque warm component. Our model also requires a molecular outflow rather than an extended halo (González-Alfonso et al. 2004, 2012) to match the absorptions seen in low-excitation lines.

Appendix C

Water Excitation under Different Physical Conditions

We present the level populations of water under different physical conditions in Figure 21. Panels (a) and (b) in Figure 21 show that water gas is subthermally excited when gas density is not exceeding $1 \times 10^4 \text{ cm}^{-3}$ and water

abundance is smaller than 1×10^{-8} . Panel (c) shows that the excitation temperature of water increases with increasing kinetic temperatures since the low/moderate-excited levels are mainly collisionally excited under the physical conditions of $n(\text{H}) \simeq 1 \times 10^5 \text{ cm}^{-3}$ and $X(\text{H}_2\text{O}) \simeq 1 \times 10^{-7}$. Once the gas density, kinetic temperature, and water abundance increase to extremely large values ($n(\text{H}) \geq 10^6 \text{ cm}^{-3}$, $T_k \geq 100 \text{ K}$, and $X(\text{H}_2\text{O}) \geq 10^{-6}$), as in the case of the hot component found in ULIRGs, the water level population can be thermally excited up to $E/k_B \simeq 500\text{--}800 \text{ K}$, as shown in panel (d). When the dust temperature is larger than the kinetic temperature, the thermalized levels start to be overpopulated by IR pumping, i.e., IR pumping starts to play a role in exciting the thermalized lines. For example, the level populations of o-H₂O with $E_{\text{up}} \sim 200\text{--}300 \text{ K}$ (and $E_{\text{up}} \sim 100\text{--}200 \text{ K}$ for p-H₂O) in the warm component will not vary with the dust temperature if $T_{\text{dust}} \leq T_k$ (see Figure 5). However, once $T_{\text{dust}} > T_k$, more and more water will be populated within these levels with increasing dust temperature (see panel (e) in Figure 21).

ORCID iDs

K. M. Menten  <https://orcid.org/0000-0001-6459-0669>

P. van der Werf  <https://orcid.org/0000-0001-5434-5942>

F. P. Israel  <https://orcid.org/0000-0002-6760-9449>

References

- Aalto, S., Costagliola, F., van der Tak, F., & Meijerink, R. 2011, *A&A*, **527**, A69
- Aalto, S., Martín, S., Costagliola, F., et al. 2015, *A&A*, **584**, A42
- Bergin, E. A., Kaufman, M. J., Melnick, G. J., Snell, R. L., & Howe, J. E. 2003, *ApJ*, **582**, 830
- Bergin, E. A., Melnick, G. J., & Neufeld, D. A. 1998, *ApJ*, **499**, 777
- Bergin, E. A., Melnick, G. J., Stauffer, J. R., et al. 2000, *ApJL*, **539**, L129
- Beswick, R. J., Pedlar, A., Mundell, C. G., & Gallimore, J. F. 2001, *MNRAS*, **325**, 151
- Bialy, S., & Sternberg, A. 2015, *MNRAS*, **450**, 4424
- Bolatto, A. D., Warren, S. R., Leroy, A. K., et al. 2013, *Natur*, **499**, 450
- Carilli, C. L., Wrobel, J. M., & Ulvestad, J. S. 1998, *AJ*, **115**, 928
- Caselli, P., Keto, E., Pagani, L., et al. 2010, *A&A*, **521**, L29
- Castor, J. I. 1970, *MNRAS*, **149**, 111
- Cernicharo, J., Goicoechea, J. R., Pardo, J. R., & Asensio-Ramos, A. 2006a, *ApJ*, **642**, 940
- Cernicharo, J., et al. 2006b, *ApJL*, **649**, L33
- Chou, R. C. Y., et al. 2007, *ApJ*, **670**, 116
- Combes, F., & Wiklind, T. 1997, *ApJL*, **486**, L79
- Combes, F., Rex, M., Rawle, T. D., et al. 2012, *A&A*, **538**, L4
- Daniel, F., Dubernet, M.-L., & Grosjean, A. 2011, *A&A*, **536**, A76
- Downes, D., & Eckart, A. 2007, *A&A*, **468**, L57
- Downes, D., & Solomon, P. M. 1998, *ApJ*, **507**, 615
- Downes, D., Solomon, P. M., & Radford, S. J. E. 1993, *ApJL*, **414**, L13
- Draine, B. T., Dale, D. A., Bendo, G., et al. 2007, *ApJ*, **663**, 866
- Elmegreen, B. G., Morris, M., & Elmegreen, D. M. 1980, *ApJ*, **240**, 455
- Emprechtinger, M., Monje, R. R., van der Tak, F. F. S., et al. 2012, *ApJ*, **756**, 136
- Engel, H., et al. 2010, *A&A*, **524**, A56
- Espada, D. 2013, in ASP Conf Ser. 476, New Trends in Radio Astronomy in the ALMA Era: The 30th Anniversary of Nobeyama Radio Observatory, ed. R. Kawabe, N. Kuno, & S. Yamamoto (San Francisco, CA: ASP), 69
- Espada, D., Matsushita, S., Peck, A., et al. 2009, *ApJ*, **695**, 116
- Feruglio, C., Fiore, F., Piconcelli, E., et al. 2013a, *A&A*, **558**, A87
- Feruglio, C., et al. 2013b, *A&A*, **549**, A51
- Fischer, J., et al. 1999, *Ap&SS*, **266**, 91
- France, K., Herczeg, G. J., McJunkin, M., & Penton, S. V. 2014, *ApJ*, **794**, 160
- Gallagher, S. C., Brandt, W. N., Chartas, G., Garmire, G. P., & Sambruna, R. M. 2002, *ApJ*, **569**, 655
- Gallimore, J. F., Baum, S. A., & O'Dea, C. P. 2004, *ApJ*, **613**, 794
- Gao, Y., Lo, K. Y., Lee, S.-W., & Lee, T.-H. 2001, *ApJ*, **548**, 172
- Gerssen, J., van der Marel, R. P., Axon, D., et al. 2004, *AJ*, **127**, 75
- Goldader, J. D., Joseph, R. D., Doyon, R., & Sanders, D. B. 1995, *ApJ*, **444**, 97
- González-Alfonso, E., Fischer, J., Aalto, S., & Falstad, N. 2014, *A&A*, **567**, A91
- González-Alfonso, E., Smith, H. A., Fischer, J., & Cernicharo, J. 2004, *ApJ*, **613**, 247
- González-Alfonso, E., Fischer, J., Bruderer, S., et al. 2013, *A&A*, **550**, A25
- González-Alfonso, E., Fischer, J., Graciá-Carpio, J., et al. 2012, *A&A*, **541**, A4
- González-Alfonso, E., Fischer, J., Isaak, K., et al. 2010, *A&A*, **518**, L43
- Greve, T. R., Leonidaki, I., Xilouris, E. M., et al. 2014, *ApJ*, **794**, 142
- Guainazzi, M., Matt, G., Brandt, W. N., et al. 2000, *A&A*, **356**, 463
- Helou, G., Soifer, B. T., & Rowan-Robinson, M. 1985, *ApJL*, **298**, L7
- Hollenbach, D., & McKee, C. F. 1979, *ApJS*, **41**, 555
- Iono, D., Wilson, C. D., Takakuwa, S., et al. 2007, *ApJ*, **659**, 283
- Israel, F. P. 1998, *A&ARv*, **8**, 237
- Israel, F. P., Güsten, R., Meijerink, R., et al. 2014, *A&A*, **562**, A96
- Israel, F. P., Raban, D., Booth, R. S., & Rantakyö, F. T. 2008, *A&A*, **483**, 741
- Iwasawa, K., Koyama, K., Awaki, H., et al. 1993, *ApJ*, **409**, 155
- Kamenetzky, J., Glenn, J., Rangwala, N., et al. 2012, *ApJ*, **753**, 70
- König, S., Martín, S., Müller, S., et al. 2017, *A&A*, **602**, 42
- Koribalski, B., Whiteoak, J. B., & Houghton, S. 1995, *PASA*, **12**, 20
- Krips, M., Eckart, A., Neri, R., et al. 2006, *A&A*, **446**, 113
- Krips, M., Martín, S., Eckart, A., et al. 2011, *ApJ*, **736**, 37
- Kruijssen, J. M. D., & Longmore, S. N. 2013, *MNRAS*, **435**, 2598
- Loenen, A. F., van der Werf, P. P., Güsten, R., et al. 2010, *A&A*, **521**, L2
- Marconi, A., Oliva, E., van der Werf, P. P., et al. 2000, *A&A*, **357**, 24
- Markwardt, C. B. 2009, in ASP Conf. Ser. 411, Astronomical Data Analysis Software and Systems XVIII, ed. D. A. Bohlender, D. Durand, & P. Dowler (San Francisco, CA: ASP), 251
- Meijerink, R., Kristensen, L. E., Weiß, A., et al. 2013, *ApJL*, **762**, L16
- Meisenheimer, K., Tristram, K. R. W., Jaffe, W., et al. 2007, *A&A*, **471**, 453
- Melnick, G. J., Stauffer, J. R., Ashby, M. L. N., et al. 2000, *ApJL*, **539**, L77
- Menten, K. M., Lundgren, A., Belloche, A., Thorwirth, S., & Reid, M. J. 2008, *A&A*, **477**, 185
- Mitsuishi, I., Yamasaki, N. Y., & Takei, Y. 2013, *PASJ*, **65**, 44
- Monje, R. R., Lord, S., Falgarone, E., et al. 2014, *ApJ*, **785**, 22
- Moorwood, A. F. M., van der Werf, P. P., Kotilainen, J. K., Marconi, A., & Oliva, E. 1996, *A&A*, **308**, L1
- Müller Sánchez, F., Davies, R. I., Genzel, R., et al. 2009, *ApJ*, **691**, 749
- Müller-Sánchez, F., González-Martín, O., Fernández-Ontiveros, J. A., Acosta-Pulido, J. A., & Prieto, M. A. 2010, *ApJ*, **716**, 1166
- Mumma, M. J., Weaver, H. A., & Larson, H. P. 1987, *A&A*, **187**, 419
- Omont, A., Neri, R., Cox, P., et al. 2011, *A&A*, **530**, L3
- Omont, A., Yang, C., Cox, P., et al. 2013, *A&A*, **551**, A115
- Ott, J., Meier, D. S., McCoy, M., et al. 2013, *ApJL*, **771**, L41
- Panuzzo, P., Rangwala, N., Rykala, A., et al. 2010, *A&A*, **518**, L37
- Papadopoulos, P. P., van der Werf, P. P., Xilouris, E. M., et al. 2012, *MNRAS*, **426**, 2601
- Papadopoulos, P. P., Zhang, Z.-Y., Xilouris, E. M., et al. 2014, *ApJ*, **788**, 153
- Pérez-Beaupuits, J. P., Wada, K., & Spaans, M. 2011, *ApJ*, **730**, 48
- Poelman, D. R., & Spaans, M. 2005, *A&A*, **440**, 559
- Poelman, D. R., & Spaans, M. 2006, *A&A*, **453**, 615
- Poelman, D. R., Spaans, M., & Tielens, A. G. G. M. 2007, *A&A*, **464**, 1023
- Poelman, D. R., & van der Tak, F. F. S. 2007, *A&A*, **475**, 949
- Poncelet, A., Sol, H., & Perrin, G. 2008, *A&A*, **481**, 305
- Priddey, R. S., & McMahon, R. G. 2001, *MNRAS*, **324**, L17
- Rangwala, N., Maloney, P. R., Glenn, J., et al. 2011, *ApJ*, **743**, 94
- Rangwala, N., Maloney, P. R., Wilson, C. D., et al. 2015, *ApJ*, **806**, 17
- Rosenberg, M. J. F., Kazandjian, M. V., van der Werf, P. P., et al. 2014, *A&A*, **564**, A126
- Sakamoto, K., et al. 2009, *ApJL*, **700**, L104
- Salomé, Q., Salomé, P., Combes, F., Hamer, S., & Heywood, I. 2016, *A&A*, **586**, A45
- Sanders, D. B., Mazzarella, J. M., Kim, D.-C., Surace, J. A., & Soifer, B. T. 2003, *AJ*, **126**, 1607
- Schinnerer, E., Eckart, A., Tacconi, L. J., Genzel, R., & Downes, D. 2000, *ApJ*, **533**, 850
- Schirm, M. R. P., Wilson, C. D., Madden, S. C., & Clements, D. L. 2016, *ApJ*, **823**, 87
- Schirm, M. R. P., Wilson, C. D., Parkin, T. J., et al. 2014, *ApJ*, **781**, 101
- Schoeier, F. L., van der Tak, F. F. S., van Dishoeck, E. F., & Black, J. H. 2005, *A&A*, **432**, 369
- Scoville, N., Sheth, K., Walter, F., et al. 2015, *ApJ*, **800**, 70
- Scoville, N. Z., Yun, M. S., & Bryant, P. M. 1997, *ApJ*, **484**, 702
- Soifer, B. T., Neugebauer, G., Matthews, K., et al. 2000, *AJ*, **119**, 509

- Spinoglio, L., Pereira-Santaella, M., Busquet, G., et al. 2012, *ApJ*, **758**, 108
- Spoon, H. W. W., Moorwood, A. F. M., Pontoppidan, K. M., et al. 2003, *A&A*, **402**, 499
- Swinbank, A. M., Papadopoulos, P. P., Cox, P., et al. 2011, *ApJ*, **742**, 11
- Tacconi, L. J., Genzel, R., Blietz, M., et al. 1994, *ApJL*, **426**, 77
- Tacconi, L. J., Genzel, R., Lutz, D., et al. 2002, *ApJ*, **580**, 73
- Tacconi, L. J., & Young, J. S. 1985, *ApJ*, **290**, 602
- Takahashi, T., Silk, J., & Hollenbach, D. J. 1983, *ApJ*, **275**, 145
- Taylor, G. B., Silver, C. S., Ulvestad, J. S., & Carilli, C. L. 1999, *ApJ*, **519**, 185
- Tunnard, R., Greve, T. R., Garcia-Burillo, S., et al. 2015, *ApJ*, **800**, 25
- van der Tak, F., Weiss, A., Liu, L., & Guesten, R. 2016, *A&A*, **593**, 43
- van der Tak, F. F. S., Tuthill, P. G., & Danchi, W. C. 2005, *A&A*, **431**, 993
- van der Werf, P. P., Berciano Alba, A., Spaans, M., et al. 2011, *ApJL*, **741**, L38
- van der Werf, P. P., Isaak, K. G., Meijerink, R., et al. 2010, *A&A*, **518**, L42
- van Zadelhoff, G.-J., Dullemond, C. P., van der Tak, F. F. S., et al. 2002, *A&A*, **395**, 373
- Walter, F., Weiss, A., & Scoville, N. 2002, *ApJL*, **580**, L21
- Wang, J., Fabbiano, G., Karovska, M., Elvis, M., & Risaliti, G. 2012, *ApJ*, **756**, 180
- Wang, J., Zhang, Z.-Y., Qiu, J., et al. 2014, *ApJ*, **796**, 57
- Wang, J., Zhang, Z.-Y., Zhang, J., Shi, Y., & Fang, M. 2016, *MNRAS*, **455**, 3986
- Weiß, A., Downes, D., Neri, R., et al. 2007, *A&A*, **467**, 955
- Weiß, A., Kovács, A., Güsten, R., et al. 2008, *A&A*, **490**, 77
- Weiß, A., Neininger, N., Henkel, C., Stutzki, J., & Klein, U. 2001, *ApJL*, **554**, L143
- Weiß, A., Requena-Torres, M. A., Güsten, R., et al. 2010, *A&A*, **521**, L1
- Yang, C., Gao, Y., Omont, A., et al. 2013, *ApJL*, **771**, L24
- Yang, C., Omont, A., Beelen, A., et al. 2016, *A&A*, **595**, A80